DOE/ER/54294-1

Final Report:
DIII-D Edge Plasma, Disruptions, and Radiative Processes

Principal Investigators: J.A. Boedo, S.C. Luckhardt, and R.A. Moyer

For the period: 11/1/1997–10/31/03

Recipient organization:
The Regents of the University of California, San Diego
Office of Contract and Grant Administration
9500 Gilman Drive
La Jolla, CA 92093-0934

DoE award number:
DE-FG03-95ER54294
Anticipated amount of unexpended funds at end of budget period:
$0
Reason for excess funds and how they will be used in next budget period:
NA

1. Introduction and project structure

The scientific goal of the UCSD DIII-D Collaboration during this period was to understand the coupling of the core plasma to the plasma-facing components through the plasma boundary (edge and scrape-off layer). To achieve this goal, UCSD scientists studied the transport of particles, momentum, energy, and radiation from the plasma core to the plasma-facing components under normal (e.g. L-mode, H-mode, and ELMs), and off-normal (e.g. disruptions) operating conditions. The Principal Investigators of this project were: Drs. Jose Boedo, Stanley Luckhardt and Rick Moyer. The research was managed as three tasks within the DIII-D Experimental Program:

Task	Title	Task PIs	Scientific Staff
1	Disruptions and Radiative Processes	Luckhardt	Luckhardt Whyte Hollmann Gray
2	Boundary Physics and Turbulent Transport	Boedo Moyer	Boedo Moyer Rudakov
3	UCSD/GA/TEXTOR collaboration on radiating boundaries and RI Mode	Boedo	Boedo Gray

Although this award ended on 10/31/04 when the project administration was moved from the DoE Operations Office in Oakland, CA to the Operations Office in Chicago, IL, the UCSD DIII-D Collaboration on "DIII-D Edge Plasma, Disruptions, and Radiative Processes" continues under DoE award number DE-FG02-04ER54758. The Point of Contact for this activity is Rick Moyer [moyer@fusion.gat.com; (858) 455-2275]. Any questions about this Final Report can be directed to Dr. Moyer.

1.1 Highlights of research results for the Period FY98 – FY04

This Section briefly summarizes the principal results from this research. More details on these highlights can be found in the corresponding sections of this Final Report:

DISCLAIMER

Section 2: Final Report: Disruptions and Radiative Processes

Section 3: Final Report: Boundary Physics and Turbulent Transport

Section 4: Publications to which this research has contributed.

The scientific goal of the UCSD DIII-D Collaboration during this period was to understand the coupling of the core plasma to the plasma-facing components through the plasma boundary (edge and scrape-off layer). To achieve this goal, UCSD scientists studied the transport of particles, momentum, energy, and radiation from the plasma core to the plasma-facing components under normal (e.g. L-mode, H-mode, and ELMs), and off-normal (e.g. disruptions) operating conditions. During the six year period covered by this Final Report, FY 1998 through FY 2004, UCSD scientists made a substantial number of significant contributions to the DIII-D, U.S. national, and international fusion research programs. This research contributed to 129 research articles, including 40 first-authored by UCSD scientists. Highlights include:

Disruptions and Radiative Processes:

- design, development, and implementation of the DISRAD II fast radiated power bolometer using next generation AXUV diode technology. The success of this UCSD diagnostic led to it's adoption for refurbishing of the poloidal SXR arrays during the Long Torus Opening Activity (LTOA) in 2005-2006; see Section 2.7, page 2-16.
- Development of "killer pellets" and massive gas jets for mitigation of the deleterious effects of disruptions in tokamaks, including: radiative dissipation of the energy released in the thermal quench, and reduction of halo currents and concomittent mechanical forces on structural components during the current quench; extension of these results to ITER-relevant conditions would significantly impact the viability of ITER and other next-step burning plasma devices; see Section 2.2, page 2-2.
- First characterization of the post-thermal quench plasma characteristics needed for understanding and mitigating disruption current quenches, including the plasma electron temperature T_e and effective ion charge Z_{eff} ; see Section 2.2 and Fig. 2.7, page 2-2.
- Development of the 0-D impurity and plasma radiation model KPRAD for interpreting the results of impurity seeded disrupting discharges using both "killer pellets" and massive gas jets; see Section 2.2, and Figs. 2.9 and 2.12, page 2-2

Boundary Physics and Turbulent Transport:

- First measurement of Mach number ~ 1 parallel plasma flow speeds and parallel heat convection in attached and detached divertor operation; see Section 3.6.1, page 3-15.
- Discovery of high plasma potential at the divertor X-point and strong ExB circulation of particles from the outer to inner divertor legs; see Section 3.6.2 page 3-17.
- Characterization of the non-diffusive nature of scrape-off layer (SOL) transport via "blobs"—filaments that are generated at the separatrix and which convect rapidly across the SOL to the first wall; see Section 3.6.5, page 3-26
- Discovery that ELMs consist of packets of "blobs" convecting through the SOL; see Section 3.6.6, page 3-28.
- Discovery of signatures of radially extended transport events ("avalanches") in the plasma edge, and consistently with Self-organized criticality (SOC); see Section 3.3.1, page 3-3.

- Discovery of signatures of non-linear mode coupling via the electrostatic Reynolds stress across spontaneous L-H transitions; see Sections 3.4.3-4, page 3-12.
- Demonstration that the H-mode pedestal height and width are governed by plasma physics effects in DIII-D/C-Mod dimensionless scaling experiments. Obtained in DIII-D Type I ELM-free H-modes at the dimensionally scaled pedestal parameters and input power, that featured a quasi-coherent (QC) mode that scaled dimensionlessly from C-Mod EDA H-modes; see Section 3.7.1, page 3-29.
- Development in collaboration with T. Evans (GA) of a computational model (TRIP3D) for magnetic field line integration in a realistic poloidal divertor tokamak geometry by modifying the TRIPND field line code to use the EFIT 2-D axisymmetric equilibrium reconstruction; see Sections 3.8.2-4, page 3-38.
- First study in collaboration with T. Evans (GA) of the role of 3-D effects (intrinsic field errors and error fields from various sources) on the magnetic topology of the H-mode pedestal region in a poloidally diverted tokamak; Section 3.8, page 3-35.
- Proposal and successful implementation with T. Evans (GA) of Type I ELM control in high performance H-modes using n=3 edge resonant magnetic perturbations from the I-coils. Extension of these results to ITER-relevant conditions would significantly enhance the viability of ITER and other next-step burning plasma devices; see Sections 3.8.6-7 and Section 3.9, page 3-43.

1.2 K-14 Plasma Science Educational Outreach

The Fusion Group of the Center for Energy Research (CERFE) and its predecessor, the Fusion Energy Research Program (FERP) have maintained an active K-14 plasma science educational outreach program since 1996. The program has been coordinated by Dr. R. Moyer and utilizes the scientific, technical, and administrative staff as volunteers in the various activities. The Fusion Educational Outreach Program offers a variety of opportunities for middle school and high school students and their teachers to experience hands-on activities and demonstrations relating to plasma science (the science of hot, ionized gases) and fusion energy. These activities include (see Table 1-1):

- A 3-week summer course for high school students as part of the Academic Connections program "From Neon Lights to Nuclear Fusion".
- Tours of PISCES and other fusion research facilities on the UCSD campus
- Tours of the DIII-D National Fusion Facility, located at General Atomics.
- Hands-on science experiences for middle and high school students in conjunction with other outreach activities at UCSD:
  - TRIO Upward Bound program for traditionally under-represented students in math, science and engineering
  - Expanding Your Horizons workshops for middle and high school girls
- Hands-on science experiences for middle and high school students in conjunction with:
  - San Diego Educational Technology Fairs run by the San Diego Science Alliance;
  - Plasma Expos of the Division of Plasma Physics of the American Physical Society, held during the Annual Meeting of the Division of Plasma Physics.
- Visits to area schools ("scientist in the classroom" and career day).

TABLE 1-1: UCSD CERFE Plasma Science Educational Outreach, 1998–2004

Date	Event	Sponsor	Location
11/1998	Plasma Expo	APS Div. of Plasma Physics	New Orleans, LA
11/1999	Plasma Expo	APS Div. of Plasma Physics	Seattle, WA
1/2000	Lead Scientist/Teacher Alliance	American Physical Society	Washington, D.C.
3/2000	Newsletter article on Lead Scientist/Teacher Alliance Workshop	San Diego Science Alliance	San Diego, CA
2/23/2000	4th Annual Educational Technology Fair	San Diego Science Alliance	Del Mar, CA
2/26/2000	National Engineers Week celebration	Reuben H. Fleet Science Center	San Diego, CA
3/2000	San Diego Leadership Institute (SanDeLI-2)	San Diego Science Alliance	San Diego, CA
7/2000	Instructor, Plasma Institute for teachers	General Atomics Fusion Education Group	San Diego, CA
2/21/2001	5th Annual Educational Technology Fair	San Diego Science Alliance	Del Mar, CA
7/2001	Instructor, Plasma Institute for teachers	General Atomics Fusion Education Group	San Diego, CA
10/19/2001	Educational Technology Fair	San Diego Science Alliance	Del Mar, CA
11/2001	Plasma Expo	APS Div. of Plasma Physics	Long Beach, CA
7/2002	Radient Plasmas: from Neon Lights to Nuclear Fusion in-residence summer course for high school students	Academic Connections, UCSD Extension	San Diego, CA
10/11/2002	6th Annual Educational Technology Fair	San Diego Science Alliance	Del Mar, CA
11/2002	Plasma Expo	APS Div. of Plasma Physics	Orlando, FL
2/19/2003	7th Annual Educational Technology Fair	San Diego Science Alliance	Del Mar, CA
2/2003	Judge, Southern California Junior Science & Humanities Symposium		So. CA
4/2003	Guest Instructor, "Plasma Science and Fusion Energy"	TRIO/Upward Bound Program, UCSD	San Diego, CA
11/2003	Plasma Expo	APS Div. of Plasma Physics	Albuquerque, NM
5/28/2003	"Plasma Science and Fusion Energy" Career Day presentation	Jefferson Middle School	Oceanside, CA
3/13/2004	Guest Instructor, "Plasma Science and Fusion Energy"	TRIO/Upward Bound Program, UCSD	San Diego, CA
2/23/2005	8th Annual Educational Technology Fair	San Diego Science Alliance	Del Mar, CA
4/2/2005	Instructor, "Plasma Science in Your Future"	2005 Expanding Your Horizons Conference, UCSD	San Diego, CA
5/12/2005	Instructor and DIII-D Tour Guide	University of San Diego undergraduate physics class	San Diego, CA

2. Disruptions and Radiative Processes

2.1 Introduction

The mitigation of tokamak disruptions continues to be a critical part of research into making the tokamak a viable design concept for a power-producing magnetic confinement reactor. Uncontrolled and frequent disruptions in a reactor-class tokamak will cause severe damage to its internal components and cause unacceptable delays and costs in their repair [1]. This damage includes ablation or melting of plasma-facing components and structural damage caused by the extremely large electromagnetic forces produced during the disruption. The goal of disruption mitigation research is to devise credible experimental mitigation scenarios on present devices (that are usually not severely affected by disruptions) that will work on the next generation of large-scale tokamaks or other similar magnetic confinement devices (e.g., spherical tokamak). This effort is necessary, since disruption avoidance can never be fully relied on to control disruptions (e.g., disruptions caused by equipment failure rather than stability limitations). Advanced Tokamak (AT) scenarios will be the focus of DIII-D research in the next years. The higher power densities associated with these designs imply a greater risk of damage due to disruptive events. This makes disruption avoidance and mitigation of extreme importance for the Advanced Tokamak to be a viable reactor design concept.

Encouraging results have been obtained on DIII-D and other tokamaks with the use of radiative disruption mitigation techniques. These scenarios introduce large quantities of an impurity into the hot, disrupting plasma in order to remove rapidly the plasma's kinetic and magnetic energy in the form of soft X-ray and UV radiation before the plasma can damage internal components.

Two critical limitations exist for the study of disruption mitigation on current devices. First is a lack of adequate diagnosis during the perturbative disruption event, when standard tokamak plasma diagnostics often fail. The second limitation is the order of magnitude differences between current and next-step devices in plasma stored kinetic and magnetic energy. This disallows simple extrapolation of mitigation results on current tokamaks to the reactor-class tokamaks that critically need the mitigation. The solution to these limitations is to provide validated physical models for the mitigation experiments carried out on current devices and to compare these models as much as possible to existing or newly developed disruption diagnostics.

DIII-D has an extensive set of existing hardware and diagnostics for disruption studies (Fig. 2.1). A key aspect to recent advances in disruption diagnosis has been the careful use of multiple diagnostics to illuminate interesting physics issues. An example of this is the development of a UV spectroscopy technique to measure T_e and Z_{eff}, which would not be possible without several supporting diagnostics (e.g., fast interferometry) to verify the diagnostic technique [2]. This research tests the unique DIII-D disruption diagnostic set with a wider range of disruption types (e.g., AT disruptions) and integrates several new diagnostic measurements.

The improving diagnostic capabilities for disruptions have also increased the need for clear physical models that describe the disruption and mitigation scenarios. The observed trend for current quench times is the opposite of that expected from the parameters of the target plasma. Most current simulations rely therefore on ad hoc imposed current quench times or resistivities without any knowledge of how the plasma achieves such short quench tines with high beta plasmas. This gap in physical knowledge is unacceptable if one desires true predictive capability of disruption behavior in an AT fusion device. In order to alleviate this situation, a combination of better diagnosis and thorough testing of numerical models must be carried out on existing

devices. The numerical codes should simulate the important disruption parameters (energy balance, radiation, halo currents, runaway electrons) in a self-consistent manner that matches the experimental data. Due to its comprehensive diagnostic capabilities and proven set of modeling tools, DIII-D is well poised to provide much of these insights.

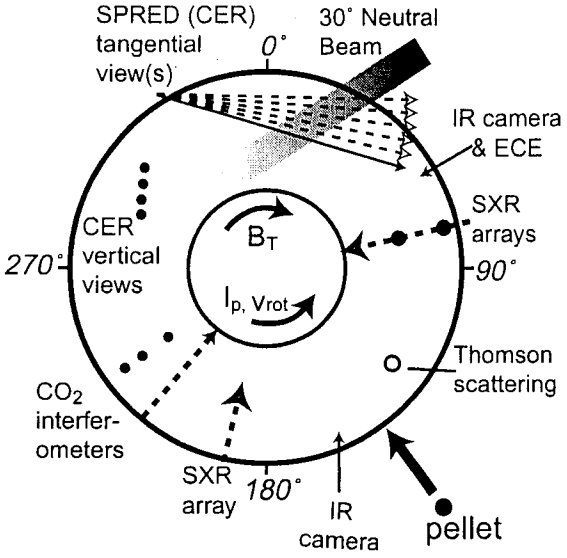

Fig. 2.1: Toroidal plane view of DIII-D tokamak and sample diagnostics for studying radiative disruption mitigation

2.2 Disruption Mitigation

The single most important result obtained by the DIII-D Disruption Mitigation Group during the past six years was the development of the high pressure noble gas jet (HPJ) as a disruption mitigation tool. The UCSD group played an important role in these experiments and their analysis. Briefly the results of these experiments are summarized as:

- Demonstrated high-pressure noble gas jet injection (HPJ) as an effective method to mitigate the effects of disruptions in tokamaks.
  - Divertor thermal loading was decreased up to a factor of 10 by dissipating the plasma energy by radiation of gas jet species (neon or argon).
  - Reduced mechanical stresses on the vessel from poloidal halo currents (JxB forces) by initiating a rapid plasma termination with a plasma that remained well-centered in the vessel away from the walls.
  - Suppressed runaway electron generation in the current quench by the high neutral gas density.
- Demonstrated the ability to detect in real-time the onset of two types of disruptions: vertical displacement events (VDE) and radiative/density limit. The control system triggered the gas-jet injection within a few milliseconds and successfully mitigated the disruption heat loads and vessel stresses in DIII-D without causing runaway electrons.
- Initiated studies on the extrapolation of the gas-jet mitigation technique to burning plasma experiments.

Here we briefly summarize the highlights of these HPJ mitigation experiments. During the past six years, our experiments at DIII-D tokamak have measured and verified the effectiveness of this high pressure gas jet (HPJ) technique. The UCSD DISRAD-II radiometer provided critical

information on the total radiated power and its spatial and temporal evolution. Fig. 2.2 shows an example of this important result.

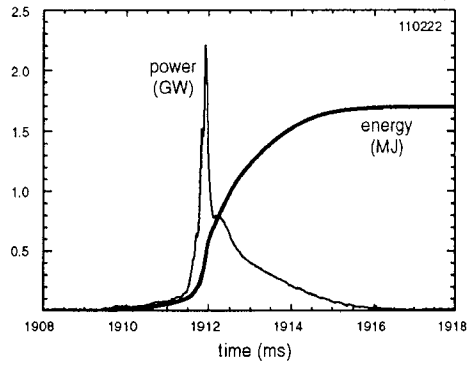

Fig. 2.2: Analysis of the 30 chord fast radiometer DISRAD-II showed that the time evolution of the radiated power during an Argon HPJ disruption reaches the 2GW level and rapidly removes the plasma stored energy over a 2-3 ms timescale.

Disruption mitigation research has been very successful over the last six years at DIII-D [3]. The program has demonstrated considerable experimental advances in controlling the deleterious effects of disruptions. This has been matched by improved diagnostic and modeling capability for understanding the disruption mitigation. An example of improved diagnosis and modeling is the observation of anomalous rapid inward transport of impurities injected for radiative disruption mitigation. This was first seen with "killer" pellets (Fig. 2.3) and also with massive helium gas injection (Fig. 2.4). It is now understood that this phenomenon is largely responsible for the effectiveness of the mitigation scenarios. The rapid transport places the impurity in the hottest part of the core plasma, which leads to high fractions of the total stored energy being radiated. This could be very beneficial for the large plasmas expected in next-step tokamak devices, where pellet or gas penetration will be limited to only the edge of the plasma. However, the underlying mechanism for this effect is not yet known. Obviously, the extrapolation of these mitigation scenarios to large-scale devices requires this explanation.

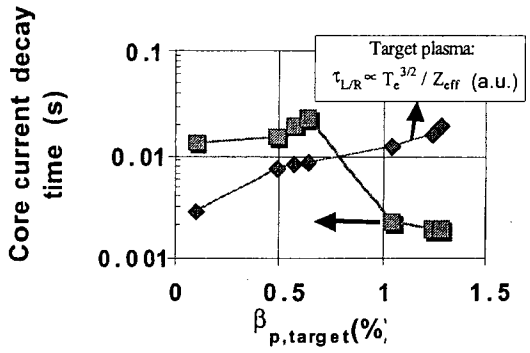

Fig. 2.3: Experimentally measured core current decay time (squares) versus poloidal beta (βp) of the target plasma. The observed trend of decreasing decay time with increasing beta is the opposite of expected L/R time based on target plasma resistivity (diamonds). Two possible reasons for this discrepancy: the presence of MHD-caused anomalous resistivity in high β disruptions or unknown details about the plasma cooling mechanism (e.g., effect of impurities removed from wall).

The use of massive helium gas injection has shown itself to be particularly promising as a mitigation technique. As seen in Table 2.1, divertor heat loading and halo currents were greatly reduced by the helium injection, and unlike killer pellets of neon and argon [5], no runaway electrons were generated during the current quench. An important diagnostic development was

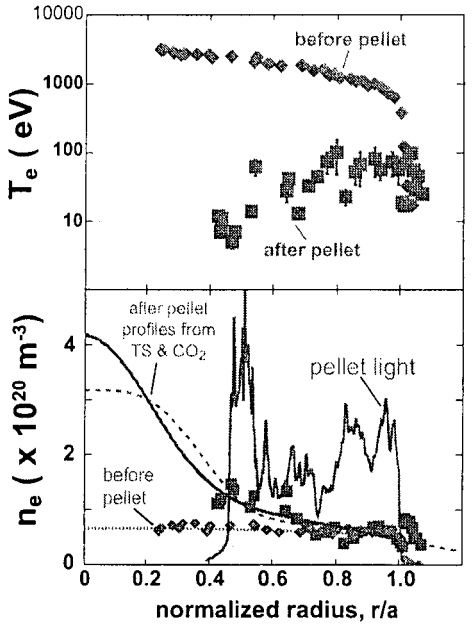

Fig. 2.4: DIII-D core plasma Thomson scattering (TS) profiles before and after injection of neon impurity pellet on discharge #88806 [4]. A combination of interferometry and TS (bottom) clearly show rapid inward transport of the pellet material beyond the ablation penetration depth of the pellet into the center of the plasma in < 1 ms. This transport leads to very efficient cooling of central plasma to T_e < 10 eV (top).

TABLE 2.1
Summary of Results for Massive Helium Gas Injection Mitigation on a VDE (Vertical Displacement Event) Disruption on DIII-D

Disruption Type	VDE with No Mitigation	VDE with Massive He Injection
Gas injection rate		10^{23} atoms in ~7 ms
Peak I_{halo} (MA)	0.30	0.13
Toroidal Peaking Factor	~2	1.2
Vessel movement (mm)	1.5 mm	< 0.9 mm
Energy to divertor plate (MJ)	0.73	< 0.05
Energy radiated (MJ)	1.38	1.95

also made possible by the helium gas injection. Namely, a VUV spectroscopy diagnostic technique was used to simultaneously measure, for the first time, plasma electron temperature (T_e) and effective charge-state (Z_{eff}) during disruptions [2]. Free-bound continuum helium radiation from the cold and dense disrupting plasma was easily measured by the DIII-D survey VUV spectrometer (Fig. 2.5). This resulted in precise measurement of T_e and Z_{eff} in both the core and halo plasmas (Fig. 2.6). These plasma parameters are critical in understanding the physics of disruptions and their mitigation. T_e and Z_{eff} together describe the thermal, ionization and energy balance of the impurities in the plasma, as well as the classical plasma resistivity. Using this new diagnostic technique in combination with the halo current model developed by General Atomics

[6], it was shown for the first time that the disrupting plasma may exhibit classical resistivity (fig. 2.7) [7]. This is demonstrated by the excellent agreement between the halo current model and experiment (Fig. 2.8).

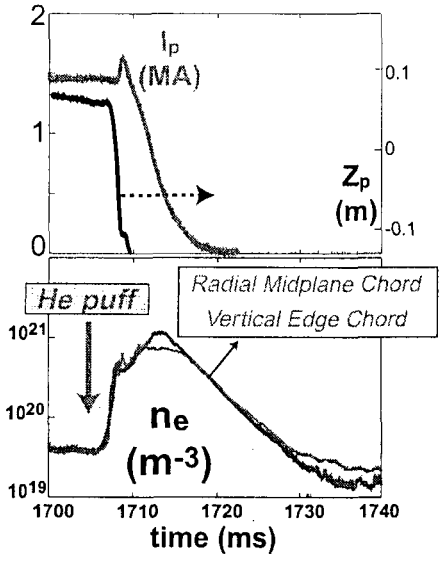

Fig. 2.5: Massive helium gas injection disruption mitigation on DIII-D discharge #96762. The simultaneous rise of an edge and centrally viewing interferometer chord indicate that the helium quickly penetrates to the center of the discharge (bottom).

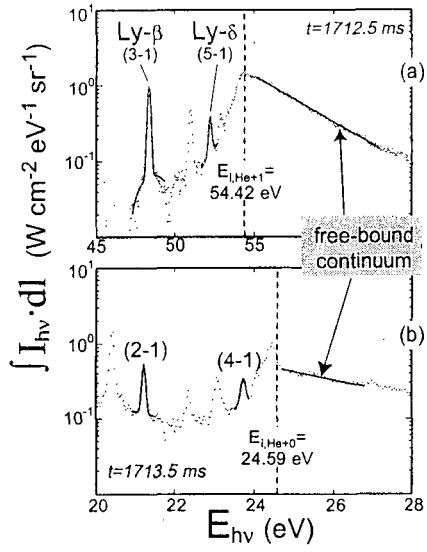

Fig. 2.6: Sample spectra for (a) He II and (b) He I series limit spectra obtained with DIII-D XUV survey spectrometer during massive helium gas injection discharge #96762 [2]. Slope of free-bound continuum determines T_e and relative intensity of He I and He II radiation determines Zeff. Shown are measured data (points) and fits (solid lines) to recombination continua that give T_e=3.59 +/- 0.03 eV and 3.89 +/-0.36 eV for He II and He I, respectively.

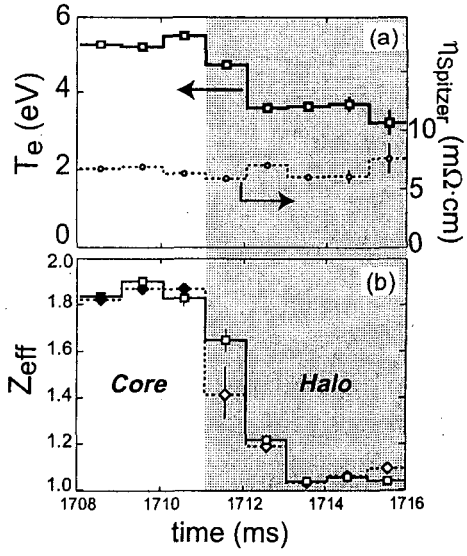

Fig. 2.7: (a) Measured electron temperature (T_e) and calculated Spitzer resistivity ($\eta_{Spitzer}$) for the helium mitigated DIII-D discharge #96762 [2]. Shaded region indicates when emission weighted location of measurement from single line-of-sight UV spectrometer is outside of the last-closed flux surface. This change is due to the vertical movement of the plasma during the disruption; (b) Measured Z_{eff} from two independent methods: line ratios method (solid line with squares), and continuum ratios method (dashed line with diamonds). Solid points indicate lower limit of Z_{eff} based on limit of detection in He I spectra.

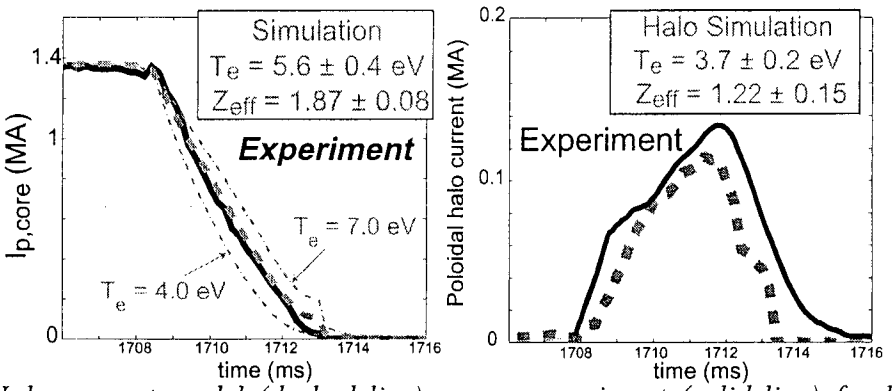

Fig. 2.8: Halo current model (dashed line) versus experiment (solid line) for helium gas mitigation discharge #96762 for core current decay (top) and poloidal halo current evolution (bottom) [7]. Model uses UV spectroscopy time-averaged T_e and Z_{eff} measurements (Fig. 2.7) noted and assumption of classical Spitzer resistivity for plasma. Light dash-dot line in left figure shows sensitivity of prediction to T_e used in model.

The KPRAD (Killer Pellet + RADiation) numerical code was previously shown to be successful in simulating the mitigation physics associated with neon, argon and methane killer pellets [8]. The model self-consistently calculates the ionization and energy balance of the plasma based on the deposited impurity density and the target plasma parameters. This modeling effort has been extended to the massive He gas injection with great success (Fig. 2.9). The model reproduces all of the important aspects of the mitigation scenario, including the time histories of the electron density and temperature, radiated power and effective plasma charge state. The predictive ability of the code is presently constrained by two factors. First, following the experimental evidence, the impurity is uniformly distributed across the target plasma radius. As previously mentioned, the cause for this phenomenon is unknown. Secondly, the experimental current decay is imposed on the simulation. The cause of the rapid transport will be illuminated by planned experiments on DIII-D aimed at carefully studying this effect. Also, a predictive ability for the current decay can be obtained by coupling the KPRAD code to the GA halo current model. These advances will be encouraging for the use of KPRAD as a predictive tool in disruption mitigation studies.

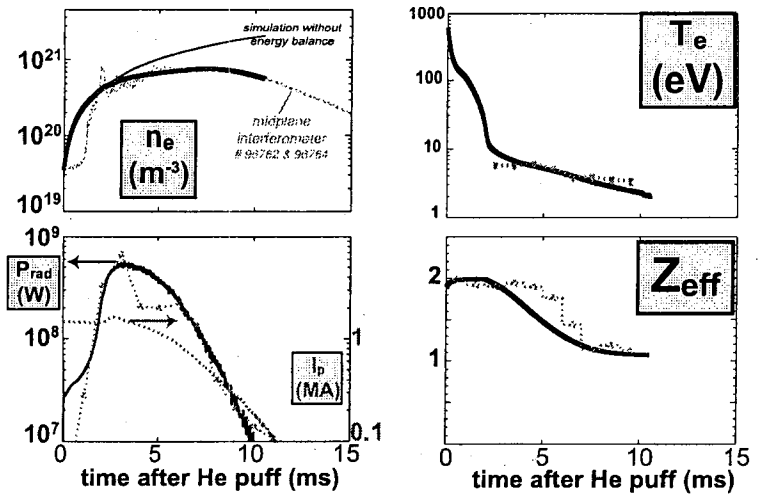

Fig. 2.9: Comparison of KPRAD simulation (solid lines) and experiment (dashed lines) for massive helium gas injection. Instantaneous radial deposition is imposed for the simulation to agree with rapid radial transport in the experiment. All other parameters are fixed by experimental conditions. The model correctly predicts the thermal energy, radiation and ionization balance of the plasma, as well as the density saturation caused by the thermal collapse.

An interesting practical implication for DIII-D was the observation that the initial phase of subsequent plasma discharges was much cleaner after a mitigated disruption than after a non-mitigated disruption. This is presumably a result of the reduced ablation damage of the carbon walls. As a result the initial evolution of the current profile was controlled, allowing one to obtain high-performance discharges immediately after a disruptive discharge. Theoretical extrapolation indicates that high-pressure noble gas injection technique will be equally effective in the burning plasma regime, thereby greatly improving the chance of operational success in future devices.

One of the most interesting mitigation effects of the HPJ was the suppression of runaway beam generation. This is shown in Fig. 2.10, where the plasma current decay waveforms are compared for a case where the disruption is generated by an argon cryo-killer pellet and an relatively large runaway population is generation, and the case of Argon high pressure jet injection where the runaway beam is suppressed. This effect is understood to result from scattering from bound electrons in weakly ionized argon in the HPJ case.

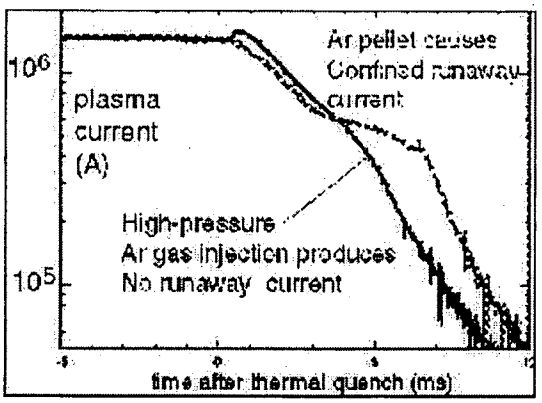

Fig. 2.10: The kink in the plasma current decay in DIII-D disruption experiment, during the disruption current quench is an indicator of runaway electron current production. Copious bursts of hard x-rays are also evident. In the case where we injected a high-pressure argon gas jet, it is evident that there is no kink in the current decay. Very little hard x-ray emission is present in these cases

The bulk of the plasma energy is converted into atomic line radiation in HPJ mitigation. During the CY2001 run period on DIII-D we used DISRAD-I to measure the radiative power evolution during the high-pressure gas jet disruption mitigation experiments. Shown below in Fig. 2.11 are time integrals of radiated power during three shots, terminated by puffs of deuterium, helium, and neon, respectively. Neon was observed to radiate the plasma stored energy more effectively than the other two gases.

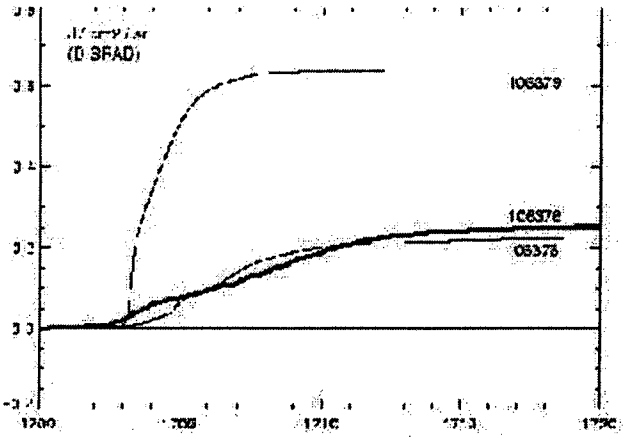

Fig. 2.11 Time integrals of radiated power during three shots, terminated by puffs of deuterium, helium, and neon, respectively. Neon (top curve) was observed to radiate the plasma stored energy more effectively than the other two gases(bottom two curves).

Fig. 2.12 shows the time history of the radiated power density from the single chord DISRAD-I AXUV system during a HPJ mitigated disruption. Prad is found to exceed 1MW/m^2 level, and

rises on a 100 microsecond timescale. We compare this data with the radiated power density predicted by the ionization/energy balance model KPRAD. This measurement appears to confirm the predicted very rapid rise time for radiative power loss, a semi-quantitative confirmation of the absolute magnitude of the power, but a slower decay rate for the radiated power than expected from KPRAD. Analysis of this slow decay effect is continuing.

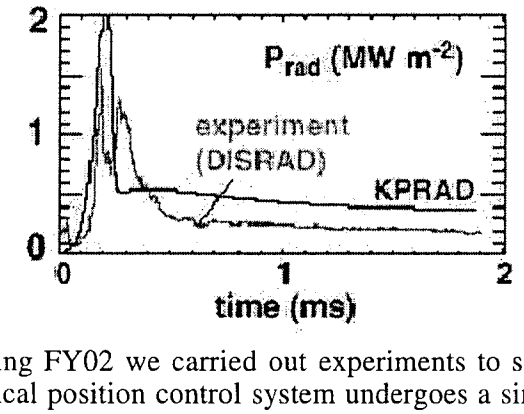

Fig. 2.12: Time history of the radiated power density from the single chord DISRAD-I AXUV system during a HPJ mitigated disruption. Prad is found to exceed 1MW/m^2 level, and rises on a 100 microsecond timescale. We compare this data with the radiated power density predicted by the ionization/energy balance model KPRAD.

During FY02 we carried out experiments to simulate disruption mitigation when the plasma vertical position control system undergoes a simulated failure. In Fig. 2.13 the results of three experiments are shown. The first, in which the vertical position control system is turned off, results in a slow downward drift of the plasma eventually terminating in a disruption. The other two cases, an HPJ was fired when the plasma center line drifted below a predetermined set point, in one case ΔZ = -10cm, and the other with ΔZ = -2cm. It can be seen that the HPJ mitigates the deleterious effects of the disruption in both cases.

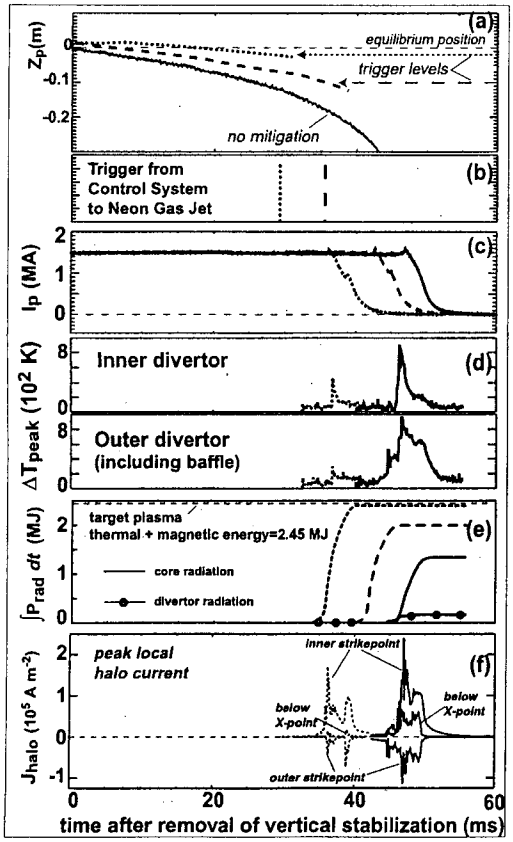

Fig. 2.13: Real-time detection and mitigation of vertical displacement event (VDE) disruptions for three shots: (a) Plasma center vertical position (Z_p) and ΔZ_p trigger levels set in plasma control system. Solid line: no mitigation, dotted line: ΔZ_p = -2 cm, dashed line: ΔZ_p = -10 cm. (b) Triggers to gas jet. (c) Plasma current decays with no runaway electron tail (d) Reduction of maximum divertor tile temperature rise (ΔT_{peak}) at inner and outer divertor. (e) Integrated radiated energy from core and divertor plasma. (f) Reduction of maximum divertor halo currents at inner and outer strikepoint positions and directly below the initial X-point position.

2.3 Disruption Radiated Power Studies

Underpinning the successful disruption mitigation experiments was substantial progress in our understanding of radiative processes in disruptions and in diagnostics for disruptions. Disruptions are considered to be a significant hurdle for reliable reactor-scale tokamak operation, because the resulting heat fluxes are expected to be large enough to damage plasma-facing components [9]. Understanding the time scale and spatial structure of disruptions, as well as achieving early detection and mitigation are therefore important areas of fusion research. The multi-chord fast radiometer DISRAD-II developed and constructed at UCSD [10] has contributed to these goals by enabling spatially-resolved measurement of the radiated power during disruptions on fast time scales (up to 1 MHz). Plots of the radiated power measured during different types of disruptions are shown in Fig. 2.14. The thick curve shows main chamber radiated power, while the thin curve shows divertor radiated power (data was taken in lower-single-null diverted discharges). Also, thermography data of the lower divertor is shown, demonstrating that the divertor heat load corresponds fairly well with the divertor radiated power. The separation between main chamber and divertor radiated power is obtained from the line-integrated radiometer data using a zonal analysis based on EFIT contours; this technique is described in Ref. [11].

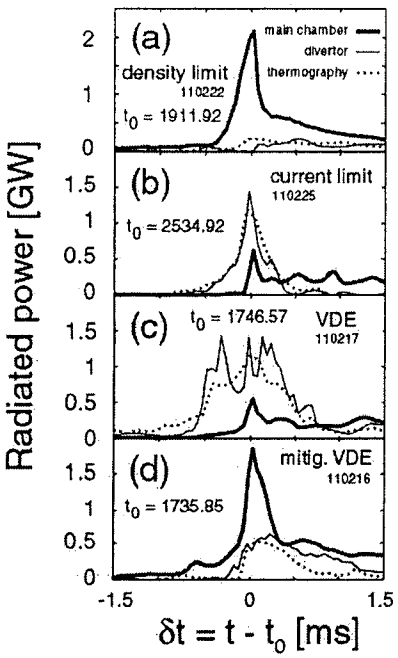

Fig. 2.14: Total radiated power from the main chamber and (lower) divertor region as a function of time for (a) a density limit disruption, (b) a current limit disruption, (c) a vertical displacement event (VDE) disruption, and (c) a neon gas puff-mitigated VDE. The time δt is defined relative to the peak in total radiated power.

Figure 2.14(a) shows a density limit disruption, Fig. 2.14(b) a current limit disruption, Fig. 2.14(c) a downward-moving vertical displacement event (VDE) disruption, and Fig. 2.14(d) shows a similar discharge to Fig. 2.14(c) but preemptively mitigated by a massive puff of neon gas. It can be clearly seen that the large divertor heat loads experienced in the downward-going VDE of Fig. 2.14(c) are reduced by more than a factor of two by the neon gas puff, demonstrating that noble gas puffing can be effective in reducing divertor heat loads during disruptions. Other measurements have shown that this disruption mitigation technique is also effective in suppressing halo currents normally experienced during VDE disruptions [12] and runaway electrons generated during disruption mitigation experiments using cryogenic pellet injection [13].

Interestingly, the main chamber radiated power for the density limit disruption seen in Fig. 2.14(a) is about ten times larger than the divertor radiated power, suggesting that the plasma is somehow "self-mitigating" in this discharge. The available experimental data on this discharge suggests that this self-mitigation is the result of a massive release of deuterium and carbon from the vessel walls. The cause of this neutral release is not well-understood at present, but it is possible that a materials physics effect, such as a sudden transient release of stored hydrocarbons from the super-saturated uppermost mono-layers of the graphite tiles, is responsible.

In Fig. 2.15(a), the midplane D_β brightness, associated with deuterium ionization is plotted as a function of time; while Fig. 2.15(b) shows the magnitude of magnetic fluctuations, associated with MHD activity and large-scale plasma motion; and Fig. 2.15(c) shows the midplane UV brightness, associated dominantly with carbon impurities entering the core plasma, all for the density limit disruption discussed above. It can be seen that the rise in deuterium ionizations begins in advance of any large-scale particle transport to the wall due to MHD and before the main thermal quench radiation spike. These time traces therefore suggest that the observed neutral release is not caused by the standard mechanisms of thermal desorption and sublimation due to wall heating from either plasma flux or radiation heating. Also, estimates based on energy conservation indicate that not enough thermal energy is available to the plasma initially to cause the required amount of local wall heating to thermally sublimate the required amount of carbon [11].

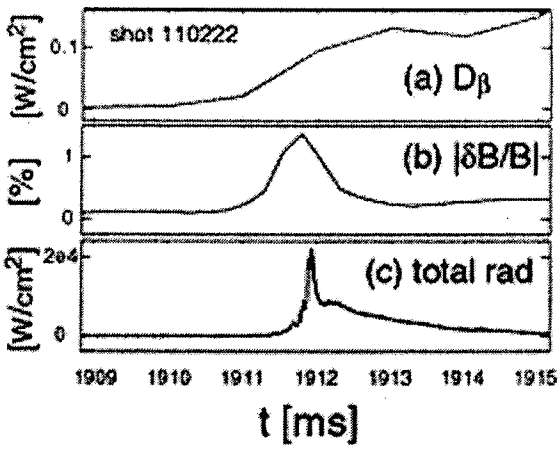

Fig. 2.15. Time traces of (a) midplane D_β brightness, (b) amplitude of magnetic fluctuations, and (c) midplane total radiant brightness for the density limit disruption

The radiated power shown in Fig. 2.15(a) and Fig. 2.15(c) is associated dominantly with carbon impurities released from the wall and into the core plasma. The inward transport of carbon impurities and the associated cold front can be seen in Fig. 2.16. Here, the evolution of the midplane ($z = 0$) radiant emissivity profile is plotted as a function of time. It can be seen that the radiation front travels from the edge of the plasma (at $\delta t = -0.4$ ms) into the center of the plasma (at $\delta t = 0.1$ ms) in a half a millisecond. From this data, an effective impurity diffusion coefficient of order $D_\perp \approx 100$ m^2/s can be estimated; this is roughly 100 times larger than the impurity transport rate measured during normal H-mode operation [14], but is roughly the same size as impurity transport observed during disruptions triggered by pellet injection [15]. Currently, this extremely rapid inward ion transport is not well-understood, although large-scale MHD mixing is probably responsible in some form.

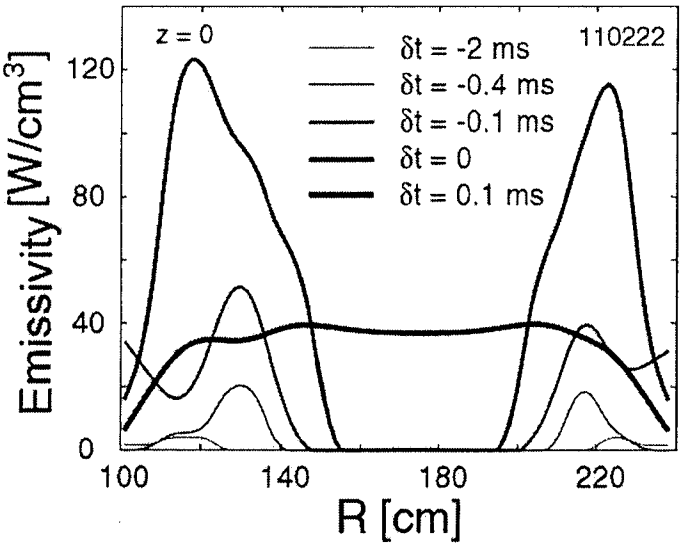

Fig. 2.16. Evolution of radial profile of plasma total emissivity during the onset of the density limit disruption. $\delta t = 0$ is the peak in radiated power

2.4 Study of MHD mode structure in DIII-D using x-ray and UV tomography

As part of the UCSD/DIII-D collaboration in 2001-2003, we analyzed the structure of MHD modes in the DIII-D tokamak using x-ray emission tomography (XET). Measurements of the structure of MHD modes as a function of the plasma profile are important for developing our understanding of MHD behavior of advanced tokamaks and for optimization of tokamak performance. We have found in preliminary studies that modern inversion methods can be used with the existing soft x-ray diode arrays and UV diode arrays to enable a study of MHD mode structure in DIII-D.

2.4.1 Background

The principal goal of the Advanced Tokamak program at DIII-D is the optimization of tokamak performance as a function of the plasma profile. Currently, the most promising advanced tokamak scenarios are "negative central shear," where the current profile is hollow, and "high-l_i", where the current profile is highly peaked on center [16]. Apart from edge instabilities, i.e., ELMs, the largest source of performance limitation in these plasmas is the onset of non-ideal MHD modes, such as neoclassical tearing modes or resistive wall modes [17]. Proposed methods for limiting the onset of these modes include: shearing apart the mode structures with counter-current neutral beam injection, improved magnetic feedback systems, and improved plasma profile tailoring [16]. An understanding of the structure and evolution of MHD modes in relation to the plasma current, rotation, and pressure profiles is an essential part of the plasma profile tailoring effort.

2.4.2 Evaluation of X-ray tomography techniques

The DIII-D fast soft x-ray (SXR) diagnostic arrays have been used extensively in DIII-D disruption experiments [18]. We have investigated how modern inversion methods can be applied to the SXR array data. Mode shapes with poloidal mode number up to m = 4 could be well reconstructed using simulated data. Further refinements using multiple diagnostics may allow reconstruction of higher poloidal mode numbers.

Because of its good spatial (≈5 cm ≈ a/10) and temporal (≈ 5 μs) resolution through the entire plasma, x-ray tomography is currently one of the best methods available for the reconstruction of MHD mode shapes [19]. Electron cyclotron emission (ECE) is a powerful diagnostic for studying local density and temperature fluctuations, however, because of harmonic overlap at low aspect ratios, this method is not always well-suited for MHD mode shape reconstruction. Magnetic probes are useful for measuring MHD mode numbers and frequencies, but are primarily sensitive to the plasma edge and are therefore not ideal for reconstructing the entire radial mode structure. Our approach in reconstructing MHD mode shapes makes use of the existing DIII-D poloidal SXR array. This array consists of two arrays of 32 detectors and was substantially upgraded in FY99. The fast digitizer for this diagnostic runs at 100-250 kHz, which is sufficiently fast to resolve the rotation frequency of typical MHD mode structures (~10 kHz). Additionally, information would be used from existing magnetic and ECE diagnostics, as well as from the DISRAD AXUV diode array.

X-ray tomography was developed for medical use and has been developed extensively for use in that field [20]. This technique has also been used in fusion research devices, such as JET [21], TFTR [19], Alcator C [22], and Wendelstein 7-AS [23], but has not been pursued actively on DIII-D. In a fusion device, the problem to be solved is determining the local plasma emissivity across a poloidal section of the plasma, $\varepsilon(r,z)$, given the line-integrated signal received on each soft x-ray diode, $I = \int \varepsilon(r,z)\, dS$. We have performed inversions of simulated DIII-D SXR data using several techniques. We found the technique of eigenfunction expansion to be the fastest and most robust inversion method; however, the shape of the reconstructed data, while very smooth, was often significantly different from the original simulated data. In particular, the reconstructed mode shape varies significantly depending on what values are chosen for L, the maximum radial mode number, and M, the maximum azimuthal mode number.

The technique of zero-order regularization was found to be robust and easy to implement, however, the quality of the inversions was poor and tended not to be as smooth as the simulated data. A special case of zero-order regularization which deserves mention is the limit $\alpha \rightarrow 0$; this is equivalent to direct inversion using singular-value decomposition (SVD), which was found to be a fast and very easy-to-implement inversion technique, although the resulting inversions tended to be somewhat less smooth than the original data. The smoothness of SVD inversions can be improved by discarding singular values, however, the resulting inversions were found to poorly-reproduce the original data and the number of singular values to be discarded is somewhat arbitrary.

The best-quality inversions were obtained using second-order regularization and maximum entropy methods. Maximum entropy methods have the advantage of built-in enforced positivity; in general, this was found to significantly enhance the quality of the reconstructed plasma emissivity. However, an iterative positivity constraint can also be added to the second-order regularization method, and enforced positivity can undesirable in some applications, such as when solving for a perturbed emissivity. Of these two methods, we prefer second-order regularization, as it is faster and easier to implement.

It is important to mention that great care must be taken in reconstructing azimuthal mode numbers $m > 2$ in DIII-D, because of the well-known Nyquist criterion [21], i.e., detectors looking at the plasma from two poloidal locations can normally only accurately resolve poloidal mode numbers up to $m \approx 2$. Because there is an array of 32 diodes at each of the two poloidal locations, however, this is not a strictly valid requirement, so higher mode numbers can be resolved, depending on the plasma rotation phase and angular resolution of the array viewing

chords. We have performed inversions of simulated data which clearly resolve poloidal mode numbers up to m = 4 using the existing DIII-D poloidal array geometry. In practice, the lowest poloidal mode numbers (m=1, 2, and 3) are found to be important for MHD stability, so we expect to be able to resolve the most important MHD modes using this method. In addition, since the MHD mode structure generally rotates coherently, higher m-resolution can be obtained, if necessary, by analysis of the amplitudes and phases of the mode-induced SXR modulation.

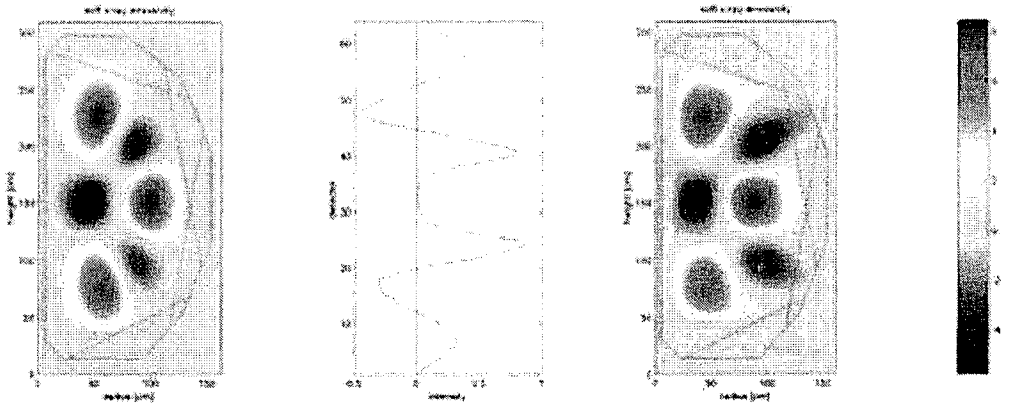

Fig. 2.17: Tomographic inversion of simulated m=3 MHD mode showing perturbed emissivity contours (a), received signal (b), and reconstructed emissivity perturbation contours (c).

A simulated tomographic inversion of x-ray data is shown in Figure 2.17. Here, Figure 2.17(a) shows a poloidal cross-section of DIII-D with simulated perturbed x-ray emissivity contours (arbitrary scale) for a large m=3 MHD mode. The dashed black lines show the field of view of each of the two poloidal arrays, while the solid black lines show the outline of the vacuum vessel. Figure 2.17(b) shows the resulting chord-integrated x-ray intensity measured on the detector array as a function of position, with 5% Gaussian noise added on each detector, and Figure 2.17(c) shows the emissivity reconstructed using only the "measured data" of Figure 2.17(b) and the known detector geometry. It is apparent that the simulated mode structure is fairly well-reconstructed. We have used the method of second-order regularization in inverting the data of Figure 2.17(b).

We have carried out preliminary tomographic inversions of actual DIII-D SXR data. These results indicated the need for improved calibration of the SXR diodes and a need for better data, that is, more data where the fast digitizer is turned on during the peak of the MHD activity and where all the diodes are working with correct gain settings. During the recent DIII-D down-time, the SXR diodes and electronics were upgraded, which should resolve these problems. One method for improved diode calibration which we intend to implement is through analysis of SXR data from smooth, well-characterized plasma profiles, such as from typical Ohmic discharges, for example.

Additionally, we plan to augment the reconstruction of the MHD mode shapes by adding information from other diagnostics to the x-ray tomographic inversions. The planned AXUV photodiode array, for example, is sensitive down to photon energies of about 2 eV and is therefore more sensitive to the cool edge region of the plasma than the soft x-ray signal, which cuts off below about 2 keV. Also, magnetic probes are located all around the vacuum vessel and can therefore assist in eliminating the well-known "shadow effect" of tomographic inversion, i.e., that the regions far from the detectors are more poorly-reconstructed. Combining diagnostics will require modeling of the density, current, and temperature dependence of each signal as well as associated error bars to allow meaningful comparison between, for example, magnetic probes

and the SXR signal. Using a combination of diagnostics, especially magnetic probes and motional Stark effect measurements, is routinely used to reconstruct bulk MHD (Grad-Shafranov) plasma equilibria, but this method has not been applied to reconstruct MHD mode structures in DIII-D.

2.5 ELM propagation measurements

In conventional tokamak H-mode operation, Edge Localized Modes (ELMs) provide particle and energy exhaust from the core plasma. ELMs are beneficial for helping reduce the buildup of impurities in the core plasma, but also have the disadvantage of providing large transient heat loads on the divertor. These transient heat loads could cause divertor plate damage in future large tokamaks, so an understanding of ELM particle and heat transport is important for minimizing ELM heat loads while maintaining impurity exhaust.

The DISRAD-II fast radiometer has enabled measurements of ELM propagation by zonal analysis of the fast radiated power measurements. An example of observed ELM propagation for a lower-single-null plasma shot is shown in Fig.2.18. Here, the measured radiated emissivity of a single ELM is shown as a function of time for four different regions: the main chamber outer wall, the main chamber inner wall, the inner divertor, and the outer divertor. It can be seen that the ELM brightness begins to rise first in the outer wall, in support of a ballooning-mode origin for ELM formation, which predicts that ELMs are born near the outer midplane [24].

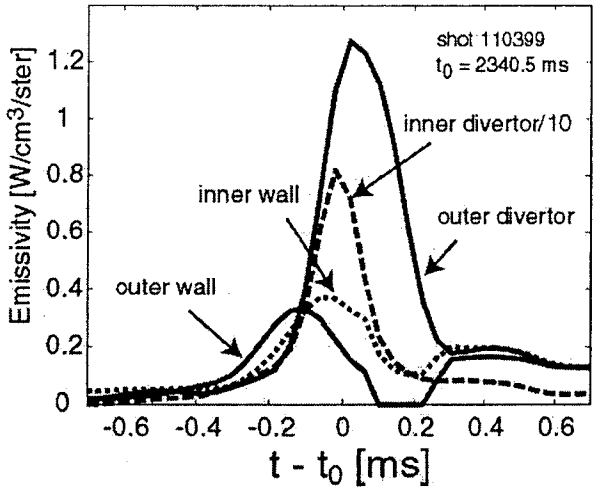

Fig. 2.18: Evolution of ELM emissivity as a function of time from DISRAD-II demonstrating initial rise in ELM radiation from the outer wall

Interestingly, Fig. 2.18 shows that the ELM emissivity is actually brighter in the inner divertor leg than the outer divertor leg. This is counterintuitive, since the connection length between the outer midplane and the outer divertor leg is shorter than between the outer midplane and the inner divertor leg. However, this result is consistent with other diagnostics, such as midplane D_α CID camera measurements and divertor thermography measurements.

Another counterintuitive result is that the estimated propagation time (the difference in peak emissivity) is shorter between the outer wall and inner divertor than it is between the outer wall and the outer divertor. This ordering is observed to change as a function of plasma (and ELM) density, as shown in Fig. 2.19, suggesting that collisionality effects might be playing a role here. As expected, the propagation time scales of Fig. 2.14 are consistent with ion-sound-speed parallel ELM propagation, rather that electron thermal velocity propagation. Overall, however, the results of Fig. 2.18 and 2.19 are not well-understood at present and will be the subject of further research in the coming grant period.

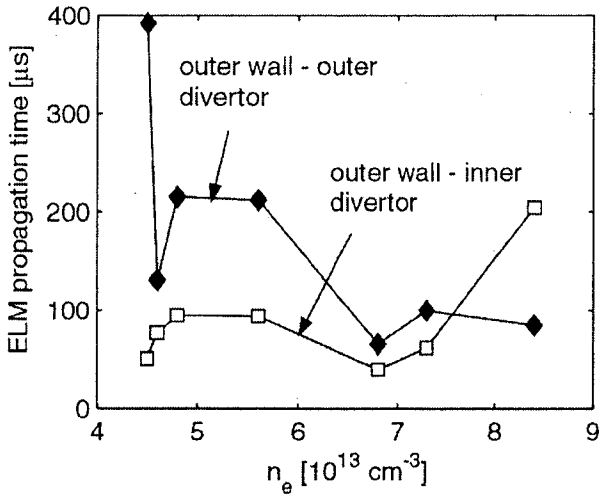

Fig. 2.19. Average propagation time of ELM emissivity peak as a function of pedestal density

2.6 Measurements and modeling of effect of DIII-D wall tile reflections

Visible light diagnostics, *e.g.* visible spectrometers, visible photodiodes, and CID cameras, are widely used to diagnose DIII-D and other tokamaks. Sometimes, it is possible to terminate the field-of-view of these diagnostics on viewing dumps such as razor blade stacks. Usually, however, the field-of-view is simply terminated on the vacuum vessel tiles. At UCSD, measurements and modeling efforts have been made to quantify the effects of vessel tile reflections on the accuracy of visible light diagnostics. It is found that the contribution of reflections is small (typically < 10%) for divertor view channels but can be significant (> 50%) for other view chords.

The reflectivity of an ATJ graphite wall tile was measured using a visible spectrometer, a calibrated turntable, and a collimated mercury lamp as a light source. Graphite reflection coefficients have been measured previously for specially prepared clean samples [25]. However, it is well-known that surface purity and roughness has a large effect on reflection coefficients, so the values obtained from an actual previously-used DIII-D wall tile where used in this study.

To quantify the expected effect of reflections on a typical visible light diagnostic, the Dα filterscope signals from DIII-D were analyzed. During normal operation, the Dα emission from the plasma comes dominantly from the colder edge region of the plasma. To model the effect of reflections, we therefore assume that the emission comes from four azimuthally-symmetric volumes: an inner divertor leg, an outer divertor leg, the private flux region, and the scrape-off-layer. These volumes, as well as the filterscope view chord geometry, are shown in Fig. 2.20. The emission volume boundaries are obtained from an EFIT reconstruction of the magnetic flux surfaces. The thickness of the scrape-off-layer is taken to be about 10 cm, corresponding to a typical neutral mean-free-path into the plasma edge.

Using the geometry of Fig. 2.20 together with measured Dα brightnesses and the known graphite wall tile reflection coefficients, the expected reflection contribution to the measured brightnesses could be obtained.

In order to understand the effects of these reflected Dα signals, a ray-tracing routine was written to integrate over the inside of the DIII-D volume assuming single bounces only. Figure 2.21 shows the measured Dα brightness (solid line), as well as the expected (single bounce) reflection contribution to the measured signal (broken lines) at the peak of an ELM. The dashed line

corresponds to a constrained solution where the reflection contribution is required to be less than the measured brightness, while the dotted line is the unconstrained solution. It can be seen that the upper array, which looks down into the divertor, is relatively unaffected by reflections. However, the much weaker main chamber signals are easily polluted by reflections from the bright divertor region; this is especially evident in lower view chords 4 and 8 in Fig. 2.21(b), since these view chords intersect tiles which are positioned close to the specular reflection angle for looking into the lower divertor.

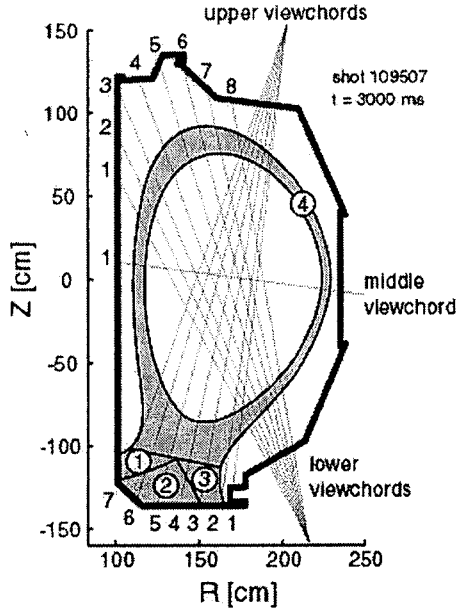

Fig.2.20. DIII-D filterscope view chords and emission volume geometry used to study wall tile reflections

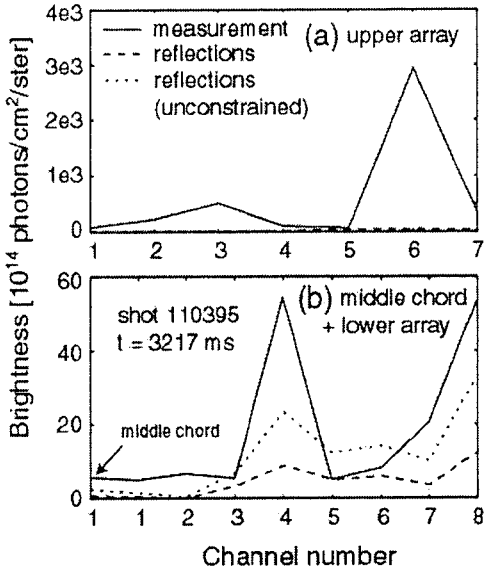

Fig. 2.21. Measured Dα brightness and calculated reflection contribution for (a) upper array and (b) middle chord and lower array during and ELM in DIII-D.

2.7 Disruption Radiometer Diagnostic DISRAD-II

In order to make progress in understanding disruptions and radiative processes in DIII-D we early recognized the need for fast time scale and spatially resolved radiated power measurements. The DISRAD diagnostic for DIII-D was planned in two phases. The Phase-I DISRAD was a single-chord, multi-detector diagnostic that uses UV filtering to investigate the efficacy of the AXUV diodes for radiometry with the emission spectrum in DIII-D, and provided experience with the AXUV detectors needed for the design of Phase II. The Phase-II DISRAD is a multi-chord diagnostic with a full poloidal view of the plasma.

2.7.1 DISRAD Phase I

The radiation observed by DISRAD from a disruption can be seen in Figure 2.22. Absolute calibration of the detectors and correction for the spectral response curve have yielded the first time-resolved measurements of the thermal quench. We find the peak brightness here to be approximately 190 W cm^{-2} sr^{-1}; the brightest disruptions observed to date have been up to about twice this bright. In this disruption, the thermal quench is complete before the current decay begins. The radiant energy we measure in the thermal quench (0.012 J cm^{-2} sr^{-1}) is much less

than we find in the current quench (0.39 J cm^{-2} sr^{-1}). The poloidal beta just before the disruption was $\beta_p = 1.1$ so the thermal stored energy should be close to the magnetic energy. The magnetic energy is an upper bound on the energy that can be radiated during the current quench. This suggests that most of the thermal energy in the plasma is lost either by radiation from regions of the plasma outside the view of the present single-chord diagnostic, or by mechanisms other than radiation. The Phase-II DISRAD will address this question.

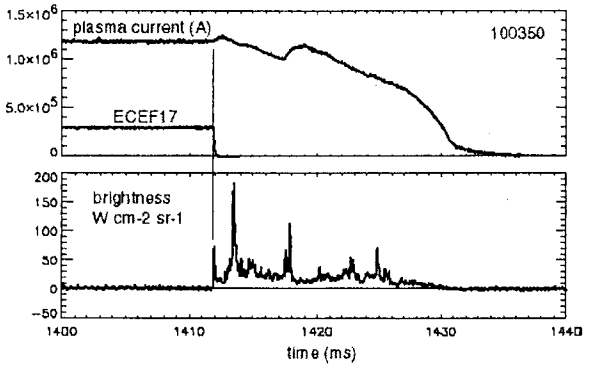

Fig. 2.22: Plasma brightness measured by DISRAD during a disruption in DIII-D. The thermal quench phase (period during which the ECE signal decays) is much shorter than the current quench phase. The radiated energy observed during the thermal quench phase by this single-chord diagnostic is small compared to the energy radiated in the current quench phase.

Figure 2.23 shows just the thermal quench phase of the same disruption. The radiation brightness is seen to decay with a characteristic time of about 0.13 ms, which is comparable to the decay time of the electron temperature as measured from ECE. The analog bandwidth of 170 kHz achieved in the detection circuit appears to be adequate for disruption measurements, judging from observations made so far.

The dynamic range requirement on the detection electronics is determined by the need to be able to measure both in disruptions and in normal, quasisteady plasmas. The brightness measured by DISRAD from a quasisteady discharge is shown in Figure 2.24, and compared with the equivalent channel of the bolometer diagnostic. The agreement is quite good, indicating that the DISRAD AXUV diode power calibration is confirmed by the independent measurement of the DIII-D bolometer.

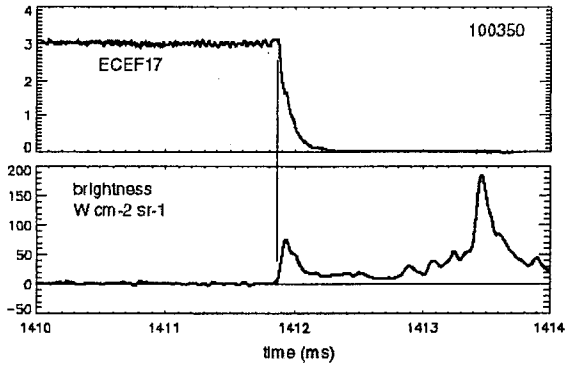

Fig. 2.23: Plasma brightness measured by DISRAD in the thermal quench phase of the same disruption. The observed decay time of the radiation is 0.13 ms, close to the decay time of the ECE signal.

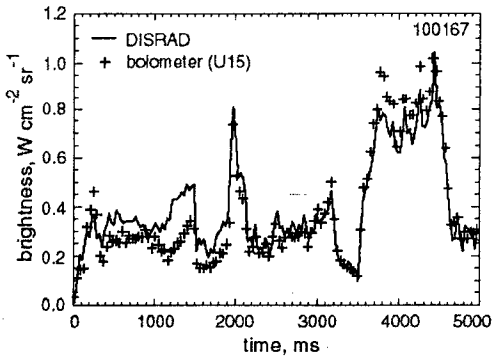

Fig. 2.24: Brightness observed by DISRAD (solid line) during a quasisteady discharge, compared to that measured by the bolometer channel that measures along essentially the same r-θ chord. The good agreement is an independent verification of the DISRAD calibration.

A major concern in employing AXUV photodiodes for radiometry in DIII-D has been that the spectral responsivity varies with photon energy. Our measurements in the past year have largely resolved this question. Optically filtered DISRAD measurements, together with data from the core SPRED spectrometer, indicate that this is not a serious problem during the current quench of disruptions, in which low energy radiation dominates. Using the measured emission spectrum and the manufacturer's spectral responsivity data, it has been found that an average responsivity of 0.12 ± 0.01 A/W can be used throughout the current quench. During quasisteady operation, substantial amounts of both soft X-rays and low-energy (< 20 eV) radiation are present, and the average responsivity is more variable (0.15 ± 0.05 A/W). During the thermal quench, it is likely that a large fraction of the radiation comes from carbon Kα, in the soft X-ray region. The fraction is not known from direct measurements, as this photon energy is too high to be seen by the SPRED and too low for the SXR arrays in DIII-D. Most likely the central responsivity value for quasisteady plasmas (0.15 A/W) is reasonably appropriate for the thermal quench.

2.7.2 DISRAD Phase II

In FY2001-03 the design of DISRAD-II was completed and the diagnostic was constructed and installed on DIII-D. After a successful campaign of measurements contributing to disruption mitigation studies and other experiments in FY2002, the diagnostic was overhauled with fresh detector arrays and improvements to the detection electronics and arrangement of view chords.

DISRAD-II provides spatially resolved measurements of radiated power, with 30 chords viewing the plasma at one toroidal location (Fig. 2.25) and up to 1 MHz bandwidth for disruption measurements. With 128K samples per channel, a full discharge can be recorded at a 10 kHz sample rate, or more than 0.1 sec at 1 MHz.

The main module (Fig. 2.25) contains two small cameras (Fig. 2.26), one for the lower fan of chords and one for the upper. Because much of the radiation to be measured is in the vacuum ultraviolet (VUV) and extreme ultraviolet (EUV) ranges, the cameras must be in the primary vacuum. Forced air cooling is provided during vessel bakes to avoid detector overheating. A shutter provides protection during boronizations and glow discharges.

Each of the two cameras contains a 16-element AXUV photodiode array (the same type used in the former, single-chord DISRAD-I diagnostic), which connects to a detection electronics module (Fig. 2.26). In order to provide bandwidth up to 1 MHz, the electronics modules are located as close as possible to the main module, and are hence exposed to magnetic fields from equilibrium and shaping coils. Amplifiers have been specially developed that are able to reject inductive pickup from these fields and provide measurements not only from disrupting plasmas but also from quasisteady plasmas, which are less bright by a factor of ~10^{-2}.

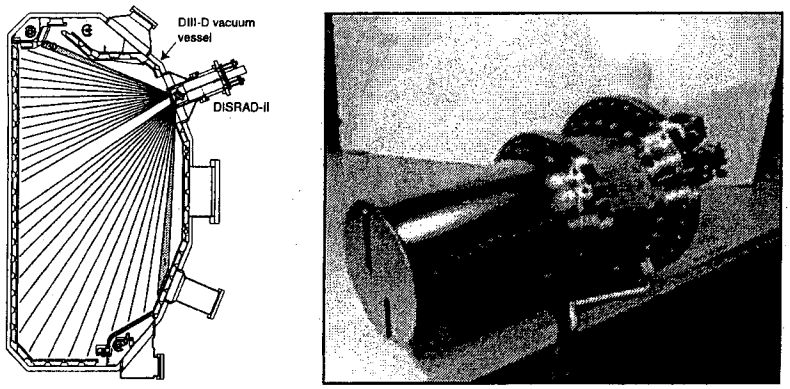

Fig.2.25. The fast radiated power diagnostic DISRAD-II views the plasma with 30 chords at one toroidal location, as shown on (left). The diameter of the front cover of the main module appearing in the photo (right) is seven inches.

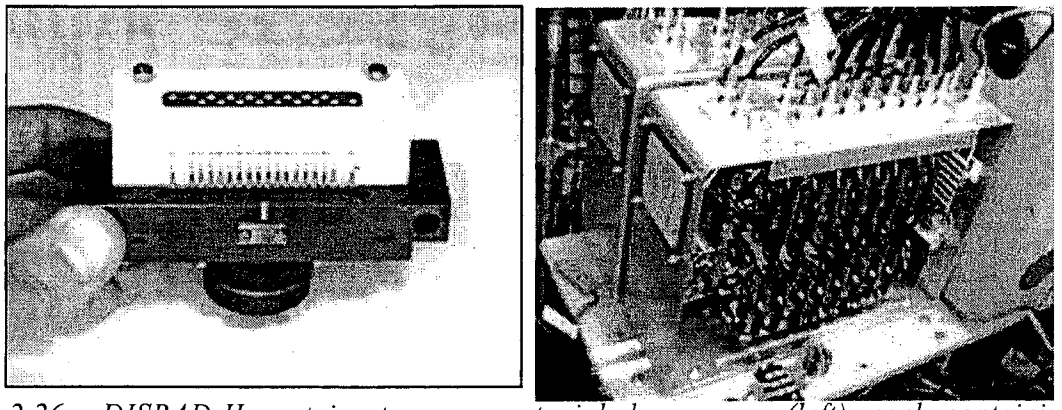

Fig. 2.26. DISRAD-II contains two compact pinhole cameras (left), each containing a photodiode array. Each array connects to a detection electronics module (right). The length of the electronics box is 12 inches.

Results from DISRAD-II in a high pressure gas jet mitigated disruption are depicted in Fig. 2.27. The surface plot shows the brightness measured in the 30 chords versus time. Using reasonable assumptions about the spatial distribution of the radiation along each chord, it is possible to calculate from the brightness data the total power radiated from the plasma. As can be seen from Fig. 2.27(right), instantaneous radiated power over 2 GW is achieved, and the plasma is almost completely extinguished in 3 ms from the beginning of the strong radiation. It was also found in these experiments that halo currents and runaway electron production were suppressed by the gas jet.

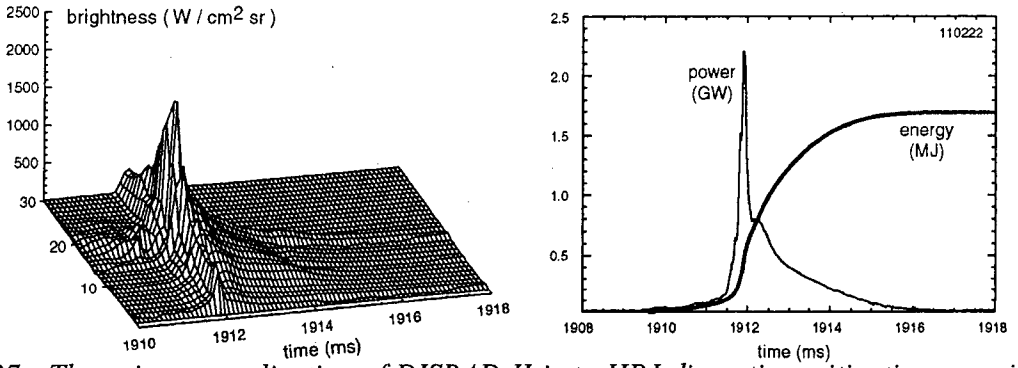

Fig.2.27. The primary application of DISRAD-II is to HPJ disruption mitigation experiment. The good spatial and time resolution of the diagnostic are evident. Importantly, the channels are absolutely calibrated so that the brightness and total radiated power and their time evolution can be measured.

There is interest in applying DISRAD-II also to measurements of fast transient phenomena other than disruptions, for example to ELMs. A higher sensitivity is required for such measurements, as less light is available. The DISRAD-II electronics can be switched to appropriate sensitivity settings. In early measurements of ELMs, however, the usefulness of the data was limited a higher noise level than was expected. As seen in Fig. 2.28, improvements to the diagnostic after the FY02 measurement campaign have substantially reduced problems with noise.

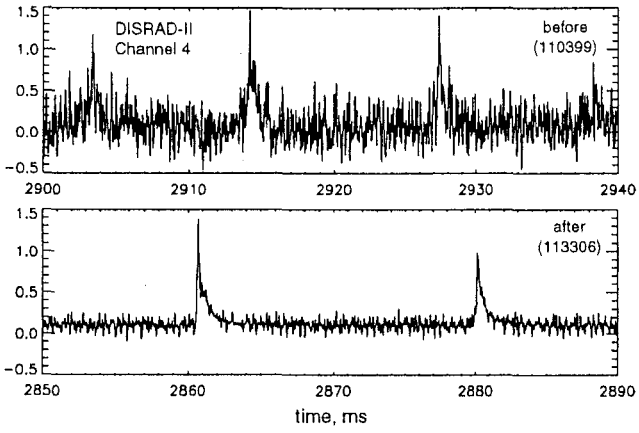

Fig. 2.28. Performance of DISRAD-II in non-disrupting conditions has been improved by recent modifications to the diagnostic. Two shots with ELMs are shown here. The clearer measurements in the lower plot are due to noise reduction and to subtraction of a newly available blind channel. In both cases, data are smoothed over 50 microseconds.

References for Section 2

[1] R. Parker, *et al.*, J. Nucl. Mater. **241-243** (1997) 1.

[2] D.G. Whyte, D.A. Humphreys, P.L. Taylor, Phys. Plasmas **7** (2000) 4052

[3] P.L. Taylor, *et al.*, Phys. Plasmas **6** (1999) 1872.

[4] D.G. Whyte, Phys. Rev. Lett. **81** (1998) 4392.

[5] T.E. Evans, *et al.* "The Production and Confinement of Runaway Electrons With Impurity Pellet Injection," GA-A22976 (1998) published in Proc. of the 17th IAEA Fusion Energy Conf., Yokahama, Japan, 1998.

[6] D.A. Humphreys, A.G., Kellman, Phys. Plasmas **6** (1999) 2742.

[7] D.A. Humphreys, D.G. Whyte, Phys. Plasmas **7** (2000) 4057.

[8] D.G. Whyte, *et al.*,"Energy balance, radiation and stability during rapid plasma termination via impurity pellet injections on DIII-D," 24th European Conference on Controlled Fusion and Plasma Physics, (Berchtesgaden) **21A** (1997) 1137.

[9] G. Federici, C. H. Skinner, J. N. Brooks, *et al.*, Nucl. Fusion **41** (2001) 1967.

[10] D. S. Gray Rev. Sci. Inst. **75** (2004) 376.

[11] E. M. Hollmann, D. S. Gray, D. G. Whyte, *et al.*, Phys. Plasmas **10** (2003) 2863.

[12] E. J. Strait, L. L. Lao, J. L. Luxon, and E. E. Reis, Nucl. Fusion **31** (1991) 527.

[13] P. L. Taylor, A. G. Kellman, T. E. Evans, *et al.*, Phys. Plasmas **6** (1999) 1872.

[14] M. R. Wade, T. C. Luce, and C. C. Petty, Phys. Rev. Lett. **79** (1997) 419.

[15] D. G. Whyte, T. E. Evans, A. W. Hyatt, *et al.*, Phys. Rev. Lett. **81** (1998) 4392.

[16] R. D. Stanbaugh *et. al.*, "DIII-D Three-Year Program Plan 1999-2001", General Atomics Report GA-A23056 (1999).

[17] O. Sauter, *et. al.*, Phys. Plasmas. **4** (1997) 1654.

[18] P. L. Taylor *et.al.*, Phys. Plasmas. **6** (1999) 1872.

[19] Y. Nagayama, *et. al.*, Phys. Plasmas. **3** (1996) 2631.

[20] R. A. Brooks and G. Di Chiro, Phys. Med. Biol. **21** (1976) 689.

[21] R. S. Granetz and P. Smeulders, Nucl. Fusion **28** (1988) 457.

[22] J. F. Camacho and R. S. Granetz, Rev. Sci. Instrum. **57** (1986) 417.

[23] A. Weller, *et. al.*, Rev. Sci. Instrum. **70** (1999) 484.

[24] P. B. Snyder, H. R. Wilson, J. R. Ferron, *et al.*, Phys. Plasmas **9** (2002) 2037.

[25] D.L. Greenaway, G. Harbeke, F. Bassani, and E. Tosatti, Phys. Rev. **178** (1969) 1340.

3. Boundary Physics and Turbulent Transport

3.1 Introduction

Since its inception in 1990, the UCSD experimental boundary physics collaboration has contributed to the DIII-D Program Mission *to establish the scientific basis for the optimization of the tokamak approach to fusion energy production* [1] by utilizing measurements from the UCSD/SNL reciprocating Langmuir probe arrays on the outboard mid-plane and in the lower divertor. Profile, fluctuation, electric field, flow parallel to $\boldsymbol{B}$, $\boldsymbol{E} \times \boldsymbol{B}$ drift, and transport flux measurements from these two probe arrays have been used, in conjunction with data from other boundary diagnostics, to advance our understanding of edge, SOL, and divertor physics, of L-H transition and transport barrier physics, and have aided the development of improved boundary plasma models.

In the period FY98–FY03, the UCSD experimental boundary physics group conducted research in support of the DIII-D Program primarily in the Transport and Boundary topical science areas and the Pedestal Thrust:

- **Transport Research:**
  - fundamental electrostatic turbulence and turbulent transport studies
  - physics of the $\boldsymbol{E} \times \boldsymbol{B}$ shear suppression of turbulence and transport
  - L-H transition and transport barrier physics
- **Boundary Research:**
  - characterization of radiation-enhanced divertor operation
  - parallel flows in the boundary and convective heat transport
  - $\boldsymbol{E} \times \boldsymbol{B}$ drifts in the divertor and X-point region
  - intermittent convective transport in the boundary
  - ELM heat and particle pulse propagation
- **Pedestal Thrust 1:**
  - H-mode pedestal physics and ELMs

In addition to furthering our understanding of how the tokamak core plasma couples to the wall through the edge and scrape-off layer (SOL), the results from this research have been used to guide the development of improved boundary plasma models such as UEDGE [2-8] and BOUT [9-11]. Ultimately, the fusion program needs a quantitative, self-consistent, predictive model of the boundary (edge, SOL, and divertor) region that can be used to establish the boundary conditions for predictive models of core performance.

3.2 Diagnostic upgrades and new capabilities: 1998-2004

Over four decades of research into transport in magnetic confinement devices has resulted in the identification of $\boldsymbol{E} \times \boldsymbol{B}$ turbulence as the source of anomalous cross-field transport in the ion channel [12]. In the two decades since the discovery of high confinement H-mode in the ASDEX tokamak [13], the understanding of $\boldsymbol{E} \times \boldsymbol{B}$ shear suppression of these ion modes has progressed sufficiently to allow its use to control anomalous transport [12]. However, today relatively little is known about electron temperature fluctuations in toroidal devices. What experimental measurements exist have come primarily from low power circular limiter tokamaks such as TEXT [14], TJ-I [15], and TEXTOR [16]. Because of the lack of information on the nature of T_e fluctuations in the boundary of shaped, diverted, high performance plasmas, the UCSD boundary physics group implemented fast T_e measurements on the outboard mid-plane probe using the

harmonic generation technique applied by Boedo at TEXTOR [16], beginning in 2000. Since then, three improvements to the diagnostic have been made:

- use of fully digital harmonic detection that eliminates phase delays characteristic of analog filtering [17]
- addition of drive voltage feedback, which significantly improved the dynamic range of the measurement.
- addition of a second channel of fast T_e measurements on the midplane probe and one channel on the X-point probe to study the poloidal structure of the T_e fluctuations in the boundary, and to improve the accuracy of the turbulent particle and heat flux measurements.

In addition, an upgrade of the mid-plane probe head to better conform all the tips to the same magnetic flux surface was undertaken in FY03. A survey of the poloidal inclination angles (with respect to the vertical) of the flux surfaces at the probe location has been performed for a number of different divertor configurations [lower single null (LSN), upper single null (USN), double null (DN)] and for inner wall limited (IWL) configurations. In all cases the poloidal inclinations were within the range of 14 ± 3.5 degrees. The modification improves the tip alignment for this angle (Fig. 3.1), further improving the accuracy of the turbulent flux measurements.

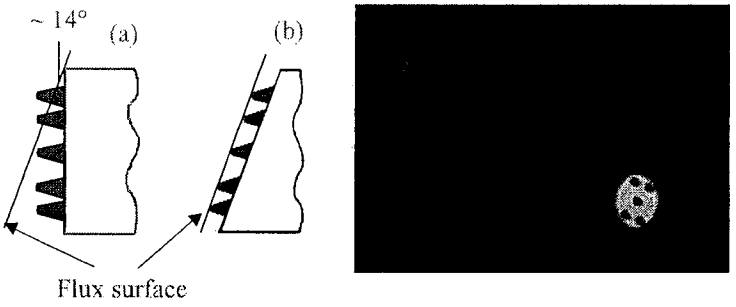

Fig.. 3.1: Poloidal view of the original (a) and modified (b) versions of the mid-plane probe head versus a typical flux surface (line). The modified head is shown on the right.

3.3. Plasma turbulence and transport

The fusion community has made considerable progress in understanding the origins of anomalous cross-field transport in tokamaks and in reducing the level of transport via E x B shear [12]. Nonetheless, we still lack both active control of anomalous transport (particularly electron heat transport) and a predictive capability for plasma transport. Achieving these goals is complicated by the large number of coupled dynamical processes that regulate the level of anomalous transport. For example, a reasonable model of the dynamical system for anomalous edge transport might look something like Figure 3.2. Considerable progress has been achieved in implementing such local transport models in numerical simulations. But quantitative verification of the results of such codes has been limited. The possiblity that other non-local transport processes, such as avalanches [18-20], might be important further complicates the picture. The detailed plasma profile, turbulence dynamics, and fluctuation-induced transport measurements obtained in this research will enable transport theories to be tested and numerical models to be validated. A more immediate and practical result of this research will be better understanding and control of plasma turbulence and anomalous transport in Advanced Tokamak regimes in DIII-D.

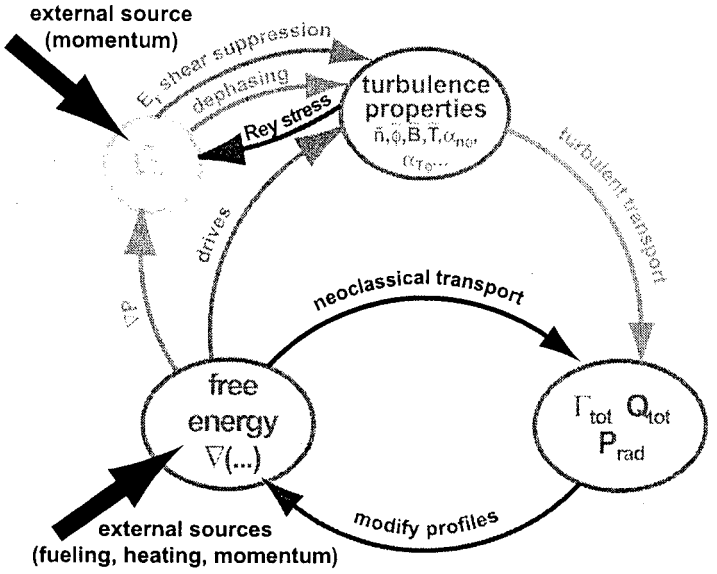

Fig. 3.2: A reasonable representation of a local transport model for anomalous edge transport in a tokamak

3.3.1 Complex Dynamics of Plasma Turbulence and Transport

Despite considerable progress in understanding and controlling anomalous transport in tokamaks [12], our understanding of the underlying dynamical processes leading to anomalous transport is still incomplete. Significant questions include: the origin of the observed universality of turbulent power spectra in toroidal devices [21,22], the origin of turbulence and transport in regions of the plasma that are below marginal stability to modes causing transport, the mechanism for rapid radial propagation (non-locality) of cold and heat pulses in experiments, and the origin of Bohm (device size) scaling of anomalous transport due to small spatial scale turbulence. Recently, theorists have considered transport models [18,19,20] based on the concept of self-organized criticality [23]. These models make several predictions about the behavior of turbulence and transport power spectra in the plasma frame of reference and transport probability distribution functions which are straightforwardly tested with existing diagnostics. In close collaboration with UCLA, UCSD scientists tested these predictions with data obtained in L-mode and ELM-free H-mode plasmas in DIII-D [24]. Power spectra of density fluctuations in the core and edge of L-mode and H-mode plasmas display significant f^{-1} ranges when measured with either reflectometry or Langmuir probes, as well as distinct regions of f^0 and f^{-4} as predicted in both cellular automata and plasma turbulence model realizations of SOC dynamics. In addition, floating potential fluctuations and the frequency-resolved particle transport flux $\Gamma(\omega)$ measured in the edge with Langmuir probe arrays also display these 3 distinct spectral ranges (Figure 3.3). Integration of $\Gamma(\omega)$ shows that the f^{-1} region of SOC-like interacting avalanches is important in L-mode, contributing 57% of the total transport (Figure 3.3).

Measurements of the instantaneous particle flux in the edge of both L and ELM-free H mode are characterized by bursts of high transport and intervals of low transport (Fig. 3.4). Transport model realizations of SOC dynamics predict a $1/\Gamma$ scaling of the probability distribution function of these transport events, which has been demonstrated for particle transport in the edge of DIII-D L modes for nearly 2 decades (Fig. 3.5). These measurements indicate that L-mode plasmas in DIII-D are in a state consistent with self-organized criticality.

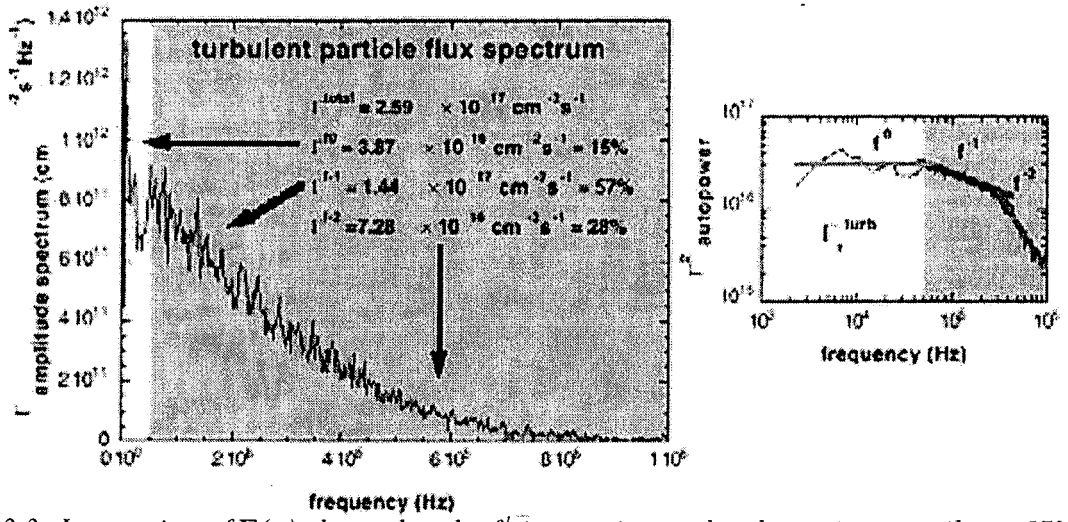

Fig. 3.3: Integration of $\Gamma(\omega)$ shows that the f^{-1} interacting avalanche region contributes 57% of the total transport

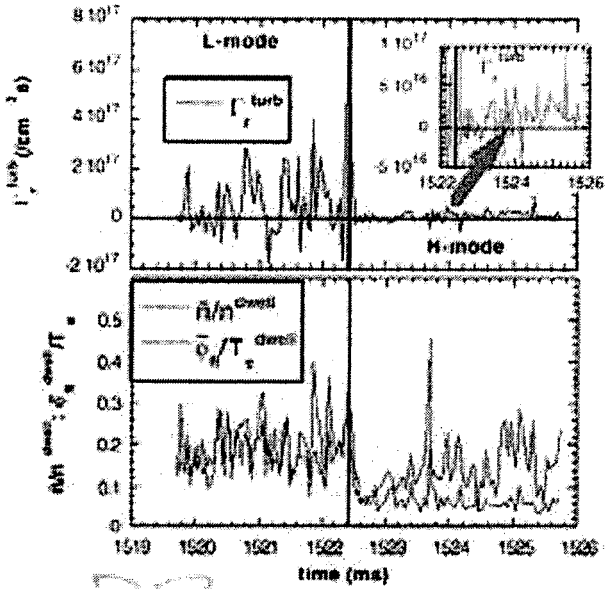

Fig. 3.4: Particle flux and normalized rms fluctuation amplitudes across an L to H transition in the edge of DIII-D. Inset is an enlargement of the H-mode flux, showing qua (Figure 3.3). Integration shows that the region of SOC.

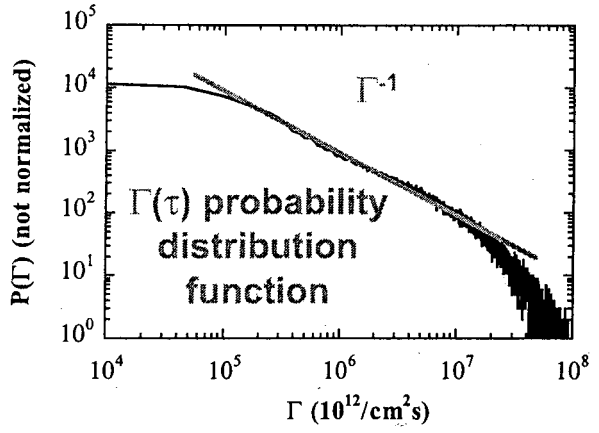

Fig. 3.5: The particle transport flux probability distribution function displays 2 decades of 1/ Γ scaling as predicted by SOC modeling

3.3.2 Turbulence Drives and E x B Shear Suppression

It is generally believed that edge gradients provide the drive (free energy source) for edge plasma turbulence. In ELM-free H-modes, fluctuation amplitudes often increase to near L-mode levels following the initial fast reduction at the L-H transition as the edge gradients increase (Fig. 3.6). Similar behavior is seen in L-mode just before the L to H transition (Fig. 3.7), suggesting that the edge turbulence drive is more likely to be due to the pressure gradient than either density or T_e gradients alone. Nonetheless, the complex variation of $\tilde{n}$with the pressure gradient in ELM-free H-mode (Fig. 3.6) clearly demonstrates a complicated picture similar to Fig. 3.2.

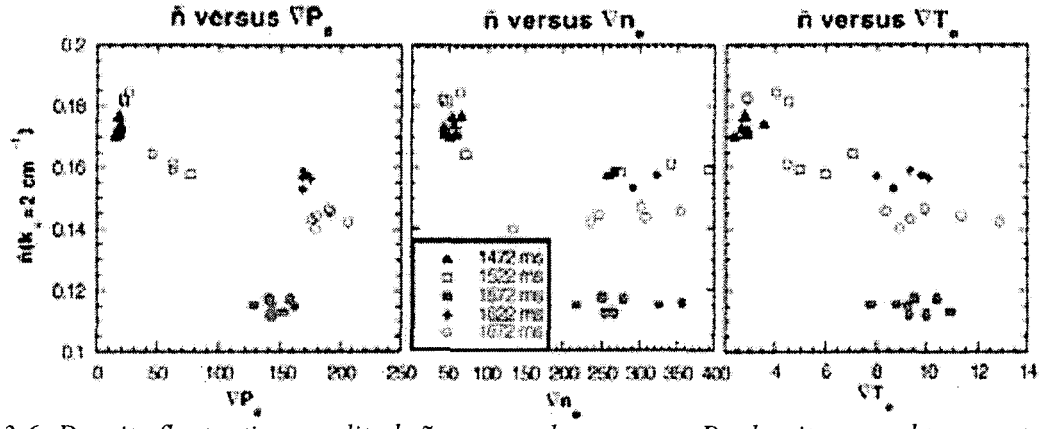

Fig. 3.6: Density fluctuation amplitude ñ versus edge pressure P_e, density n_e, and temperature T_e gradients in an ELM-free H-mode. Before 1572 ms, ñ falls despite an increase in the edge gradients due to increase E x B shear.

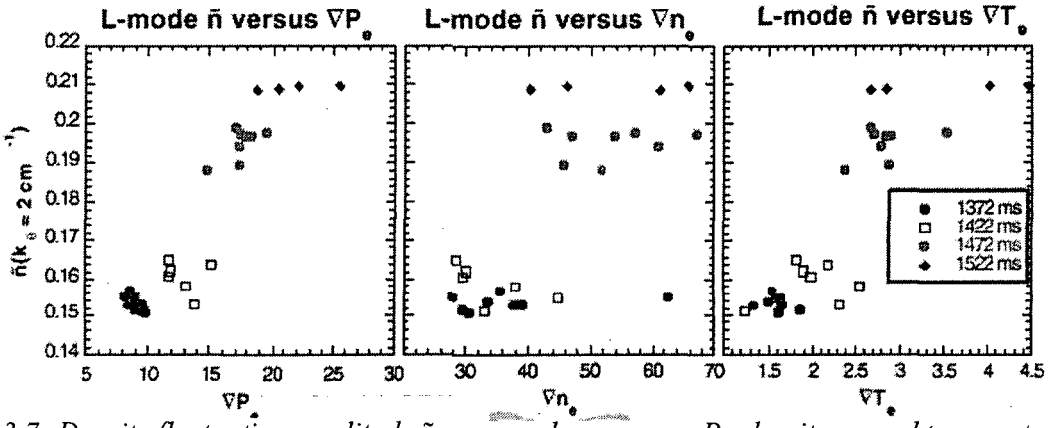

Fig. 3.7: Density fluctuation amplitude ñ versus edge pressure P_e, density n_e, and temperature T_e gradients in an L-mode

3.3.3 Electron temperature fluctuations and turbulent heat transport:

A comparatively new method for the measurement of electron temperature with high spatial and temporal resolution was implemented on the midplane fast reciprocating probe on DIII-D during the 2000 experimental campaign. The method is based on detection of harmonics generated in the current spectrum of a single Langmuir probe driven by high-frequency sinusoidal voltage [16] (Fig. 3.8) The probe on DIII-D was driven at 400 kHz thus allowing temperature measurements with a bandwidth of up to 200 kHz. A newly developed digital harmonic detection procedure has considerably improved phase resolution of the technique making it suitable for

turbulent heat flux measurements (Fig. 3.9). Initial results from DIII-D showed good agreement with swept double probe and Thomson scattering data. Diagnostic upgrades being implemented for the experimental campaign of 2000 include drive voltage feedback and capacitive leakage current compensation. Both upgrades are aimed at increasing accuracy and dynamic range of the measurements. Further upgrades are suggested including increase of the bandwidth to 500 kHz and addition of another channel in order to measure the wave numbers of the temperature fluctuations.

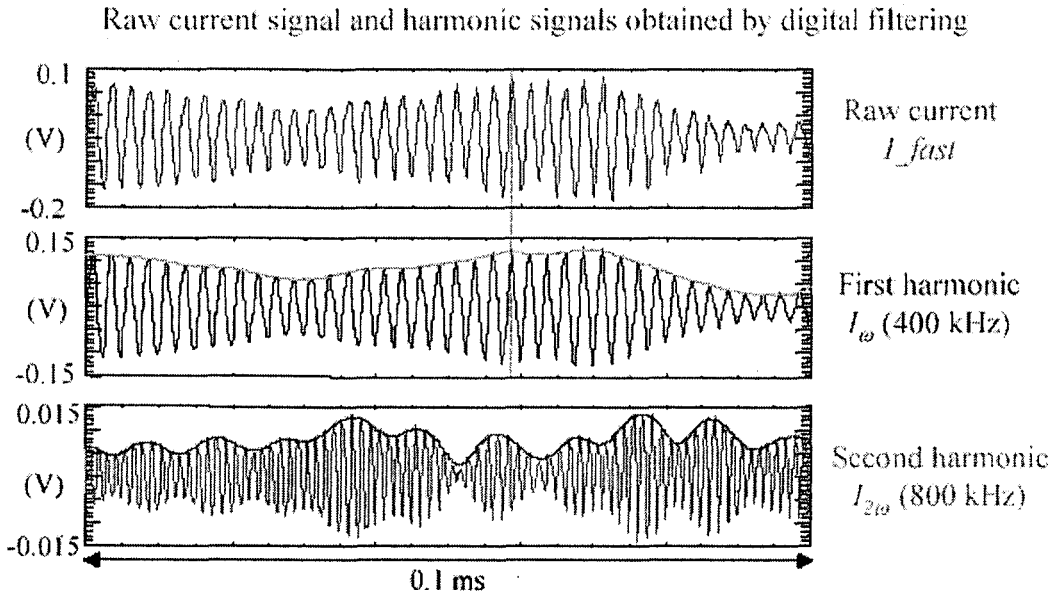

Fig. 3.8: Raw probe current and first and second harmonics

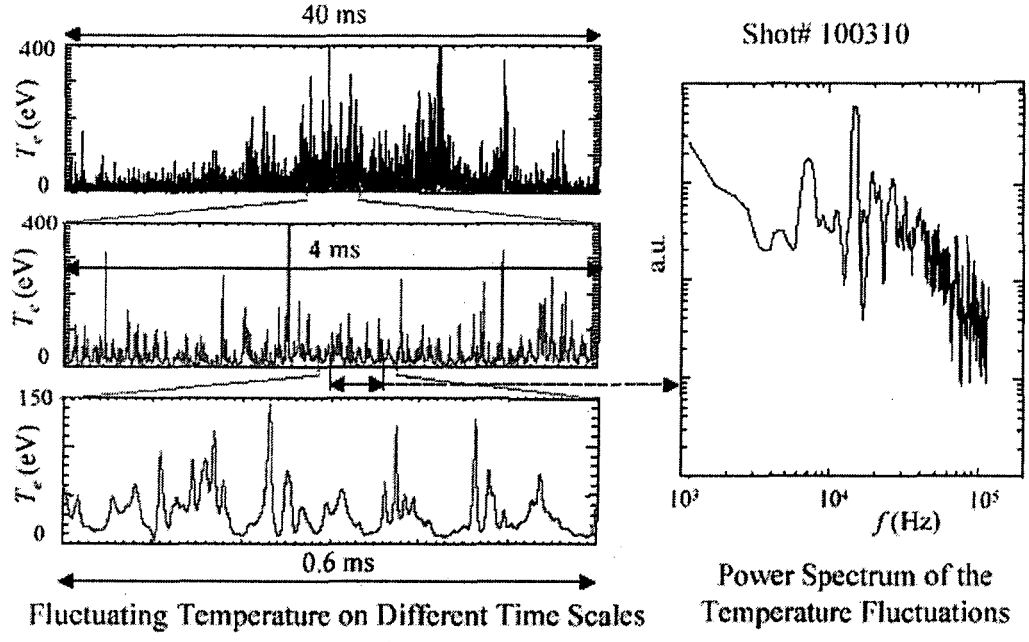

Fig. 3. 9: (left) T_e fluctuations on different time scales. (right) Auto-power spectrum of the T_e fluctuations.

The fast electron temperature measurement capability of the mid-plane reciprocating probe [17] has been used extensively for several years to characterize T_e fluctuations in the DIII-D boundary under a variety of conditions. The results of this research are being used to extend the knowledge of T_e fluctuation behavior in the boundary of high performance diverted tokamaks. Briefly, T_e fluctuations also have relative root-mean-square (RMS) levels ranging from 0.1–0.2 at the separatrix to 0.5–0.6 in the SOL, comparable to the levels of the density and floating potential (V_f/T_e) fluctuations (Fig. 3.10). The T_e and floating potential fluctuations have similar frequency spectra and poloidal wavenumbers (Fig. 3.11). At frequencies below 30 kHz, electron temperature fluctuations tend to be approximately in phase with both the electron density and the poloidal electric field fluctuations, leading of significant turbulent convective (associated with the turbulent particle flux) and conductive (due to correlation between T_e and poloidal electric field fluctuations) heat transport. Both convective and conductive terms of turbulent heat flux were measured in L and low power H-mode discharges. In H-mode, the two terms are comparable near the separatrix and fall off rapidly with radius. In L-mode the convective term is usually larger than the conductive one and radial decay is much slower. These results indicate that the H-mode transport barrier is primarily a particle transport barrier. Although T_e fluctuations are broadband with significant energy throughout the measurable range (up to 100 kHz), most of the heat transport occurs at frequencies below 30 kHz, (Fig. 3.11). Total heat flux through the separatrix at the mid-plane probe location in L mode and low-power H mode shots is typically around 10 W/cm^2 which is higher than expected from the power balance assuming poloidally symmetric transport. Possible explanations for this include poloidal asymmetry of the transport and/or overestimate of the transport rates due to limitations in the poloidal electric field E_θ measurements.

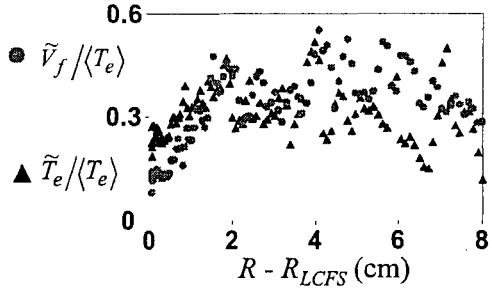

Fig. 3.10: Relative levels of the floating potential (purple circles) and electron temperature (blue triangles) fluctuations in the boundary of a DIII-D L-mode.

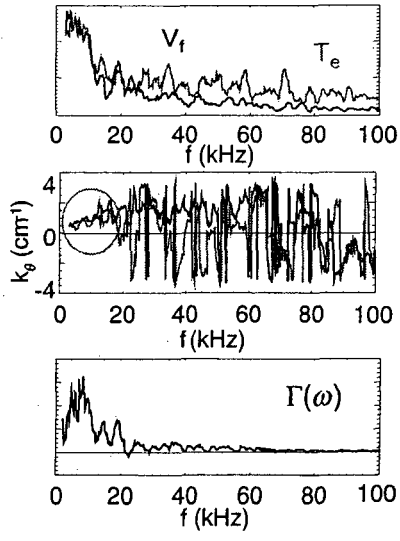

Fig. 3.11: Comparison of frequency-resolved spectral characteristics of floating potential (V_f, black) and electron temperature (T_e, blue) fluctuations: (top) frequency spectra, (middle) poloidal wavenumber k_θ and (bot) turbulent heat flux $\Gamma(\omega)$.

3.4 H-mode and transport barrier physics:

The confinement of high β plasmas in toroidal magnetic configurations is often limited by particle and heat transport due to plasma micro-turbulence [12]. Under suitable conditions, however, these plasmas undergo spontaneous transitions from low to high confinement states by formation of radially localized transport barriers in the plasma edge [13] and core [25]. These transport barriers result from the spontaneous formation of a sheared flow [26] which increases the decorrelation rate of turbulent eddies via eddy stretching in the direction of the flow [27]. In the initial theoretical work [28], the origin of the sheared flow was unspecified. In more recent work the sheared flow was proposed to evolve out of the turbulence in a self-organization process [29-35] driven by the turbulent Reynolds stress [36] which transports and concentrates turbulent momentum in a velocity shear layer. Viewed as a mode-coupling problem, the kinetic energy associated with the turbulent velocity fluctuations of the fluid is transferred to larger spatial scales via three-wave interactions [37,38]. Recently, UCSD scientists have studied the dynamics of $\boldsymbol{E} \times \boldsymbol{B}$ shear suppression and the L-H transition in four experiments to clarify the role of $\boldsymbol{E} \times \boldsymbol{B}$ shear induced cross-phase changes in turbulent transport suppression (Sec. 3.4.1) and to identify the underlying origin of the sheared radial electric field (Sec. 3.4.2-3.4.4).

3.4.1 Scaling of plasma turbulence suppression with velocity shear

With the discovery that spontaneous L-H transitions were accompanied by the spontaneous formation of a negative radial electric field E_r well just inside the last closed flux surface [26], significant focus was placed on the role of the negative E_r well in transport barrier formation. Experiments in the CCT and TEXTOR tokamaks, in which L-H transitions were triggered by inducing an edge E_r well (CCT [39]) or hill (TEXTOR [40]) demonstrated the importance of E_r for transport barrier formation. Subsequently, a variety of theories were developed that considered the stabilization of turbulence by $\boldsymbol{E} \times \boldsymbol{B}$ shear due to linear stabilization of modes [41,42] or nonlinear decorrelation of turbulence [43,44]. Scalings of the turbulence suppression with velocity shear, $|dv_E/dr|$ were derived for both the strong or weak shear regimes by considering the nonlinear turbulent decorrelation in a single fluctuating field, point model [28, 45,46]. Biglari, Diamond, and Terry found that for the strong shear regime the ensemble of fluid fluctuations normalized to its equilibrium value in a sheared fluid divided by the ensemble in a shear-free fluid is related to the shearing rate, ω_s, and the turbulent decorrelation time, $\Delta\omega_t$, by:

$$\hat{\Theta} \equiv \frac{\left\langle \left|\delta\hat{\xi}\right|^2 \right\rangle}{\left\langle \left|\delta\hat{\xi}\right|^2 \right\rangle_0} \approx \left(\Delta\omega_t/\omega_s\right)^{2/3} < 1 \qquad \textit{Eq. 1}$$

which results in a $|dv_E/dr|^{-2/3}$ dependence while [45] finds a $|dv_E/dr|^{-2}$ dependence in the weak shear regime. Further work by Zhang and Mahajan [46] aimed to unify and extend the theory, resulting in the relations:

$$\left\langle \hat{k}_\perp^2 \right\rangle \hat{\Theta} = 1 - \frac{4}{3}\left(\frac{|dv_E/dr|t_{c0}}{\alpha \left\langle \hat{k}_\perp^2 \right\rangle^{1-\gamma}} \right)^2 \quad \textit{weak shear} \text{ limit, } \textit{scales as Shaing} \qquad \textit{Eq. 2}$$

$$\left\langle \hat{k}_\perp^2 \right\rangle \hat{\Theta} = \left(\frac{\sqrt{3}\,|dv_E/dr|t_{c0}}{\alpha \left\langle \hat{k}_\perp^2 \right\rangle^{1-\gamma}} \right)^{-2/(3-2\gamma)} \quad \textit{strong shear} \text{ limit } \textit{scales as} \begin{cases} \textit{Biglari for } \gamma = 0 \\ V_0^{-2} \textit{ for } \gamma = 1 \end{cases} \qquad \textit{Eq. 3}$$

$$\left(\left\langle \hat{k}_\perp^2 \right\rangle \hat{\Theta} \right)^{-1} = 1 + 2\left(\frac{|dv_E/dr|t_{c0}}{\alpha} \right)^2 \quad \textit{arbitrary shear } (\gamma = 1) \qquad \textit{Eq. 4}$$

where $\langle \hat{k}_\perp^2 \rangle$ is the ratio of the averaged square of the perpendicular wave number with shear flow to that without shear flow, α measures the anisotropy of the k spectrum and $t_{c0} \equiv \sqrt{2}\left(\langle k_\perp^2 \rangle D\right)_0$ is the decorrelation time without shear flow that depends on the diffusion coefficient, D, and γ is a parameter between 0 and 1 determining the strength of the turbulent regime (i.e. γ=1 for weak turbulence or γ=0.5 for strong turbulence).

In these models, there was only one fluctuating quantity, and the turbulent transport depended only on the square of the rms fluctuation amplitude. Consequently, these models cannot predict the proper scaling of turbulent transport fluxes with $\boldsymbol{E} \times \boldsymbol{B}$ shear due to the important role played in transport reduction by changes in the cross-phase between pairs of fluctuating quantities ($\tilde{n}$ and $\tilde{E}_\theta$ for particle and convective heat transport; $\tilde{T}_e$ and $\tilde{E}_\theta$ for conductive heat transport) [47]. Ware and Terry [48] extended these single-field models to a two-field model of resistive pressure gradient driven turbulence. They derived expressions for the turbulence-driven particle flux Γ and density-potential cross-phase δ to the velocity shear in the weak shear limit:

$$\frac{\Gamma\left(|dv_E/dr|\right)}{\Gamma\left(|dv_E/dr|=0\right)} \approx 1 - 2.1\frac{\left(k_y |dv_E/dr| W_0\right)^2}{\gamma_0^2} \qquad Eq.\ 5$$

$$\cos\delta_k^n \approx 1 - 1.2\frac{\left(k_y |dv_E/dr| W_0\right)^2}{\gamma_0^2} \qquad Eq.\ 6$$

where γ_0 is the dominant mode linear growth rate and W_0 is the radial mode width without shear.

To test these predictions, the thin, (δr=1.5 cm) rotating $\boldsymbol{E} \times \boldsymbol{B}$ shear layer induced by an electrode in the edge of TEXTOR was characterized before the L-H transition with high-spatial resolution and correlated to the profiles of directly measured absolute and normalized turbulent quantities, including the turbulence-driven radial particle flux. It was found that the amplitude of the fluctuations was reduced in the sheared layer and that fact, coupled to changes in the cross-phase, resulted in reduced turbulent transport and improved particle confinement. It was also found that relatively low shearing rates were sufficient to affect the fluctuations and a scaling with shear was produced that was compared to the analytical theories above.

The variation of the normalized density fluctuation level Θ with shear is shown in Fig. 3.12 (solid circles). A fit (solid line) to the Zhang-Mahajan (Z-M) prediction for arbitrary shear (Eq. 4) is superimposed. The results of the fit are shown in Table 3.1 for all points and also for points where $dE_r/dr > 0$ or $dE_r/dr < 0$ and it becomes clear that the fitting parameters do not show any clear sensitivity to the sign of the shear. Further fitting of the same function but allowing the exponent to be an additional free parameter indicates that values of the exponent of up to 3.6 are possible, quite higher than the value of 2 predicted by Z-M. A large amount of physical information as related to the models can be obtained from the fits since the fitting parameters are defined as per Eq. 4 as:

$$m1 = \frac{1}{\langle \hat{k}_\perp^2 \rangle} \qquad m2 = \frac{t_{c0}}{\alpha}$$

By using a value of the de-correlation time t_{c0} of ~1-4 10^{-5} s^{-1} inferred from correlation techniques, α= 10-35 (the fluctuation spectrum is very anisotropic) and $\langle \hat{k}_\perp^2 \rangle$=0.98 (the average normalized $k_\perp$ does not change much).

Table 3.1: Fits to the normalized density

Function	m1	m2	γ	χ^2	Case
$y=m1/(1+2*(m2*V)^2)$	1.018	$8.865*10^{-7}$	2.0	0.15736	**All points**
	0.943	$9.156*10^{-7}$	2.0	0.0115	**dE/dr >0**
	1.103	$9.180*10^{-7}$	2.0	0.1155	**dE/dr <0**
$y=m1/(1+2*(m2*V)^\gamma)$	0.964	$1.032*10^{-6}$	3.6	0.129	**All points**

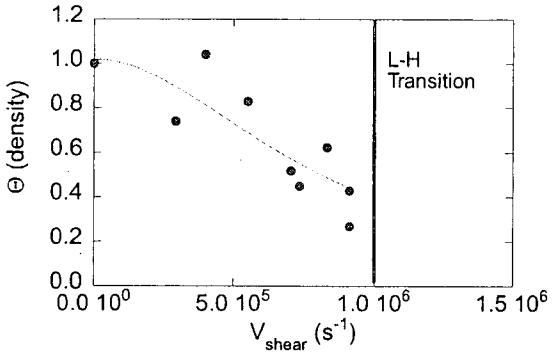

Fig. 3.12: Scaling of normalized density fluctuations with shear (solid circles) and the fit by the Z-M prediction (line). The shear at which the L-H transition occurs is marked.

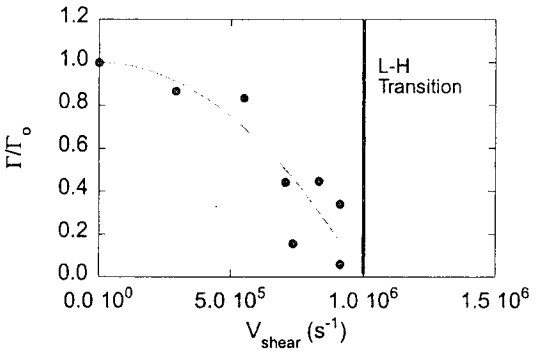

Fig. 3.13: Scaling of normalized radial particle flux with shear (solid circles) and the fit (solid line) based on Ware-Terry predictions.

The normalized particle flux scaling with shear is shown in Fig. 3.13 (solid circles) as well as the fit to the Ware-Terry prediction (Eq. 5) for weak shear. The results of the fit are shown in Table 3.2. Additional fits were performed with the exponent as a free parameter and only a 20% difference is observed in the fitting parameters.

Table 3.2: Fits to the radial flux Γ

Function	m1	γ	χ^2	Case
$y=1-2.1*(m1*V)^2$	$6.92*10^{-7}$	2.0	0.179	**All points**
$y=m-2.1*(m1*V)^\gamma$	$6.22*10^{-7}$	1.67	0.173	**All points**

To test the shear dependence of the density-potential cross-phase δ^n, we write the particle flux in the time domain as:

$$\tilde{\Gamma}_r = \frac{\langle \tilde{E}_\theta \tilde{n}_r \rangle}{B_\phi} = \frac{\langle \tilde{n}_e^2 \rangle^{1/2} \langle \tilde{E}_\theta^2 \rangle^{1/2}}{B_\phi} \gamma_{\tilde{E}\tilde{n}} \sin \delta^{nE_\theta}$$

The measurement-inferred quantity $\gamma\sin\delta^{nE\theta}$ (coherence times the sine of the density-poloidal field cross-phase = coherence times the cosine of the density-potential cross-phase) is plotted in Fig. 3.14 as a function of shear. Since the coherence is reduced only by 15% as shear increases, the reduction seen with shear can be mostly attributed to cross-phase effects. The plot differentiates data in the dE/dr>0 region (solid symbols) from that in the dE/dr<0 region (open symbols) and H-mode data (squares) from L-mode data (circles). The data has been fitted with a

generalized function *a la* Ware-Terry (Eq. 6) with variable or fixed (to $\nu = 2$) exponent and the fitting parameters are shown in Table 3.3. The first four rows of Table 3.3 indicate that there is a measurable difference between the data in the dE/dr>0 that in the dE/dr<0 region for both variable (first two rows) and fixed (third and fourth rows) exponential. The fits are shown in Fig. 3.14 as thick solid and dashed lines respectively. An important immediate conclusion of Fig. 3.14 is that the cross-phase term plays an important role in the suppression of the particle flux, as crucial as that of the amplitudes of the fluctuations. H-mode data (squares) can be added to this dataset to drive the important point that the cross-phase term can become ***negative*** and therefore drive the particle flux inward. A fit to the whole dataset including the H-mode data is shown as dash-dottted lines in Fig. 3.14 corresponding to fixed (ν=2) and variable exponent. The best fit is obtained for ν=2.6 as seen in the last two rows of Table 3.3.

Table 3: Fits to the cross-phase

Function	m1	m2	γ	χ^2	Case
$y=m2+m1*V^{\nu}$	$-3.3*10^{-12}$	0.47	1.78	0.00017	**dE/dr >0 no H-mod**
	$-8.3*10^{-23}$	0.46	3.6	0.0135	**dE/dr <0 no H-mod**
$y=m2+m1*V^2$	$-1.6*10^{-13}$	0.47	2.0	0.99	**dE/dr >0 no H-mod**
	$-2.9*10^{-13}$	0.49	2.0	0.85	**dE/dr <0 no H-mod**
$y=m2+m1*V^{\nu}$	$-7.1*10^{-17}$	0.47	2.6	0.025	**All points**
$y=m2+m1*V^2$	$-3.23*10^{-13}$	0.50	2.0	0.034	**All points**

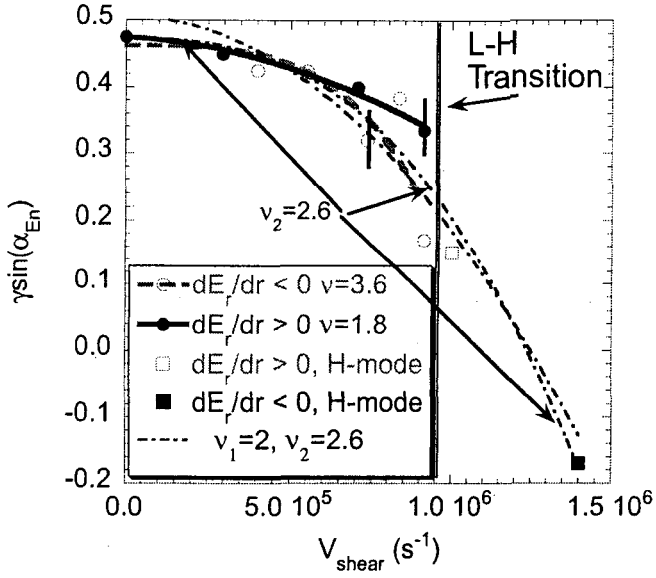

Fig. 3.14: Scaling of the cross-phase term with shear for the dE/dr>0 region (solid symbols), and the dE/dr<0 region (open symbols) including H-mode data (squares) and L-mode data (circles). Fits excluding the H-mode data (circles only) are shown as a solid line for dE/dr>0 and a dash line for dE/dr<0. The dashed-dotted lines show fits to the complete dataset.

Two important results should be noted: 1) the scaling of the cross-phase term is as strong as that of the turbulence amplitudes, confirming that the cross-phase is a key element in the suppression of turbulent transport, as first reported by Moyer et al. [37], and 2) there is a difference in the scaling of the cross-phase between the positive and negative shear regions, an effect not included in the theories, but deduced by Moyer et al. In earlier work [37].

3.4.2 Slow L-H transitions and IM-mode:

The dynamics of the L-H transition were explored in an experiment in which slow L-H transitions involving periodic instability bursts due to edge relaxation oscillations formed an intermediate state between L and H modes, the so-called IM-mode [49,50]. In this mode particle and energy confinement increase over L-mode values. The duration of this regime can be controlled by the neutral beam heating power. IM-mode is characterized by edge relaxation oscillations that are consistent with a predator-prey type of coupling between fluctuations and shear flow [51]. The "prey" instability—electron temperature fluctuations—was observed directly by the reciprocating probe using the fast T_e diagnostic [17]. The "predator"—shear flow—was inferred from BES data showing an increase in the poloidal phase velocity of the mode when the mode amplitude decreases and the probe data showing the presence of large bursts of plasma potential and potential gradients. IM-mode oscillations are illustrated in Fig. 3.15 showing data from the plunging probe located just inside the separatrix at $\rho = 0.994$. The D_α signal is plotted as a timing reference (blue trace) in all four plots. The relative timing of the signals is consistent with the predator-prey model. Fig. 3.16 shows radial profiles of the plasma potential near the separatrix inferred from the probe data during and between the instability bursts, showing the formation of a negative E_r in the edge between the bursts, providing support for the Reynolds stress as the origin of the E_r shear. It is also interesting to note that similar self-generated oscillations have been previously observed in the H-1 Heliac [52].

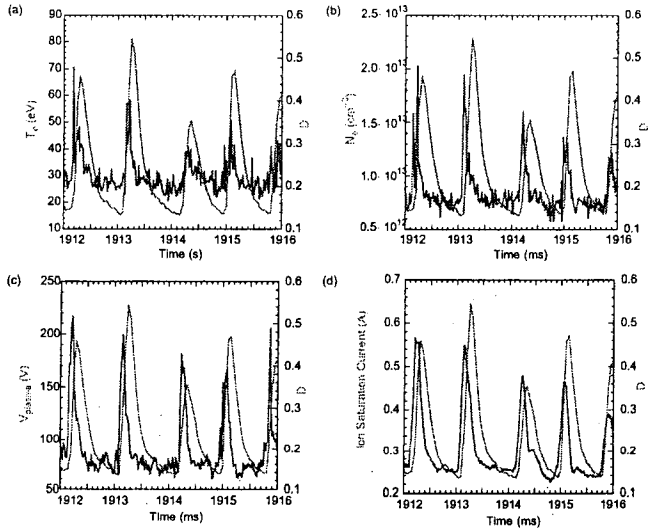

Fig.3.15: Electron temperature (a), electron density (b), plasma potential (c) and ion saturation current (d) measured by the mid-plane reciprocating probe at $\rho = 0.994$ in IM-mode. D_α signal (blue trace) is shown for timing reference.

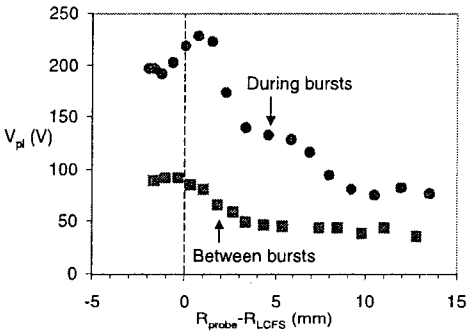

Fig. 3.16: Radial profiles of the plasma potential V_{pl} near the separatrix during (black circles) and between (red squares) the instability bursts. Between each burst, the fluctuations damp and the plasma potential in the boundary becomes less positive.

3.4.3 Search for evidence of Reynolds stress-driven flows—bispectral analysis:

The process by which the electrostatic Reynolds stress $< \tilde{v}_r \tilde{v}_\theta >$, where $\tilde{v}_r$ and $\tilde{v}_\theta$ are the fluctuating radial and poloidal velocities respectively and the "< >" denote an ensemble average, transports and concentrates turbulent momentum in a velocity shear layer, has been reformulated

as a 3-wave coupling problem, transforming the search for changes in the Reynolds stress and shear flow into a related study of the bispectrum of the potential fluctuations $B_{k_3}(\mathbf{k}_1,\mathbf{k}_2) \equiv \langle \phi(\mathbf{k}_3)\phi(\mathbf{k}_1)\phi(\mathbf{k}_2)\rangle$ [35,37,38] An increase in the shear flow energy due to the Reynolds stress should thus be accompanied by an increase in the bispectrum [35,37]. An increase in the bispectrum can occur via increases in the turbulence or shear flow amplitudes, and/or by an increase in the coherence between different fluctuation scales. Since the turbulence and shear flow amplitudes do not change significantly prior to the L-H transition [47], changes should be seen in the 3-wave phase coherence across the transition using the (squared) auto-bicoherence

$$\hat{b}^2_{k_3}(k_1,k_2) \equiv \frac{\left|B_{k_3}(k_1,k_2)\right|^2}{\left\langle\left|\phi_{k_3}\right|^2\right\rangle\left\langle\left|\phi_{k_1}\phi_{k2}\right|^2\right\rangle}$$

which provides a measure of the significance of phase-coherent 3-wave interactions with $\boldsymbol{k}_3=\boldsymbol{k}_1+\boldsymbol{k}_2$ [38], independent of the fluctuation amplitude. The **k** domain results are transformed into the frequency domain using the frozen-flow hypothesis: $f \propto k_\theta$. As there is no Doppler shift for the shear flow (because it has $k_\theta \sim 0$) the low-frequency (f~0) nature of the sheared flow is retained. Therefore the coupling between small scale turbulence and large scale shear flows should be manifested as simultaneous coupling among triads of frequencies $f_1 \approx f_2 \approx 100$'s kHz and the corresponding difference frequencies $f_3 << f_1, f_2 \approx 0$ kHz.

The structure of the 3-wave coupling is indicated by the squared auto-bicoherence in frequency space $\hat{b}^2_{f_3}(f_1,f_2)$ [Fig. 3.17]. At each (f_1,f_2) the degree of phase-coherence for triad interactions with $f_3=f_1\pm f_2$ is plotted; the $f_2>0$ triangle corresponds to sum coupling $f_3=f_1+f_2$, and is bounded on the left at $f_1=f_2$ by symmetry and on the right by $f_3=f_N$ since frequencies above f_N are not measured. The $f_2<0$ region corresponds to difference coupling $f_3=f_1-f_2$ and is bounded on the left at $f_1=-f_2$ by symmetry and on the right by $f_3=0$. In early L mode [Fig. 3.17(a)], there is little structure to the 3-wave coupling. Just before the transition, [Fig 3.17(b)] significant coupling develops between pairs of high (400-1000 kHz) and low-to-intermediate difference frequencies (20-200 kHz). Just after the L-H transition [Fig. 3.17(c)], this coupling has shifted to nearly equal high and smaller difference frequencies ($f_1 \sim f_2 \sim 300$-1200 kHz; $f_3<60$ kHz) in the presence of broadband coupling that may result from an increase in the "burstiness" of the signal. By 6 ms after the transition, ∇P_e is 3× larger, the broadband coupling has disappeared, and only coupling between nearly equal high and low difference frequencies remains ($f_1 \sim f_2 \sim 100$-1000 kHz; $f_3<50$ kHz) [Fig. 3.17(d)]. This coupling eventually disappears more than 10 ms after the transition.

Bispectral analysis of data 7 mm outside the separatrix show no such temporal variation, indicating that the bicoherence where measured changes only in the region of the strong shear flow. The time dependence of the total bicoherence

$$b^2 \equiv \sum_{f_1}\sum_{f_2} b^2_{f_3}(f_1,f_2)$$

(a measure of the relative strength of nonlinear coupling integrated over all scales) is shown in Fig. 3.18 inside (-3 mm) and outside (+7 mm) the separatrix, and indicates the temporal and spatial localization of the changes relative to the L-H transition.

These results indicate that 3-wave coupling between low and high frequencies (large and small scales) increases just before and during the L-H transition. This transient increase 1) starts *before* the turbulence reduction and rapid increase in E × B shear flow; 2) occurs in the region of

increased velocity shear; and 3) decays within a few milliseconds after the L-H transition. These results are consistent with expectations for a transient Reynolds stress driven zonal flow triggering the L-H transition [53,54]. In these models, as the Reynolds stress decays, the increased pressure gradient sustains a mean (diamagnetic) shear flow distinct from the initial Reynolds stress shear flow in the steady-state H-mode.

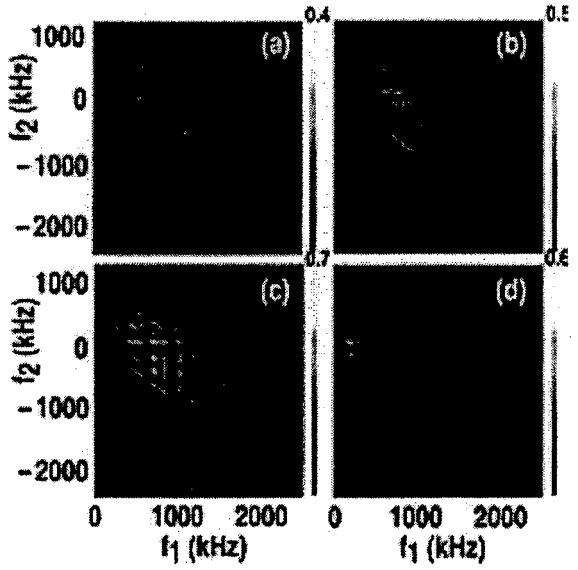

Fig. 3.17: Auto-bicoherence $\hat{b}^2_{k_z}(k_1,k_2)$ of I_{sat} 3 mm inside the separatrix (a) 15.5 ms before, (b) 2.5 ms before, (c) 2.5 ms after, and (d) 6.1 ms after the L-H transition.

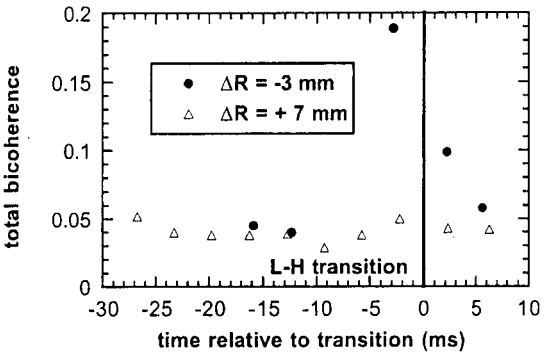

Fig. 3.18: Evolution of the total bicoherence of I_{sat} 3 mm inside (●) and 7 mm outside (Δ) the separatrix.

3.4.4 Evidence for Reynolds stress driven flows: zonal flows and GAMs

A coherent oscillation in the poloidal flow of density fluctuations that shows remarkable similarity to predicted characteristics of geodesic acoustic modes (GAM), a class of high frequency zonal flows, has been observed using beam emission spectroscopy (BES) on DIII-D [55]. Zonal flow features observed in the flow-field of the density fluctuations are believed to be associated with the oscillating potential and corresponding $\boldsymbol{E} \times \boldsymbol{B}$ fluctuations of the GAM. To investigate this, potential fluctuations were measured directly with the reciprocating Langmuir probe just inside the last closed flux surface. In a relatively low power discharge (with neutral injection power of 2.5 MW), the probe was inserted to approximately r/a=0.98. The probe independently measured both the floating potential (V_f) and ion saturation current (I_{sat}) fluctuations. The spectra for each are shown in Fig. 3.19(a) and (b). The potential in Fig. 3.19(a) shows a coherent fluctuation near 12.5 kHz at t=1500 ms, consistent with the BES flow measurements slightly before in the discharge. Fig. 3.19(b) indicates that there is little or no density (I_{sat}) fluctuations at the same frequency. This is consistent with the expectation that the GAM oscillation is a potential fluctuation with little or no associated density perturbation. The BES measurements showed no detectable density at the GAM frequency near the separatrix, while a modest fluctuation was observed deeper in the plasma. The probe measurements thus indicate a localized potential fluctuation at the GAM frequency, and so it is reasonable to expect an associated radial electric field and resulting $\boldsymbol{E} \times \boldsymbol{B}$ oscillation of the turbulence flow at this frequency, consistent with the BES flow measurements.

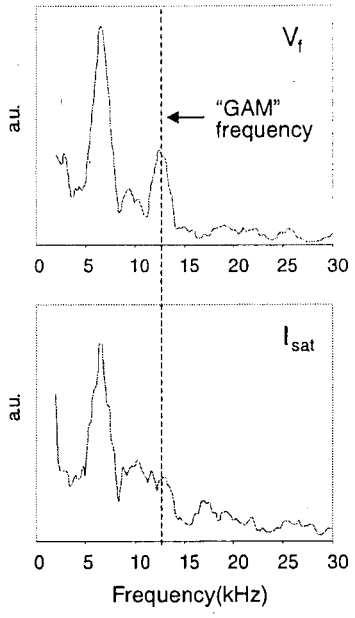

Fig. 3.19: Frequency spectra of the floating potential (a) and ion saturation current (b) fluctuations measured by the mid-plane reciprocating probe just inside the separatrix (r/a ≈ 0.98). The potential shows a peak near GAM frequency (12.5 kHz) while there is little or no density (I_{sat}) fluctuations at the same frequency

3.5 Edge-Scrape-off Layer Coupling and H-mode Physics

Significant progress was made in understanding the role of edge-scrape-off layer coupling for L-H transition physics and boundary turbulent transport in the period CY1998-2003. UCSD scientists studied the phase transition dynamics of very slow L to H transitions in which the transition speed and magnitude of fluctuation amplitude reduction were altered by the presence of a MARFE at the divertor X-point in L-mode. The time scale for the L-H transition was determined by the time to extinguish the MARFE, showing that boundary physics plays a role in L to H transition dynamics. Subsequent measurements with the X-point probe array showed that the plasma potential peaked strongly at the X-point, producing very strong circulation or flow of particles in the lower divertor around the X-point, directly linking the inner and outer divertor volumes.

A major thrust in CY98-03 for the H-mode working group has been an effort to understand the origin of the large increase in the H-mode power threshold when the ∇B drift is directed away from the divertor X-point in single null divertor plasmas. Reversing the ∇B drift is achieved by reversing the direction of B_T which reverses the direction of the E x B drifts around the X-point. In addition, the X-point region becomes strongly turbulent in the "reversed B" case (∇B drift away from the X-point), and there is some evidence that plasma flows in the boundary, as indicated by the sign of E_r, also reverse. These results all suggest that coupling of the scrape-off layer to the plasma edge, and in particularly plasma parallel and E x B flows, may be the origin of the higher H-mode power threshold in cases where the ∇B drift is away from the X-point.

3.6 Divertor and SOL Studies:

3.6.1 Parallel Flows

Measurements of the parallel Mach number of background plasma in the DIII–D [56] tokamak divertor were performed using a fast scanning Mach probe [57]. The parallel particle flow shows evidence of reverse flow, i.e., flow away from the target plate, stagnant flow, and large scale convection. Measurements perfomed in the outer divertor leg of attached discharges show classical acceleration of the plasma towards the divertor target (Fig. 3.20). However, increased

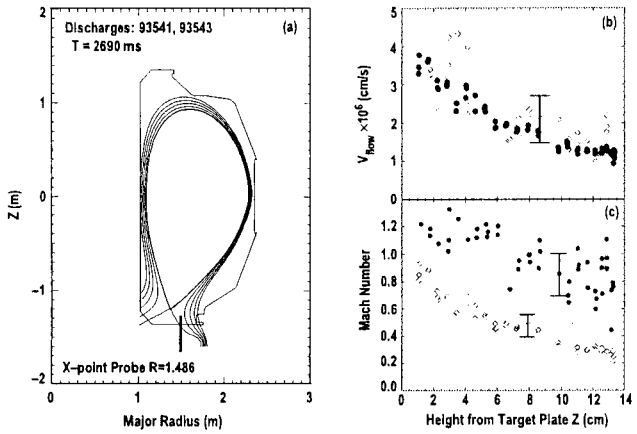

Fig. 3.20: a) Magnetic geometry for parallel flow measurements in the outer divertor leg, b) parallel flow velocity for attached (open symbols) and detached (solid symbols) discharges and c) corresponding Mach numbers.

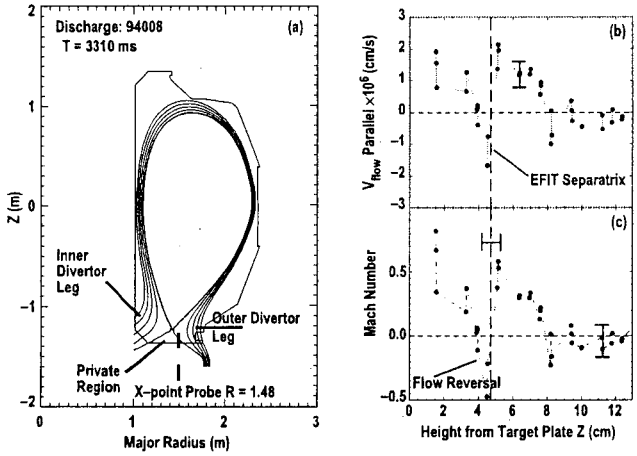

Fig. 3.21: a) Magnetic geometry for flow measurements in the private flux region and across the separatrix into the outer divertor leg in attached plasmas b) parallel flow showing the flow reversal region at the separatrix and c) corresponding Mach number.

recycling can cause a region of flow reversal at or near the outer separatrix, as seen in Fig. 3.21 thereby confirming the existence of a mechanism by which impurities can be transported away from the divertor target plates. In detached discharges, the Mach number and density increase as the temperature decreases, resulting in large convection all over the divertor volume towards the divertor target plate at near sound speed over large regions in the divertor, as seen in Fig. 3.20 and confirming predictions. We find that modeling results from the 2–D fluid code UEDGE [58] can reproduce the main features of the experimental observations, namely the thin region of flow reversal (Fig. 3.22) in attached disharges and convection over large volumes as shown in Fig. 3.23. The parallel heat flux is also dependent on the fluid velocity and can be expressed, following Braginskii [59], in terms of the bulk fluid velocity $V_{||}$, the electron density n_e, the parallel thermal conductivity $\kappa = \kappa_1 T_e^{5/2}$ the atomic ionization potential I_0 and the gradient along the magnetic field length:

$$q_{||} = \kappa_1 T_e^{5/2} \frac{\partial T_e}{\partial s} + n V_{||}\left[\frac{5}{2}(T_e + T_i) + \frac{1}{2} m V_{||} + I_0\right] \qquad \text{Eq. 7}$$

During detached divertor conditions, the conduction term in Eq. (7) is essentially zero because of the extremely low temperature and parallel temperature gradient [60] and, therefore, the convection terms dominate. Reduction of the heat flux to the plate can be accomplished by a reduction of density or parallel fluid velocity (i.e., $\Gamma_{||}$) or temperature, because the last term, I_0, is

irreducible. The temperature can be reduced by radiation, the velocity by charge exchange with the neutral background, and the density by recombination. We have compared the total heat flux (defined as the convected, conducted, and radiated) to the divertor plate at the probe position measured by IR cameras [61] to the convected heat flux inferred from probe measurements. For detached discharges, the convected heat flux to the plate is 30×10^4 W/m^2 or ~80% of the total heat flux. For attached discharges, the convected heat flux is 23×10^4 W/m^2 or less than 30% of the total. These measurements are in agreement with previous work [60] where most of the heat flux to the target plates could be explained by conduction in attached discharges but not by conduction in detached discharges. Therefore, convected heat flux is a dominant heat transport mechanism in detached divertors.

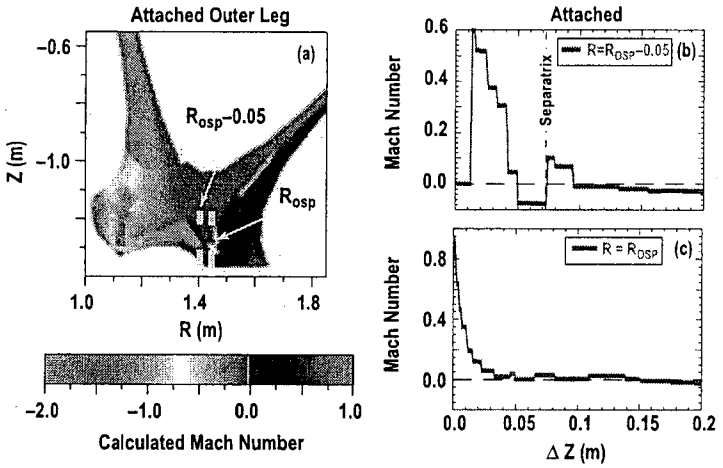

Fig. 3.22: a) Parallel Mach number from an UEDGE simulation of attached plasmas and showing two vertical cuts b) inward cut showing a flow reversal region at the separatrix [equivalent to the data in Fig. 3.21(c)] and c) cut in the SOL showing acceleration toward the divertor plate [equivalent to the data in Fig. 3.20(c) open symbols].

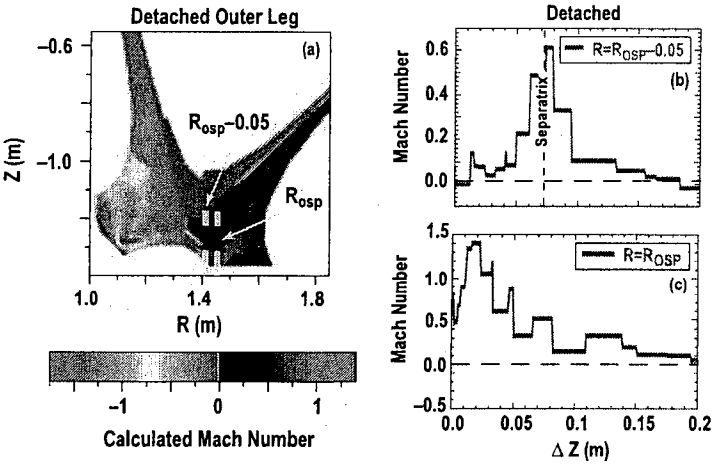

Fig, 3.23: a) Parallel Mach number from an UEDGE simulation of detached plasmas and showing two vertical cuts b) inward cut showing a peak in the Mach number at the separatrix and c) cut in the SOL showing acceleration near mach 1 toward the divertor plate [equivalent to the data in Fig. 3.20(c) solid symbols].

3.6.2 E x B Flows in the Boundary

New measurements of the electric fields, **E** in the DIII–D tokamak divertor region [62] are quantitatively consistent with recent computational modeling [63] establishing that $\mathbf{E}\times\mathbf{B}_T$ circulation is the main cause of changes in divertor plasmas with the direction of the toroidal magnetic field, $\mathbf{B}_T$. Extensive two-dimensional measurements of plasma potential in the DIII–D tokamak divertor region were reported for the first time as shown in Fig. 3.24, featuring an

outward shift of the profiles in reversed $\mathbf{B}_T$. The resulting $\mathbf{E}\times\mathbf{B}_T/B^2$ drift particle flux was

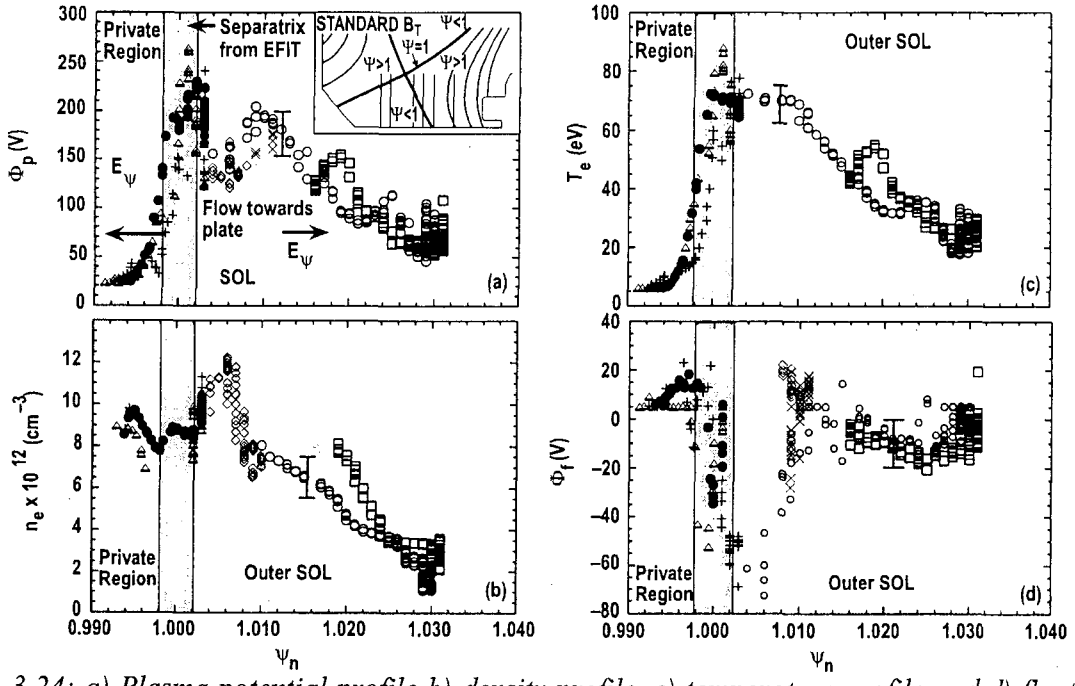

Fig. 3.24: a) Plasma potential profile b) density profile, c) temperature profile and d) floating potential profile showing large gradients at the separatrix between the private region and the outer SOL.

calculated for standard (ion $\nabla\mathbf{B}_T$ drift toward divertor X–point) and reversed $\mathbf{B}_T$ direction and for low (L) and high (H) confinement modes. Perpendicular field strengths of up to $\mathbf{E}$ ~ 5 kV/m were observed at the separatrix between the divertor private region and the scrape-off layer (SOL) as shown in Fig. 3.24(a). The electric field can be understood in terms of pressure gradients along the field lines.

$$-E_{\|} = \nabla_{\|}\Phi = \frac{\nabla_{\|} n_e T_e}{n_e} + 0.71\nabla_{\|} T_e - \frac{J_{\|}}{\sigma_{\|}} \qquad \text{Eq. 8}$$

The $\mathbf{E}\times\mathbf{B}_T$ drift, which reverses with reversal of $\mathbf{B}_T$, creates a poloidal circulation pattern in the divertor that convects 25%–40% of the total ion flow to the divertor target. The particle flux can be roughly written as:

$$\dot{N} \approx 2\pi R n(\Phi_1 - \Phi_2)/B_T \qquad \text{Eq. 9}$$

The resulting circulation, sketched in Fig. 3.25, strongly couples the various regions of the divertor and SOL and fuels the X-point region. The long-observed in-out divertor asymmetry can now be understood in terms of these drifts and also the observation that the asymmetries are reversed when the toroidal field is inverted. When the divertor plasma detaches, the temperature becomes low and uniform over the whole divertor, resulting in a considerable weakening [64] of the ExB drifts. Since the density is very high in these conditions, a weak drift can result in significant fluxes.

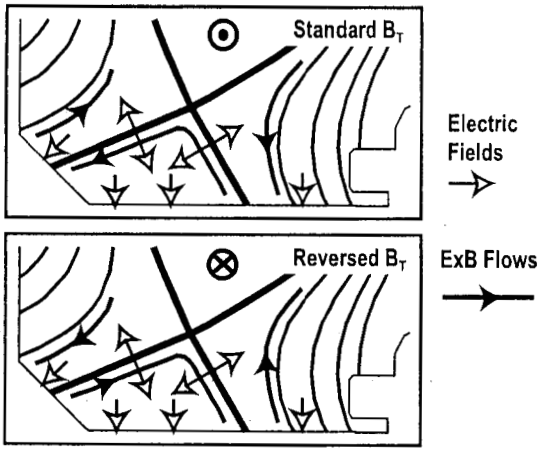

Fig. 3.25: Inferred ExB perpendicular flow patterns for (top) standard Bt direction and (bottom) reversed Bt direction, showing the reversal of flow direction

3.6.3 Puff and Pump Discharges

Improved divertor impurity retention results from "Puff and Pump" discharges have traditionally been interpreted as resulting from enhance induced plasma flow [65] in the SOL of DIII-D. Recent experiments performed with a magnetic geometry suitable for probe access to the SOL, show that the flows in the near SOL are not modified, as seen in Figs. 3.26 and 3.27. Furthermore, there is no observable difference in the plasma flow between upstream gas puff or divertor gas puff (Fig. 3.26). Existing results do not rule out the enhancement of flows in the far SOL, but it is crucial to pursue these experiments to determine the mechanism for impurity entrainment.

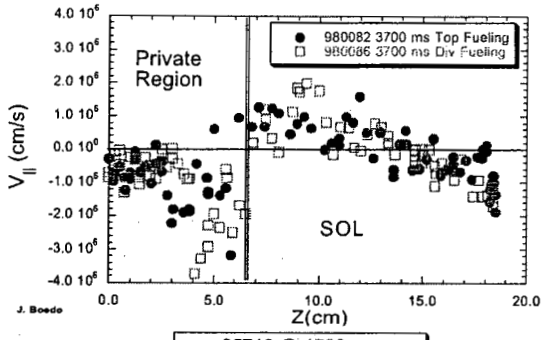

Fig. 3.26: Parallel velocities in the private region and SOL for upstream fueling (solid symbols) and divertor fueling (open symbols) indicating no change

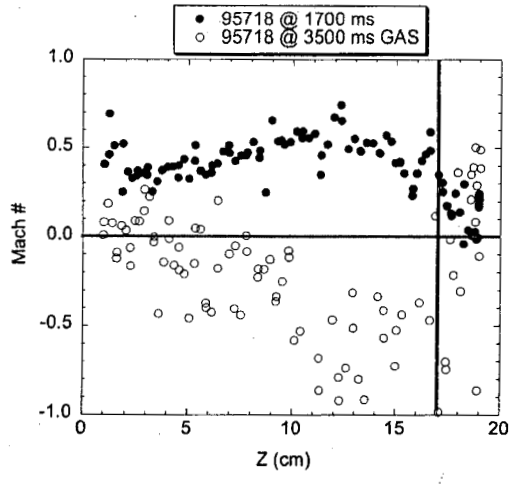

Fig. 3.27: Measured Mach number for a Puff and Pump discharge (open symbols) and a background discharge (solid symbols) showing flow reversal in the private region ($0 \le Z \le 17$ cm) and near SOL ($Z > 17$ cm) for the Puff and Pump discharge. The values in the SOL seem to converge, suggesting no effect on the SOL flow.

3.6.4 Turbulence Suppression during Neon-Seeded Discharges: TEXTOR and DIII-D

Experiments performed in TEXTOR [66] and then in DIII-D [67] show very similar signatures in the behavior of the electrostatic turbulence in the plasma edge. Non-linear gyrokinetic simulation results show that the growth rates and saturated levels of ITG are tremendously reduced, resulting in increased energy and particle confinement. The ITG suppression is achieved chiefly by the modification of the density and temperature profiles in the plasma edge due to the effect of impurity radiation. The linear stabilizing effect of impurities, especially those with highly charged states, on ITG modes, has been considered previously [68,69]. This effect can be most easily seen from the fluid limit growth rate of the ITG mode including impurities and neglecting the parallel ion dynamics. For the small impurity fraction limit, $Zn_z/n_e<1$, where Z is the impurity charge number and n_z the number density of impurity, along with $T_i=T_z$, $L_n=L_{nz}$ and $L_T=L_{tz}$, we obtain the interchange-type growth rate

$$\gamma_{ITG} \approx \sqrt{[1-(Z-1)n_z/n_e]\omega_{*pi}\,\overline{\omega}_{Di}} \qquad \text{Eq. 9}$$

where $1/L_n = \frac{-1}{n}\frac{dn}{dr}$, $\omega_{*pi} = \frac{k_\theta c}{eBn_i}\frac{dp_i}{dr}$ is the ion pressure gradient drift frequency, k_θ is the poloidal wave number, $\overline{\omega}_{Di} = \frac{L_n}{R}\omega_{*i}\frac{\langle v_\perp^2 + v_\parallel^2/2\rangle}{v_{thi}^2}$ is the energy-averaged ion toroidal drift frequency, $\rho_i = c\sqrt{m_iT_i}/eB$ is the ion gyroradius, and $v_{thi} = \sqrt{T_i/m_i}$. A Boltzmann response for the electrons can be used if one assumes that the phase velocity of the perturbation satisfies $v_{the} > \omega/k_\parallel > v_{thi}$. In the small impurity fraction limit, the real frequency of the mode is $\omega_{real} \sim \omega_{Di} > \omega_{Dz}$. Physical insight can be gained from Eq. 9 by noting that impurities and their radiation can reduce the driving term of the ITG mode by: 1) modifying the pressure or density gradient (and thereby ω_{*pi} or the scale length L_n), 2) diluting the main ion species and 3) reducing the growth rate below the $\vec{E}\times\vec{B}$ shearing rate.

Impurity seeding experiments have been performed in DIII-D by injecting trace amounts of neon, argon and krypton. The energy confinement increases after the injection as shown in Fig. 3.28, but the improvement over the background conditions is inversely dependent in the Z of the injected impurity (Fig. 3.28). The turbulent particle transport in the edge is reduced by a factor of 7-10 for neon over deuterium as shown in Fig. 3.29 but higher Z gases (argon and krypton) induce a lesser effect, in agreement with the global confinement time behavior.

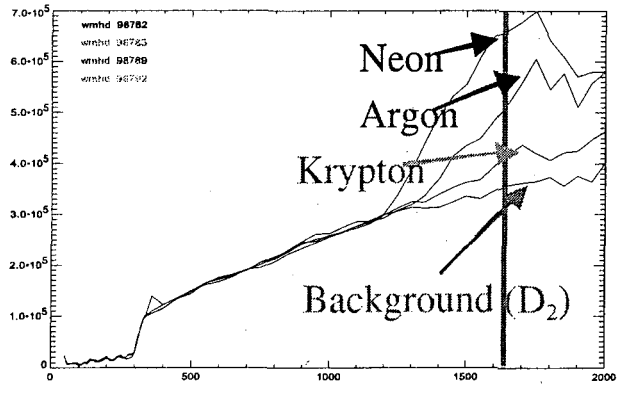

Fig. 3.28: Time evolution of the plasma stored energy (J) for seeding with 3 impurities, neon, argon and krypton. The probe is inserted at 1600 ms. The largest increase is obtained for neon and progressive lower as Z increases.

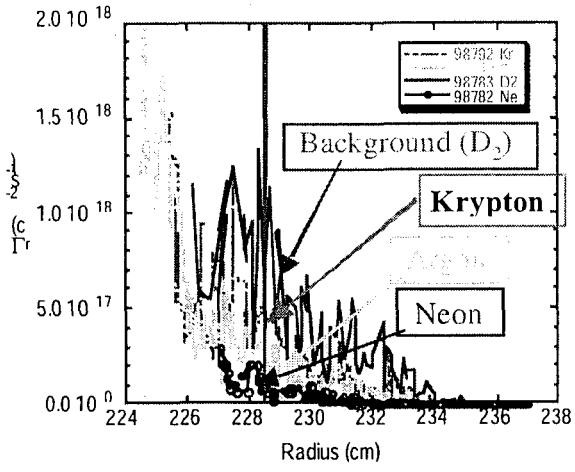

Fig. 3.29: Turbulent particle transport profiles at the edge of DIII-D for seeding with various gases. The suppression of turbulence is greatest for neon and progressively lower for higher Z impurity.

A concomitant increase of particle and energy confinement times as the impurity concentration increases during impurity seeding experiments in TEXTOR (Fig. 3.30) suggests that there is a common, global phenomenum at play. The particle confinement time increase is consistent with first measurements of turbulence in the edge of the TEXTOR-94 device showing that the radial particle transport is reduced by a factor of 4-7 [Fig. 3.31(a)] due to the quenching of both density [Fig. 3.31(b)] and poloidal electric field [Fig. 3.31(d)] turbulence levels. Non-linear gyrokinetic particle-in-cell simulations of these discharges show impurity-induced suppression of the electrostatic fluctuations associated with the Ion Temperature Gradient-driven (ITG) mode. The simulations use experimental profiles to determine that the growth rate of the ITG modes is reduced [Fig. 3.32(a)] and that the reduction is significant over most of the outer 60% of the discharge [Fig. 3.32(b)], including the edge where the probe measurements are performed. The results suggest that the suppression of ITG modes is the underlying mechanism for confinement improvement.

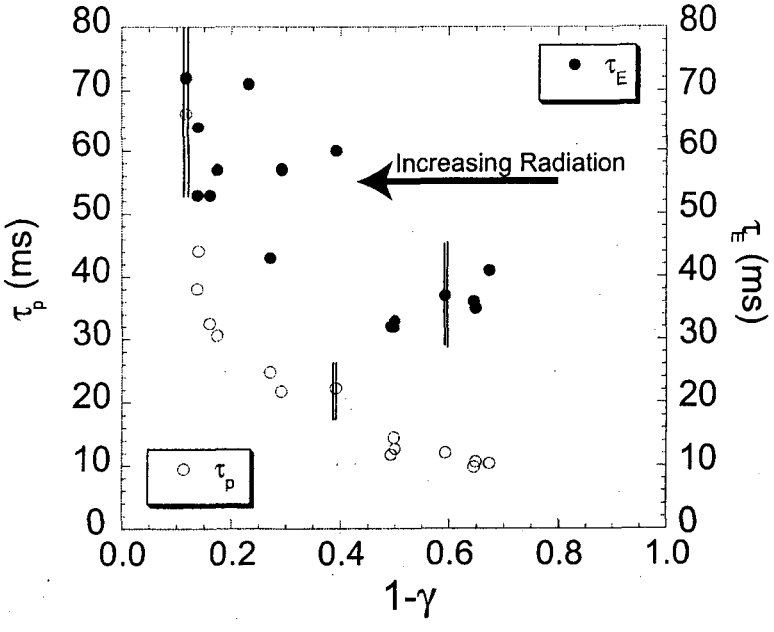

Fig. 3.30: Particle and energy confinement times increase concomitantly with radiation levels, suggesting a common underlying mechanism

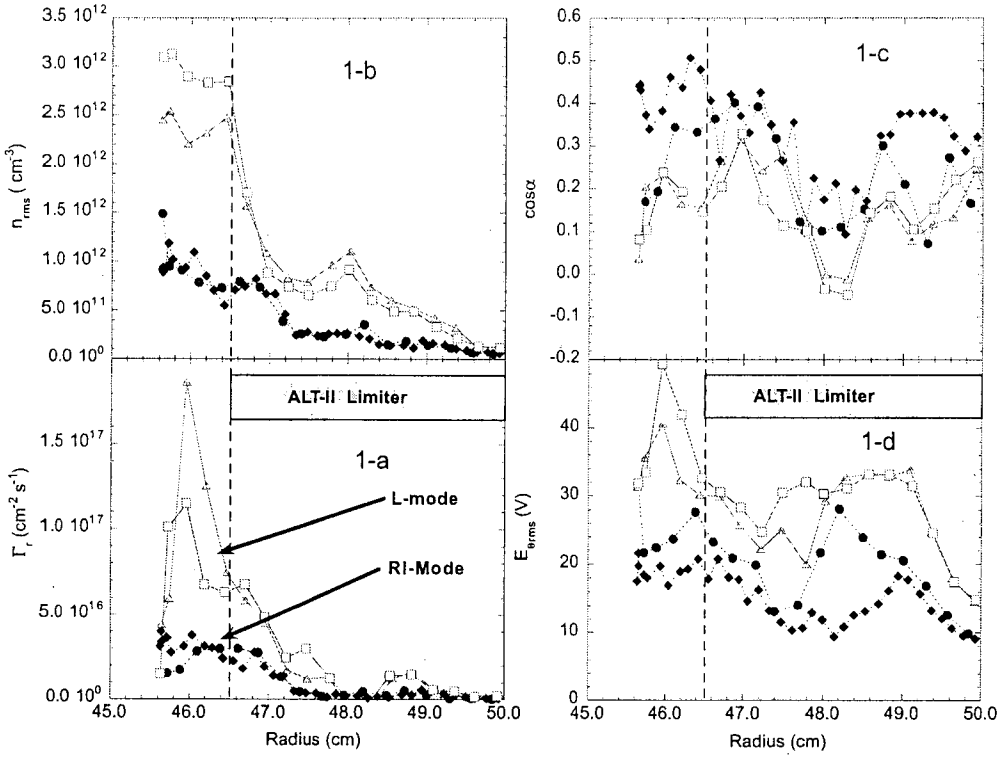

Fig. 3.31: Profiles of a) turbulent particle flux, b) density fluctuations, c) cross-phase and d) poloidal electric field fluctuations during L-mode (open symbols) and RI-mode (solid symbols) discharges.

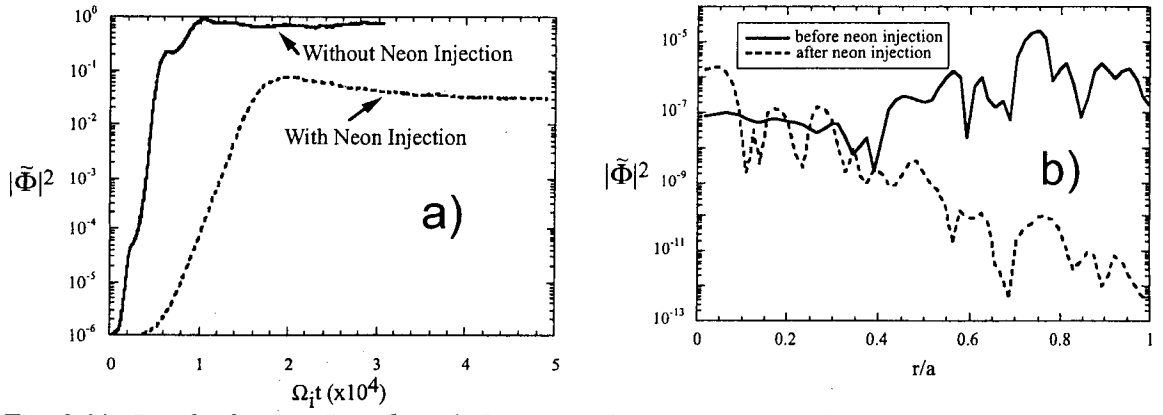

Fig. 3.32: Results from ITG mode turbulence simulations for RI Mode, showing: a) Evolution of the volume-averaged turbulence with time and b) Radial profiles of potential fluctuation levels averaged over a correlation time.

3.6.5 Intermittent convective radial transport in DIII-D:

The balance between parallel and perpendicular transport in the SOL generally results in SOL profiles that are near exponential [70,71] with short (1–3 cm) decay lengths near the separatrix. However, evidence that the SOL profiles can be very wide and flat abounds [72-74.], suggesting

that perpendicular transport in these conditions is much larger than expected, and enhancing the plasma-wall contact beyond what would be expected from exponential profiles.

A candidate for the additional edge/SOL transport, intermittency in the fluctuations corresponding to events above the standard deviation, has been extensively documented in linear devices, [75,76]., stellarators, [77] and tokamaks [78-80] and its statistical properties examined [81,82] via the probability distribution function (PDF) [83]. The fluctuations depart from a Gaussian distribution, featuring skewness and kurtosis due to the intermittent events. Furthermore, it has been proven that the statistical properties of the fluctuations are near-Gaussian in the shear layer while deviating from Gaussian into the SOL of tokamaks (Joint European Torus, JET), and stellarators (Advanced Toroidal Facility, ATF, Weldestein 7 Advanced Stellarator W7-AS). The intermittency has been analyzed using conditional averaging tools in both linear devices [75,76] and tokamaks [84-89] with the result that coherent structures propagating radially are responsible for much of the radial transport. Comparative work at the devices TJ-I and TJ-IU [81] concluded that intermittency bears a substantial part of the transport and most importantly, that the various properties of the intermittency (power spectra, PDF moments, etc.) are self-similar in tokamaks and torsatrons. Work in the JET tokamak [90] focused on the power spectra of the fluctuations, demonstrating that its decay as 1/f was localized in the spectral region where intermittent transport is dominant and interpreting the result as an indication of closeness to instability thresholds. On the other hand, very recent work on the Alcator-C device [91] has mostly focused on transport analysis of the SOL and demonstrated the need of very large diffusion coefficients if convection is not considered. Additionally, there is an extensive body of work imaging the edge of various devices with fast cameras [92,93] which show that moving plasma filaments exist in the edge/SOL. However, although the universality of intermittency in the SOL and the concomitant fast convective transport in confined plasmas has been established, limited work on the dynamical characteristics, origin, or scaling with plasma parameters has been done.

At DIII-D, we have focused recently on the dynamics and scaling of the intermittent boundary transport. We find that intermittent plasma objects (IPOs) featuring higher pressure than the surrounding plasma, and responsible for ~50% of the $\boldsymbol{E} \times \boldsymbol{B_T}$ radial transport, are observed in the scrape-off layer (SOL) and edge of the DIII–D tokamak [84]. The skewness (i.e. asymmetry of fluctuations from the average) of intermittent density fluctuations from the mid-plane probe and from Beam Emission Spectroscopy (Fig. 3.33) suggest IPO formation at or near the last closed flux surface (LCFS) and the existence of hole-IPO pairs due to the change is sign of the skewness across the LCFS [94]. BOUT and other fluid codes can reproduce the intermittent behavior; in particular, BOUT can reproduce the skewness profiles from the experiment [95].

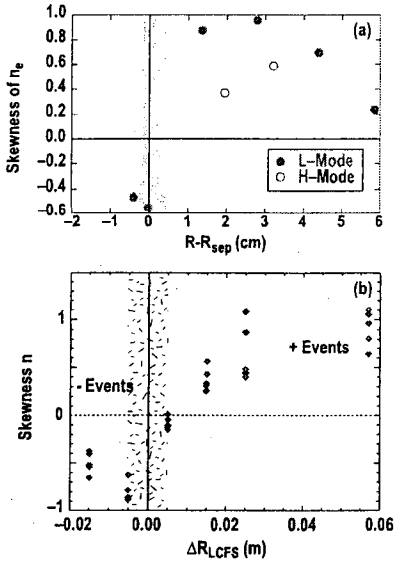

Fig. 3.33. Radial profile of the skewness of density fluctuations in L-mode (red) and H-mode (open blue circles) across the LCFS. The data are from BES (top) and mid-plane probe (bottom).

Conditional averaging was used to characterize typical events in fluctuations and fluxes, and reveals that there are "holes" coexisting with spikes in the vicinity of the separatrix (Fig. 3.34) [95], consistent with the interpretation of the radial profile of the skewness measurements Furthermore, the holes move inward, due to being negatively polarized, as seen in Fig. 3.34. Recent calculations by Sarazan and Ghendrih [96] suggest that interchange instability is responsible for the "hole-hill" phenomena as the hot LCFS plasma and the cold SOL plasma interpenetrate each other,in agreement with observation.

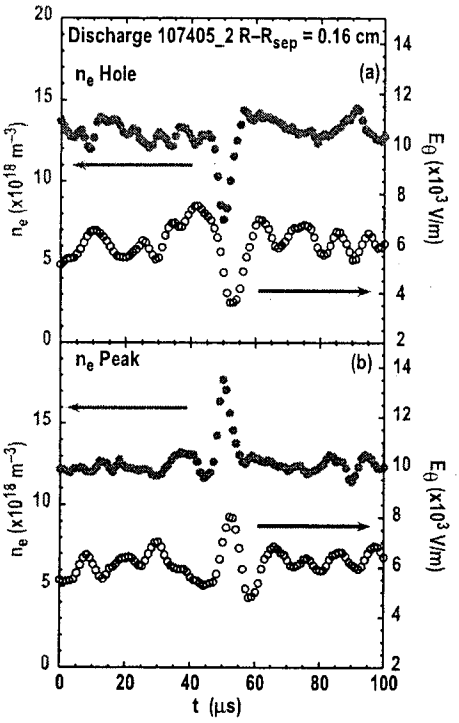

Fig. 3.34. "Average" (top) hole and (bot) IPO events obtained from conditional sampling of fluctuating probe signals. The density (red) shows clear "hole" and "peak" structure, while E_θ (blue) has opposite sign for the holes and peaks, corresponding to radially inward $E_\theta \times B_T$ motion for holes and radially outward motion for peaks.

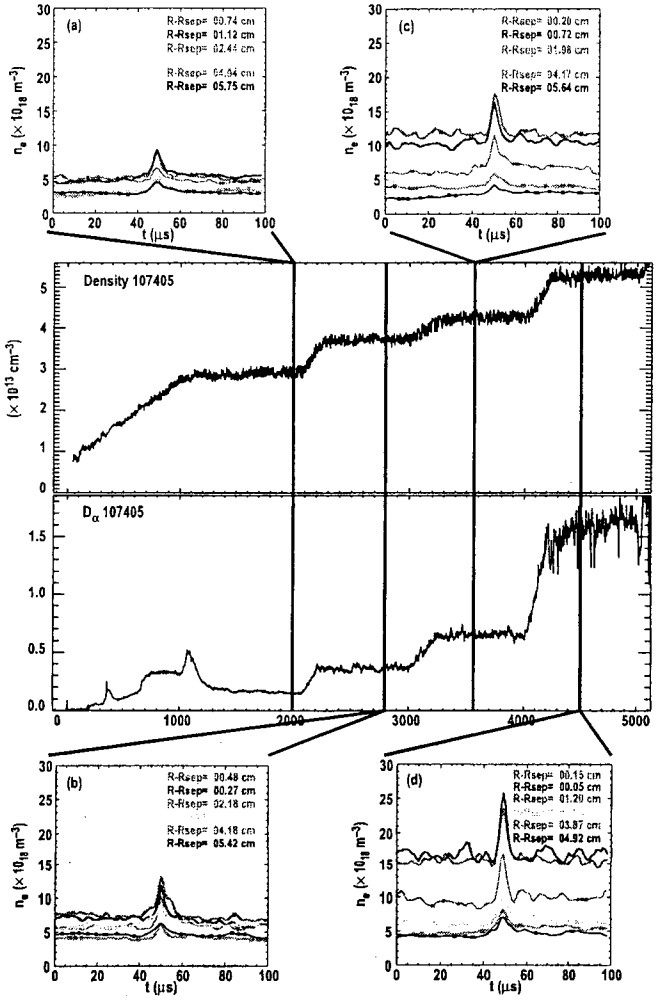

Fig. 3.35. Structure of density IPO in the SOL of DIII-D for 4 different discharge densities. Also shown for comparison is the variation in D_α emission.

The particle content of the IPOs at the LCFS is linearly dependent on the discharge density as seen in Fig. 3.35, consistent with observations that the particle flux increases with density [94]. An interesting point is that the normalized IPO density (i.e. IPO density divided by the local averaged density), it is fairly insensitive to discharge density variations. Another important result shown in Fig. 3.36, is that the IPOs quickly thermalize with the background plasma within a few cm of the LCFS [95].

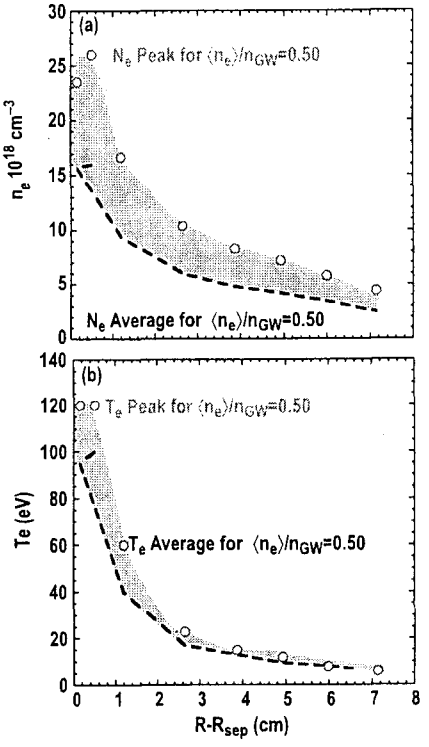

Fig. 3.36 Radial profiles of the equillibrium density (top) and T_e (bot) and the range of IPO amplitudes (green shading) for a line average density of 0.5 n_{GW}. Although the relative density perturbation is fairly constant across the SOL, the T_e perturbation decays to the equilibrium level within a few centimeters of the LCFS.

Because the spikes in plasma density correlate with those in the poloidal electric field (Fig. 3.34), the IPOs are intermittent transport events carrying both particles and heat. The intermittence has qualitatively similar character in L-mode and ELM-free H-mode. However, in absolute terms transport rates due to intermittence are much higher in L-mode due to the higher density of the IPOs in L-mode. Low-amplitude ELMs observed in high-density H-mode produce in the SOL periods with cross-field transport enhanced to L-mode levels and featuring intermittent events similar to those in L-mode. Figure 3.37 shows the contribution of the intermittent events to the net particle and heat fluxes as a function of the relative (normalized to the mean flux) amplitude of events. Each point represents the integral fraction of the total flux carried by all events with the relative amplitude above the corresponding x-axis value. Thus, events with amplitude above 10 times the mean flux level are responsible for about 60–65% of the net particle and heat transport in L-mode and for about 30% of the net transport in H-mode.

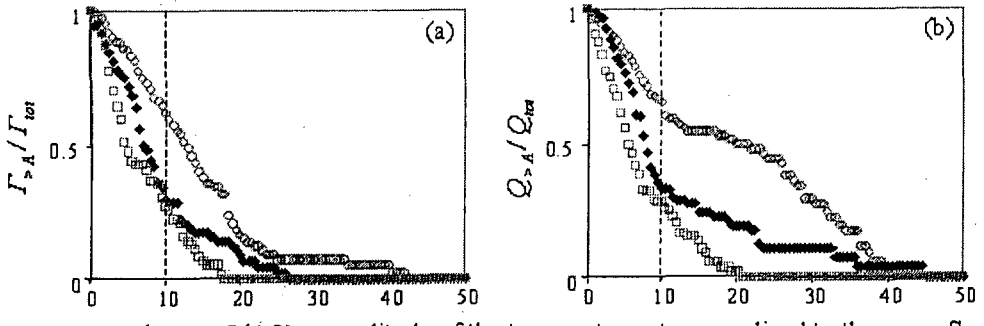

Fig. 3.37: Integral fraction of the total particle (a) and heat (b) flux carried by transport events with relative (normalized to the mean flux) amplitude above the x-axis value in L-mode (open circles), ELM-free H-mode (solid diamonds) and during an ELM (open squares)

Experimental evidence obtained so far is consistent with a model involving plasma filaments or IPOs with density higher than that of the background plasma propagating outwards due to $\boldsymbol{E} \times \boldsymbol{B}$ drift. Accepting this model as a working hypothesis, we can estimate an average radial propagation speed and an average size of the IPOs from the spikes in the probe signals. Just outside the separatrix the IPOs are typically 2–4 cm in transverse size and move in both poloidal and radial directions with velocities of about $2–5 \times 10^3$ m/s. These values agree with the results from the Beam Emission Spectroscopy (BES) diagnostic. As the IPOs move towards the wall, they gradually shrink in size to about 0.5 cm and slow down to about 500 m/s [85]. This is consistent with Fig. 3.36 and with the observed fast decay of the n_e and T_e profiles.

Recent non-linear simulations performed with an imposed driving flux have shown that the turbulent transport is dominated by long-range transport events or avalanches [96]. The simulations predict intermittent dynamics of the events and statistical properties of the turbulence similar to those observed in our experiments. Work on detailed statistical analysis of the intermittence and comparison with modeling is underway.

3.6.6 ELM dynamics in DIII-D

High performance tokamak discharges operate in ELMing H-mode in order to combine high energy confinement with adequate particle exhaust. However, the ELM instability carries a considerable amount of particles and heat from the pedestal region into the SOL towards the divertor region and other plasma facing components (PFCs), limiting their lifetime and causing the release of impurities into the plasma. Additionally, ELMs can have deleterious effects on confinement by suddenly (< 1 ms) collapsing the pedestal region and causing an inward cold pulse. Simple ELM-induced ablation thresholds for reactor PFCs scale as $Q/t^{1/2}$, where Q is the deposited ELM energy density and t is the ELM duration. It would be beneficial to reduce the ELM deposited energy and extend the duration. Therefore, a considerable amount of effort has been invested by the fusion community to study ELMs and to produce scaling laws [97] that allow extrapolation to the next step devices, such as ITER. Recent results [98] indicate that the initial ELM energy scaling laws, showing a linear dependence with pedestal pressure, can be circumvented if plasma operation is conducted at high density. As an example of the present situation, if the existing scaling laws for Type I ELMs are applied to ITER discharges, it is found that the divertor lifetime may be exceeded in a single discharge. Therefore a more fundamental understanding of ELMs is needed in order to develop techniques for controlling their properties.

A number of theoretical studies of ELMs have noted that the sharp pressure gradients, and consequent large bootstrap currents in the pedestal region can destabilize MHD peeling (i.e. edge localized external kink) and ballooning modes over a wide range of toroidal mode numbers (n). Recent studies [99-101] have emphasized the complex dual role the bootstrap current plays in the stability physics, on one hand driving peeling modes, while on the other lowering edge shear and opening second stability access to high-n ballooning modes. Field line bending stabilizes long wavelength modes, while short wavelengths are stabilized by a combination of second stability and FLR/diamagnetic effects, shifting the limiting modes to intermediate wavelengths (typically n~4-40). These dominant modes are referred to here as coupled peeling-ballooning modes, and are driven by both parallel current (J_{ped}) and the pressure gradient (∇p_{ped}) [100,101]. These intermediate-n peeling-ballooning modes impose constraints on the pedestal height, which are functions of the pedestal width, plasma shape, collisionality, safety factor and other equilibrium details. Studies of the nonlinear evolution of these peeling-ballooning modes are in their infancy; however, some expected general characteristics of a peeling-ballooning mode driven ELM crash can be surmised from linear calculations of mode structures along with insight from preliminary nonlinear studies.

A characteristic linear mode structure for an n=10 peeling-ballooning mode in a DIII-D plasma, calculated using the ELITE code [101,102], is shown in Fig. 3.38. The mode has maximum amplitude on the outer mid-plane, and has very small amplitude on the high field side of the plasma. The mode structure follows field lines, and thus consists of a series of filaments, with a length ~qR along the field line, a poloidal wavenumber of roughly nq, and a radial extent somewhat larger than the pedestal width (noting that the local field line curvature should replace q for a more accurate estimate). Preliminary nonlinear studies suggest that during the ELM, a number of these filaments will grow in the pedestal region and travel across the separatrix into the scrape off layer, carrying particles and heat with them. However, the existing theoretical understanding does not predict the non-linear phase of the ELM and still has to include various effects such as toroidal and poloidal rotation and finite resistivity [101]. Therefore, measurements are needed to provide theorists with detailed information on ELM genesis, structure and propagation that can be used to improve the models.

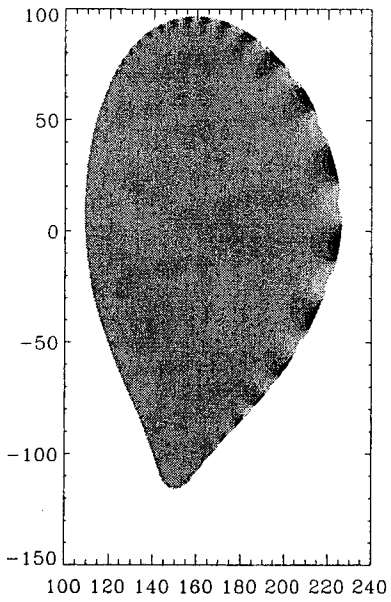

Fig. 3.38: Poloidally asymmetric linear mode structure for an n=10 peeling-ballooning mode in DIII-D, calculated using the ELITE code.

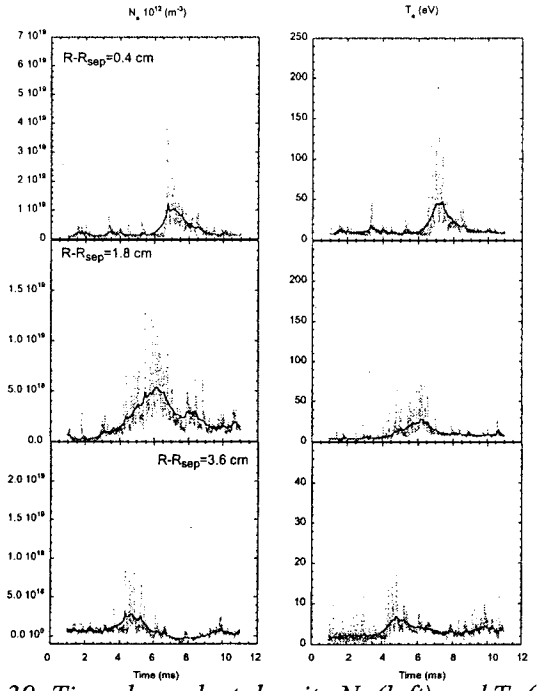

Fig. 3.39. Time dependent density N_e (left) and T_e (right) at 3 radii in the SOL (0.4 cm, 1.8 cm, and 3.6 cm outside the LCFS from top to bottom) showing chains of fast bursts (red) on a slower rise and decay (blue lines).

High temporal and spatial resolution measurements in the boundary of the DIII-D tokamak [103] show that Edge Localized Modes (ELMs) are produced in the low field side, are poloidally localized and are composed of fast bursts of hot, dense plasma on a background of less dense, colder plasma (~5×10^{18} m^{-3}, 50 eV) created by the bursts themselves (Fig. 3.39) The ELMs travel radially in the scrape off layer (SOL), starting at the separatrix at ~450 m/s, and slowing down to ~150 m/s near the wall, convecting particles and energy to the SOL and walls. The temperature and density in the ELM are initially very similar to those at mid-pedestal but decay with radius in the SOL. The temperature decay length (~1.5 cm) is much shorter than the density decay length, which is very dependent on discharge (and SOL) density (Fig. 3.40). The local particle and energy flux at the wall during the bursts can reach ~1-2×10^{21} m^{-2} s^{-1} and 20-30 kW/m^2

respectively. The ELM plasma density and temperature increase linearly with density up to a Greenwald fraction of ~0.6, after which they drop [98,103,104]

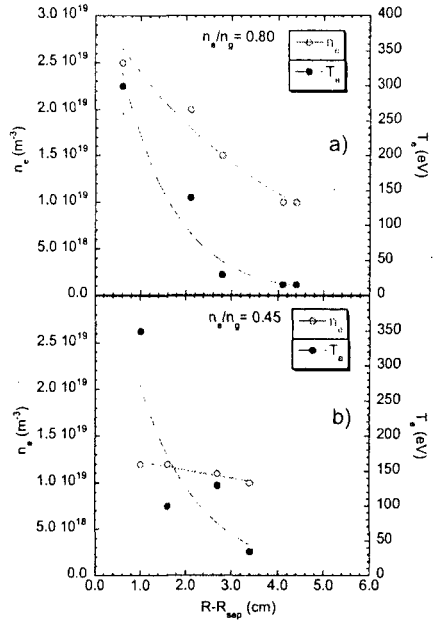

Fig. 3.40. Radial profile of the n_e (red) and T_e (blue) perturbations associated with ELMs at n_e/n_{GW} = 0.80 (top) and 0.45 (bot). The ELM T_e perturbation decays more rapidly in the SOL than the density perturbation.

From the previous discussion, it is clear that much information is missing from our picture of ELMs, the nonlinear ELM phase and its dynamics in the edge/SOL. An imaging diagnostic was developed by using a fast, intensified CID camera with a tangential view of the DIII-D divertor to image emission from deuterium and carbon in the visible part of the spectrum [105]. From the tangentially integrated data, a 2D profile of the emissivity can be reconstructed, as shown in Fig. 3.41 The sequence of images shown indicate that the ELM causes reattachment of the originally detached inner divertor leg (carbon emissivity shifts from the X-point to the divertor floor) which then evolves back into detachment after the ELM is absorbed into the divertor. UCSD participated in this diagnostic development and physics task by designing a triggering circuit that uses input from fast diagnostics (such as fast photodiode arrays) to produce an output for the camera trigger to synchronize the camera to the ELMs [106].

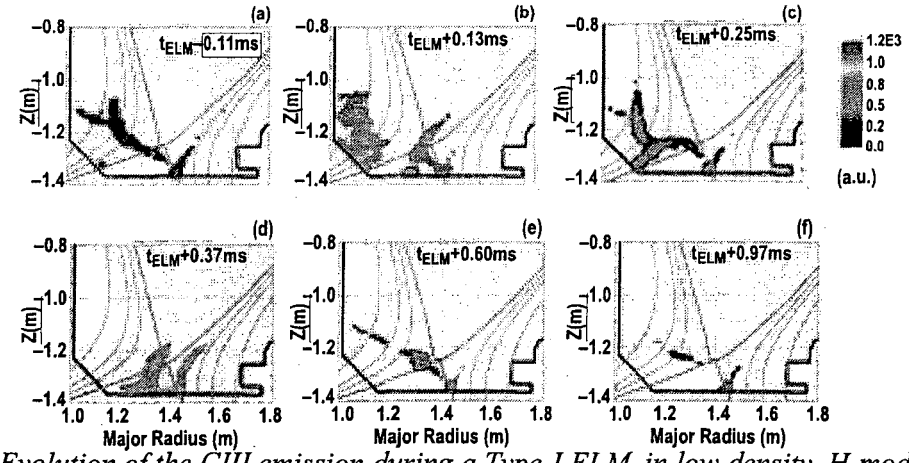

Fig. 3.41. Evolution of the CIII emission during a Type-I ELM. in low density, H-mode plasmas. The time of the ELM (t_{ELM}) is defined as that of the rise in the mid-plane photodiode array signal.

3.6.7 Comparison of Fluctuation Measurements with Numerical Simulations (BOUT, BAL Codes)

Fluctuation, flow, and turbulent transport measurements from the reciprocating probe arrays have been used for extensive benchmarking of the BOUT 3-D boundary turbulence code in realistic divertor geometr [107] and the BAL MHD shooting code with ballooning formalism [108]. These efforts have produced an ideal tool for investigating a range of plasma boundary physics issues, including L to H transitions [109], ion ∇B drift effects, and turbulent transport scaling [110-112]. Key results include the identification of the X-point mode as the dominant boundary fluctuation mode. This mode is a modification of curvature driven modes that occurs in the realistic, high magnetic shear geometry of a shaped divertor tokamak. Preliminary modeling of the ion ∇B drift effect on the H-mode power threshold suggests that this mode causes the higher power threshold since it is strongly damped when boundary poloidal flows are from the midplane to the X-point (for the ion ∇B drift toward the X-point) and not when these flows are from the midplane away from the X-point (ion ∇B drift away from the X-point).

3.7 Pedestal Physics

3.7.1 C-Mod similarity experiments i n DIII-D

Because the H-mode pedestal T_e plays an important role in setting the overall level of core performance, it is important to determine the physics that sets this pedestal "height." If ∇T_e is set by MHD stability limits, then the T_e pedestal height should depend on the width of the H-mode pedestal. Consequently, understanding the physics that governs the width of the H-mode pedestal is a critical need for the tokamak community. It has been postulated that the H-mode pedestal width might be governed by either "plasma physics" effects (transport considerations) [113] or by "atomic physics" (that is, by neutral penetration lengths) [114]. One approach to separate these two mechanisms is to study the similarity of the H-mode pedestal in two different tokamaks in plasmas with matched shape (elongation κ, triangularity δ, and inverse aspect ratio ε) for similar MHD stability conditions (Fig. 3.42), and matched *local* edge dimensionless parameters β, ρ*, collisionality ν* and safety factor q_{95} at the top of the pedestal:

Target dimensionless parameters at the top of the pedestal:

$$\nu^* \sim \frac{an_e}{T_e^2} \approx 2 \qquad \rho^* \sim \frac{T_e^{1/2}}{B_T a} \approx 5\times10^{-3}$$

$$q \sim \frac{aB_T}{I_p} \approx 4.5 \qquad \beta \sim \frac{T_e n_e}{B_T^2} \approx 5\times10^{-3}$$

$$\varepsilon = \frac{a}{R} \approx 0.3$$

Parameter	C-Mod	DIII-D	Scaling
R	0.7 m	1.7 m	~a
a	0.2 m	0.48 m	~a
ε	0.28	0.28	
B_T	5.4 T	1.8 T	$\sim a^{-5/4}$
I_p	1 MA	0.73 MA	$\sim a^{-1/4}$
n_e	3e20 m^{-3}	5e19 m^{-3}	$\sim a^{-2}$
T_e	600 eV	390 eV	$\sim a^{-1/2}$

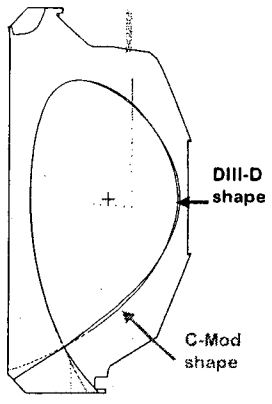

Fig. 3.42. Matched DIII-D (black) and C-Mod (magenta) shapes used in the pedestal dimensionless scaling experiment..

DIII-D discharges with the appropriate shape and engineering parameters to match C-Mod were obtained. These discharges provided a good match in pedestal profiles for type-I ELM-free EDA H-mode conditions in C-Mod at a power through the separatrix P_{sep} in DIII-D ≈ 500 kW, close to the expected scaling:

$$P_{sep}^{D3D} \sim P_{sep}^{CMod}\left(\frac{a^{CMod}}{a^{D3D}}\right)^{0.75}$$

$$\approx 1.15e6\left(\frac{.22}{.56}\right)^{0.75} \approx 570kW$$

Because the DIII-D dimensionless scaling match to EDA H-mode was not steady-state (Fig. 3.43), we were able to obtain dimensionally similar pedestals for both EDA and ELMy H-mode discharges in Alcator C-Mod (Fig. 3.44). For discharges with dimensionally similar parameters at top of the pedestal, the same pedestal width in flux coordinates was obtained on C-Mod and DIII-D, implying that pedestal width scales with machine size.

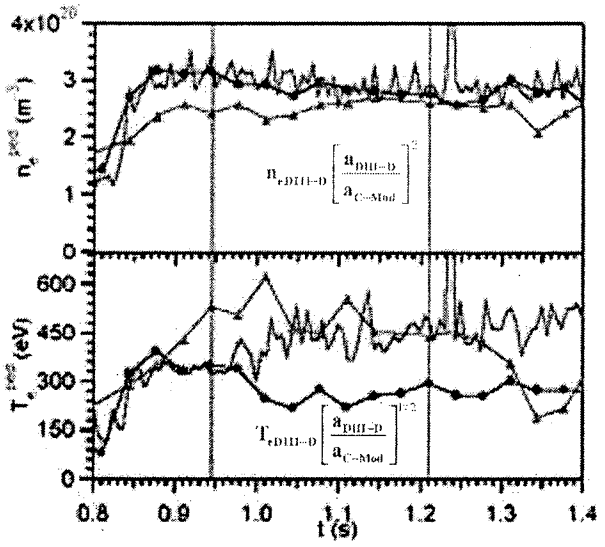

Fig. 3.43. Comparison of the pedestal n_e (top) and T_e (bot) for an EDA H-mode (blue circles) and an ELMy high density H-mode (green triangles) in C-mod and a DIII-D discharge that matches the dimensionally scaled pedestal conditions of the EDA H-mode at 0.945 s (blue line) and the ELMy H-mode at 1.21 s (green line).

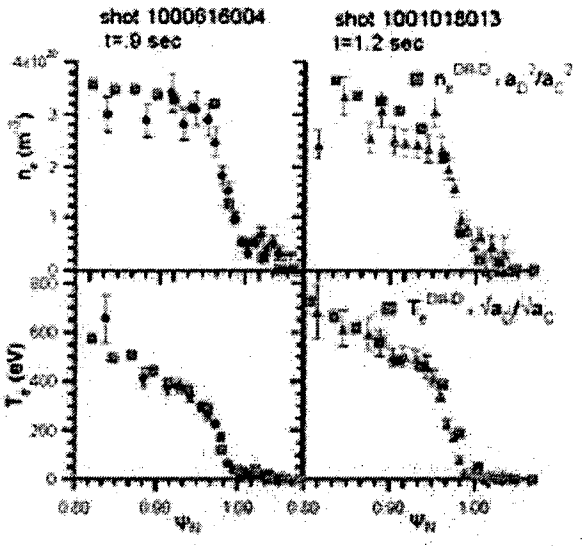

Fig. 3.44. Demonstration of the dimensional similarity between the C-Mod and DIII-D H-mode pedestal n_e (top) and T_e (bot) profiles for the discharges in Fig. 3.43. C-mod data correspond to EDA H-mode (left: blue circles), and ELMy H-mode (right; green triangles). The DIII-D data (red squares) is dimensionally scaled to the C-Mod values.

These dimensionally similar pedestal matches also displayed similar MHD edge stability behavior, as shown in Fig. 3.45. The DIII-D match the Type-I ELM-free EDA H-mode .was also ELM-free, although it did not display the increase in overall recycling from which EDA H-mode gets its name. Like EDA H-mode, however, the DIII-D ELM-free discharge displayed a strong

quasi-coherent oscillation in the H-mode pedestal region (Fig: 3.45) which drives large amounts of local particle and heat transport, similar to the QC mode in C-Mod (Fig. 3.46). Both the mode frequency and poloidal wavenumber k_θ scale from the C-Mod values, suggesting that this is indeed the same mode as the QC mode in C-Mod.

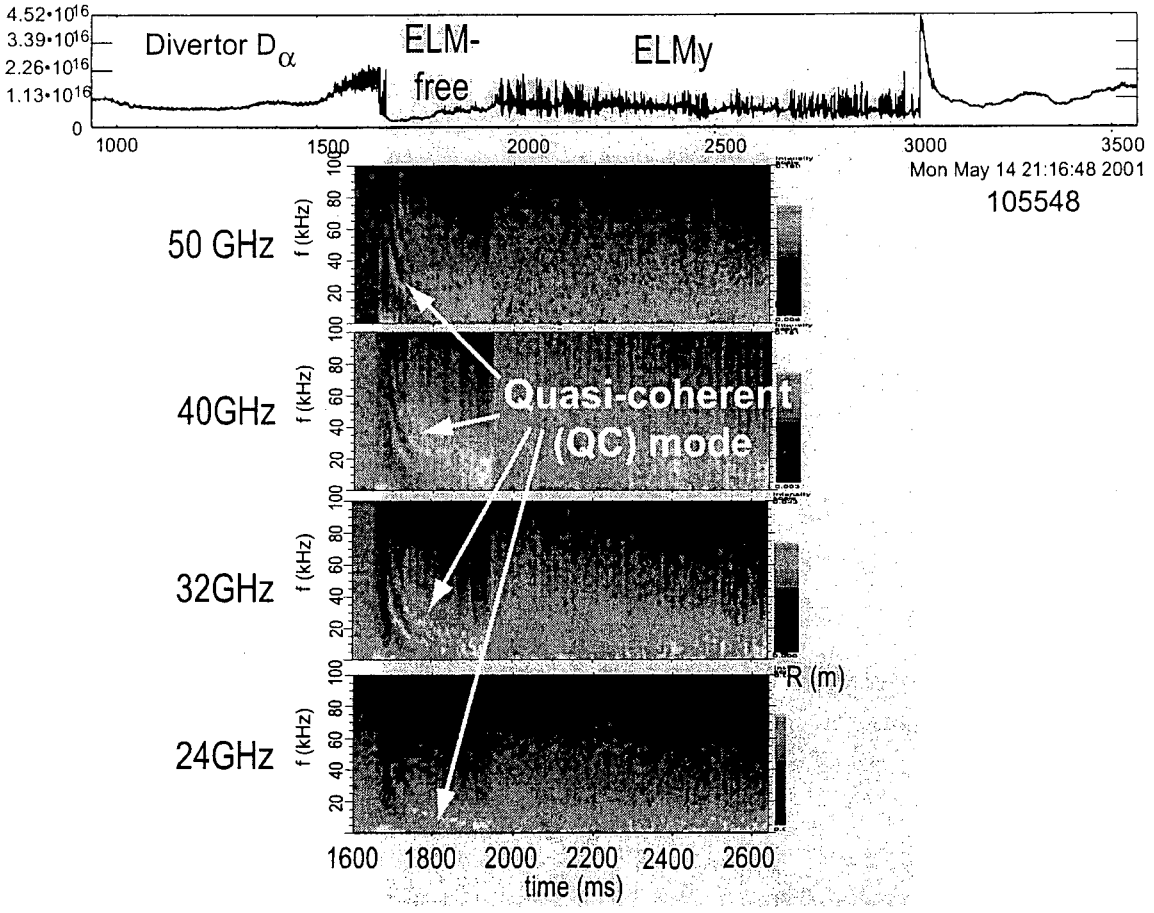

Fig. 3.45. Divertor recycling light D_α and color contour plots of the ñ autopower spectra measured by four fixed frequencies of homodyne reflectometry in the pedestal. During the ELM-free phase, the ñ power spectrum is dominated by a QC mode that shows some near-harmonic components on some channels. Once the rapid, small ELMs start, the ñ spectra become broadband for all four channels.

Although the DIII-D similarity discharges display ELM and fluctuation behavior similar to EDA H-modes in C-Mod, the QC mode doesn't appear to provide sufficient levels of cross-field transport to prevent the central density from peaking and the impurities to subsequent accumulation in the core (Fig. 3.47). Since the QC mode is confirmed to drive large levels of transport locally, this results suggests that the conclusion that the QC mode is responsible in C-Mod EDA H-modes for maintaining steady-state H-mode operation without ELMs may not be correct. Nevertheless. The validity of the dimensionless scaling approach to the pedestal is well established by these experiments: for discharges with similar MHD stability properties (shaping), dimensionally correct edge pedestal profiles were obtained at the appropriate dimensionally scaled power through the separatrix. Further, these discharges display identical ELM behavior to the dimensionally scaled C-Mod discharges, and feature a strong quasi-coherent oscillation in the pedestal with frequency and wavenumber consistent with scaling expectations. This mode drives

significant local transport, as seen in C-Mod, but apparently not enough for maintaining steady-state in DIII-D, where the discharges evolve into dimensionally scaled matches to high density ELMy H-modes in C-Mod.

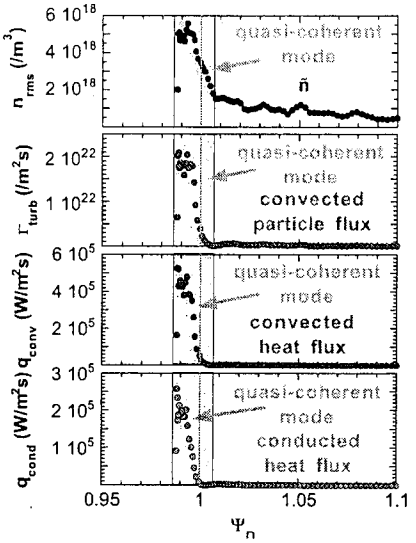

Fig. 3.46. Radial profiles of the rms amplitude ñ of density fluctuations (top), turbulent convected particle flux Γ_{turb} (second from top), and turbulent convected q_{conv} (third from top) and conducted q_{cond} (bot) heat fluxes. All four signals are dominated by the narrow peak of the QC mode, indicated by the tan shaded region.

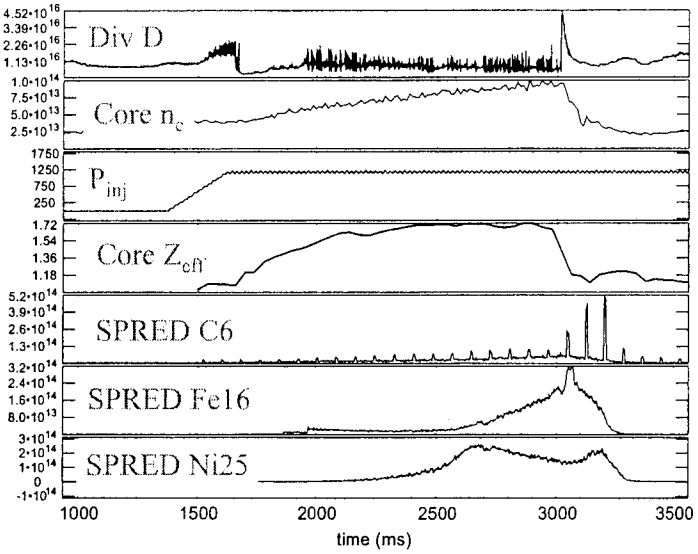

Fig. 3.47. Time dependence of core density n_e, Z_{eff}, and selected impurity lines, showing the peaking in the density profile and concomittent inward pinch of impurities. The transport associated with the QC mode doesn't appear sufficient to prevent this density peaking and impurity pinch as it is in C-Mod

3.7.2 Coherent, quasi-coherent, and harmonic modes in the pedestal

The appearance of a quasi-coherent mode localized to the H-mode pedestal during ELM-free operation is not new to C-Mod similarity discharges. In the early 90s, researchers at DIII-D observed similar modes in the ELM-free phases of high density H-modes following very slow L-H transitions [115]. In these discharges, the QC mode was also observed to drive significant particle transport locally. This type of non-diffusive transport is often seen in high-density H-modes with prolonged ELM-free periods, where the transport near the separatrix is dominated by coherent modes driving particle and/or heat fluxes exceeding L-mode levels (Fig. 3.48). These modes may play an important role by providing particle and/or heat exhaust between ELMs, and might provide a means to circumvent large ELMs in steady-state H-mode if the associated transport can be enhanced. Fig. 3.49 shows relative (normalized to RMS fluctuation levels) modulation of the electron density, electron temperature and poloidal electric field by coherent modes in two H-mode discharges. The figures were generated by averaging over about 20 periods of the fluctuation in such a way that the relative phasing of the signals was preserved. In the first case [Fig. 3.49 (a)] all three signals are sufficiently in phase to cause radial transport of both particles and heat exceeding those in L-mode at comparable conditions. In the second case [Fig. 3.49(b)] the electron temperature and poloidal electric field change roughly in phase

while the density is about 90 degrees out of phase. Therefore, in this case the particle flux and associated convective heat flux are low, while the conductive heat flux (due to correlation between the electron temperature and poloidal electric field fluctuations) is high. Despite the high level of transport driven by the modes confinement stays good, implying that the fluxes are either poloidally non-uniform or not time-stationary. On the other hand, it is possible that the modes still provide enough particle and/or heat exhaust at the plasma edge to prevent the edge gradients from reaching critical values and driving ELMs.

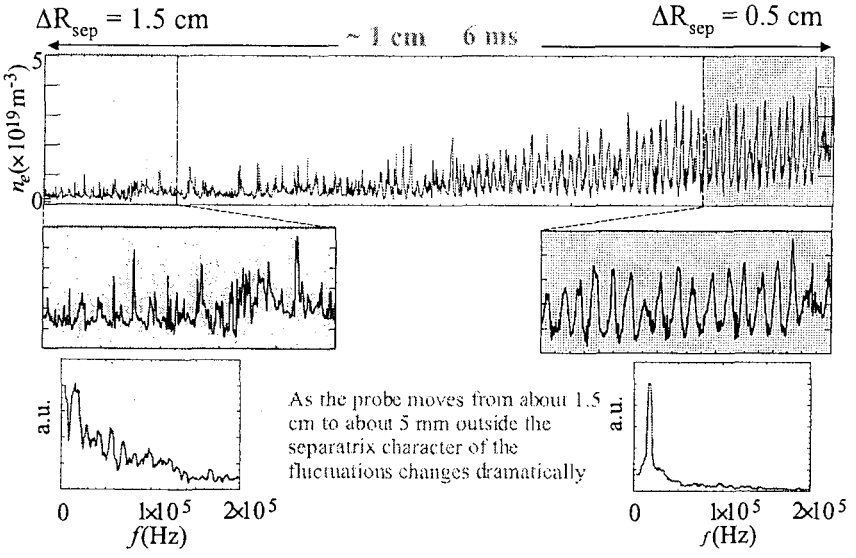

Fig. 3.48. Radial variation of density fluctuations in the near SOL of an ELM-free H-mode, showing: (left) a broadband turbulent spectrum and (right) a strong coherent oscillation.

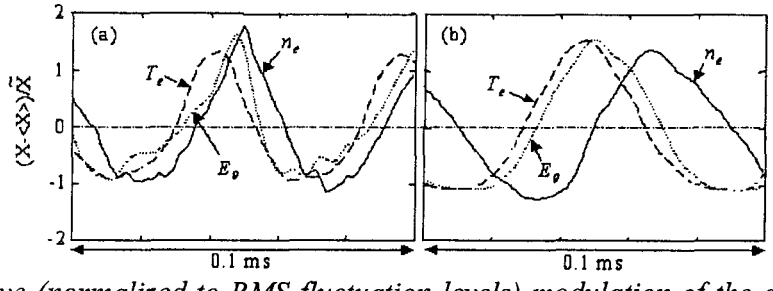

Fig. 3.49. Relative (normalized to RMS fluctuation levels) modulation of the electron density (solid), electron temperature (dashed) and poloidal electric field (dotted) by the coherent mode. In the first case the mode drives both particle and heat fluxes above L-mode levels. In the second case the mode drives only conductive heat flux.

3.7.3 QH mode and the Edge Harmonic Oscillation:

An important example of an ELM-free H-mode with high core confinement is the Quiescent H-mode, discovered at DIII-D [116]. QH modes have a number of specific requirements which differ from the conditions in which coherent or quasi-coherent edge oscillations are routinely seen as described above. QH modes require low density and effective pumping with the cryopumps; for this reason, QH modes have collisionless ions in the edge, as opposed to collisonal ions for the high density H-modes described in Section 3.7.1 and 3.7.2. QH modes to date also require neutral beam injection counter to the plasma current direction. In this

configuration, the fast ion orbits can extend deep into the SOL. The high carbon ion temperatures near the wall have been attributed to heating of the SOL by these fast ions. Reciprocating Langmuir probe measurements have also measured large positive plasma potentials near the wall in QH mode (Fig. 3.50). It might be tempting to ascribe these large potentials to the fast ion orbit losses due to counter NBI, but as is clearly shown in Fig. 3.50, discharges which remained ELMy rather than transitioning to QH mode, did not have these large potentials despite having similar levels of counter NBI. This suggests that the high potentials might be related to the presence of a strong Edge Harmonic Oscillation (EHO) in the QH modes. This oscillation is a common feature of QH mode pedestals, although some uncertainty remains concerning both the nature of the mode and its radial location. One piece of evidence to suggest that the mode close to the plasma edge but at the top of the pedestal comes from the Toroidal Tile Current Array (TTCA) signals shown in Fig. 3.51. The TTCA measures the toroidal distribution of electric currents flowing in the SOL into or out of the divertor floor. During an EHO (in a co-injected discharge that did not transition to QH mode), the EHO was seen on the TTCA rotating toroidally in the direction of the neutral beam injection with a speed of 100–110 km/s (Fig. 3.51). For an island rotating with the plasma (as opposed to a mode with an intrinsic propagation in the plasma frame), this speed corresponds to the q=4 surface, somewhat deeper in the core than the top of the pedestal. Since the density fluctuation diagnostics all see a perturbation located in the region of the steep density gradient, these disparate results will need to be resolved.

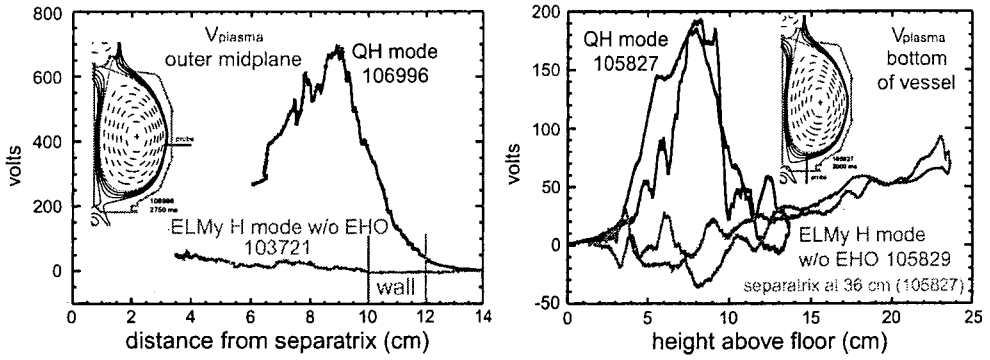

Fig. 3.50. Profiles of plasma potential on the outboard mid-plane (left) and above the lower divertor floor (right) for discharges with counter NBI that either transitioned to QH mode with a strong EHO (black) or remained ELMy (red).

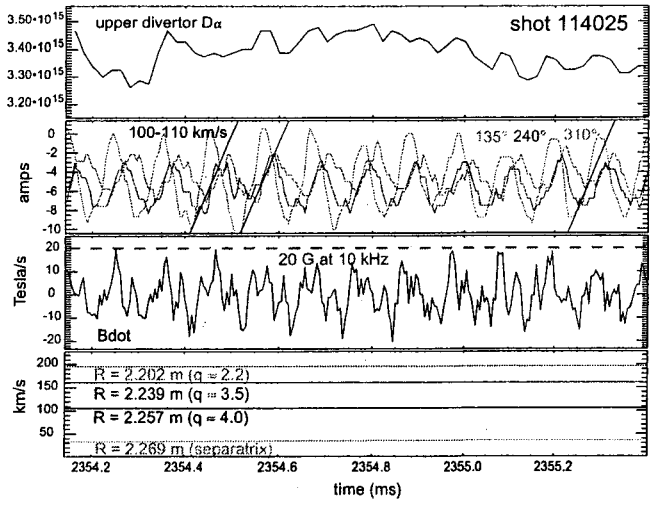

Fig. 3.51. Time dependence of (top to bottom) primary divertor D_α, TTCA currents for tiles located at 135° (red), 240° (blue) and 310° (green) showing the EHO oscillation and toroidal propagation, Mirnov Bdot signal, and the toroidal rotation calculated by the CER neural net for a set of edge chords.

3.8 Stochastic boundaries and 3-D effects in tokamaks:

Recently the 3-D character of the magnetic field in tokamaks, especially in the edge region, has received considerable attention [117]. In addition to the effect of a boundary stochastic layer on the interaction of the plasma with the plasma-facing components (altering the heat, particle, and helium exhaust, and impurity generation and penetration), there are two additional reasons for this:

- the need for external coils to control locked [118], resistive wall [119,120], and neoclassical tearing modes [121] in order to achieve high performance in Advanced Tokamak operation (high $\beta_n H$); although designed to control core modes, these coils also perturb the pedestal and scrape-off layer, resulting in stochastic layers with embedded remnant islands that alter plasma-wall interactions.
- the stochastic layer forms just inside the unperturbed seperatrix in the region of the pedestal, where it can also impact core performance due to the tight coupling of the core transport to pedestal plasma conditions [122].

Because the stochastic layer forms just inside the separatrix in the pedestal region, resonant radial magnetic perturbations may provide a means to actively control the pressure pedestal height (and consequently the core performance), as well as the edge stability and ELM behavior; power, particle and helium exhaust; and impurity screening and penetration into the plasma core.

3.8.1 Coupled plasma core and edge response to C-coil changes

Although there are various external sources of resonant radial magnetic field perturbations δb_r in the DIII-D tokamak, we illustrate the significance of δb_r for pedestal and boundary physics using a known source that is well characterized, routinely used, and externally controllable: the DIII-D C-coil (Fig. 3.52) [118]. The C-coil is used to enhance core plasma performance by nulling a presumed field error at the $q=2$ surface in order to reduce locked mode effects and the onset of resistive wall modes. The C–coil is comprised of six mid-plane saddle loops with toroidally opposing coil pairs are wired in series with antiparallel phases creating a predominantly $n=1$ toroidal perturbation spectrum with poloidal mode numbers of significant amplitude ranging from $m=1$ to 7 [118]. In CY2003, the DIII-D I-coil will be operational, consisting of an additional 12 coil segments, 6 above and 6 below the elevation of the C-coil but locating inside the vacuum vessel. The I-coil is designed for improved control of resistive wall modes, but can also provide a "clean" edge perturbation when operated in the n=3 configuration (Section 3.8.6).

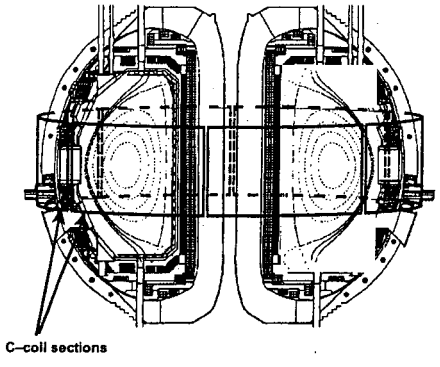

Fig. 3.52. Cutaway view of the DIII–D device showing the location of the six C–coil segments around the outer midplane of the device. Contours of constant poloidal magnetic flux ψ for a representative axisymmetric DN divertor equilibrium obtained from EFIT are shown.

Because the poloidal mode spectrum of the C-coil contains harmonics m = 1–7, the coil directly perturbs both the core and edge plasma. In high confinement regimes, the strong coupling between the core and pedestal plasma by stiff radial transport can make it difficult to separate "core effects" (e.g. locked modes) from the formation of a stochastic boundary. To illustrate this effect, we consider two similar double null diverted Ohmic plasmas. During the first 2500 ms of these discharges the C-coil is actively controlled using our standard locked mode feedback algorithm. At 2500 ms a similar change to the amplitude and phase of the six coil segments is made over a 100 ms timescale.

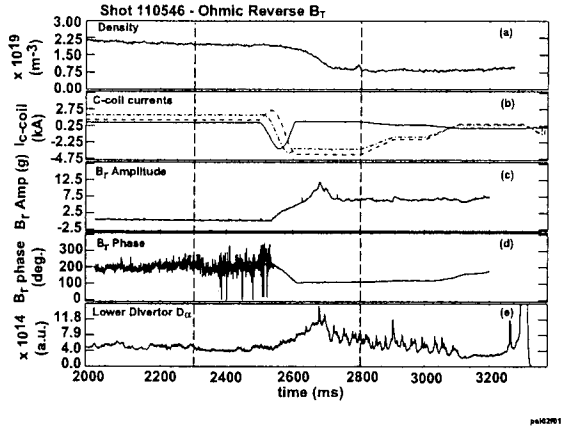

Fig. 3.53 Plasma response to a C-coil change during discharge 110546: (a) line average density, (b) C-coil currents, (c) radial error field δb_r, (d) error field δb_r phase, and (e) lower divertor D_α recycling fs04f near the outer strikepoint.

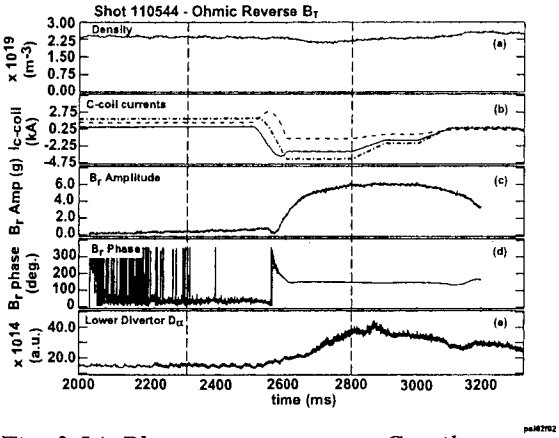

Fig. 3.54. Plasma response to a C-coil change during discharge 110544: (a) line average density, (b) C-coil currents, (c) radial error field δb_r, (d) error field δb_r phase, and (e) lower divertor D_α recycling fs04f near the outer strikepoint.

In discharge 110546 (Fig. 3.53), a core perturbation (locked mode) globally reduces confinement, as shown by the global drop in the density profile (Fig. 3.55(a) open and closed squares) and the drop in the T_e profile outside of the $q = 1.5$ surface (Fig. 3.35(b) open and closed squares). The edge perturbation (Fig. 3.54), in contrast, makes no change to the profiles at the $q = 2$ surface [Fig. 3.55(a) and (b)] where locked modes generally onset. Instead, the edge profile change is consistent with formation of a stochastic boundary layer with characteristics associated with such layers in non-diverted tokamaks: 1) T_e and n_e profile flattening locally in the edge [Fig. 3.55(c) and (d)]; 2) increased recycling consistent with connecting field lines from inside the separatrix to the divertor (Fig. 3.54); and 3) broadened particle flux profile on the divertor floor inferred from broadening of the D_α profile [123].

The TRIP3D code [124] was used to model shot 110544 at 2800 ms and 2300 ms (see the dashed lines in Fig. 3.54). At 2800 ms the unperturbed outer seperatrix position from EFIT is located at $r_{sep\_mid\_out}$=0.6349 m [Fig. 3.56(a)]. The solid violet line is the DIII-D vacuum vessel wall and the dashed blue line is the unperturbed EFIT separatrix position. The figure shows the field line r,θ positions after each toroidal transit (black, red and green dots) at a toroidal angle ϕ=120° (the Thomson scattering system location: dark blue dots near θ=60°). The field lines are started at ϕ=120°, θ=0 and $r < r_{sep\_mid\_out}$. The black dots are field lines that do not cross the unperturbed separatrix while the red and green dots are those field lines that cross the separatrix and intersect

a material surface. Red field lines are integrated in the forward B_T direction and green lines are integrated in the reverse direction.

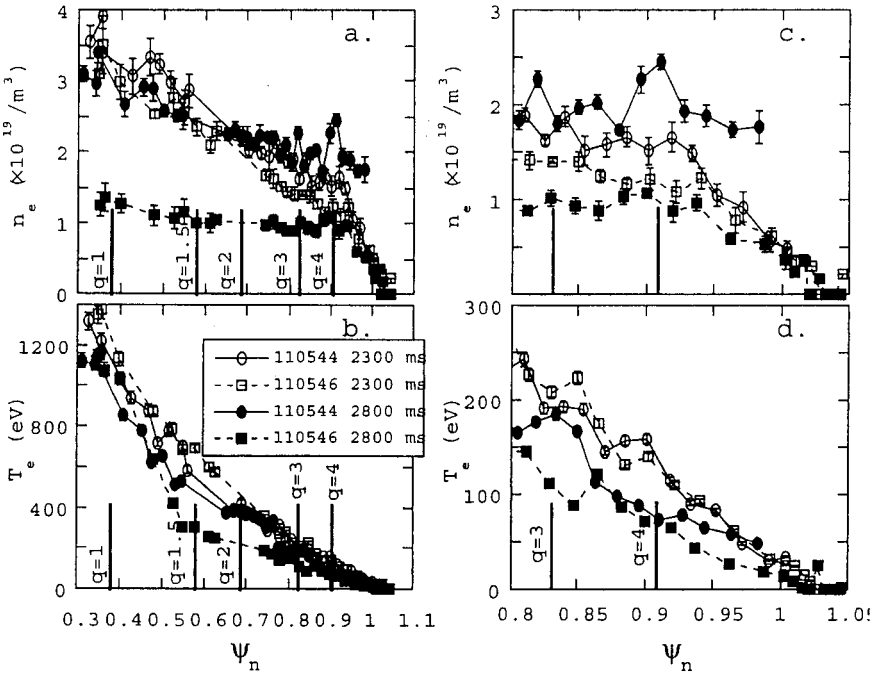

Fig. 3.55: Full (a) n_e and (b) T_e and edge (c) n_e and (d) T_e Thomson profiles for the discharges shown in figs. 1 and 2 at 2300 and 2800 ms. The profiles are averaged over 100 ms (6 Thomson time samples). The locations of the q-surfaces in the axisymmetric equilibria are indicated as vertical lines.

The modeling results demonstrate that the C-coil currents and phases at 2800 ms [Fig. 3.56(b)] produce a much broader open field line stochastic region (OFLSR) than those at 2300 ms. We find that the width of the OFLSR increases by about a factor of 2.5 at the outer midplane between 2300 and 2800 ms. Field lines were initiated at 0.5 mm steps starting about 50 mm inside the unperturbed separatrix for each timeslice. Based on the starting radius of the first field line connecting to a material surface we determine the width of the OFLSR. At 2300 ms the width of the OFLSR is 19 mm and at 2800 ms it is 44 mm. This implies that the number of Thomson scattering points sampling the OFLSR increases from 3 at 2300 ms to 9 at 2800 ms, consistent with the changes to the edge T_e profile shown in Fig. 3.55(c) and (d).

The structure of the field lines near the lower divertor x-point indicates that the footprint around the strikepoints is more complex at 2800 than at 2300 ms. In addition to those field lines lost very close to the unperturbed inner and outer divertor legs we see secondary striations further away from the legs at 2800 ms that are not seen at 2300 ms. These secondary striations intersect the divertor about 100-135 mm away from the nominal strikepoints (both along the inner wall above the inner strikepoint and outside the outer stikepoint in the outer scrape-off layer). These secondary striations indicate a significant broadening of the magnetic flux profiles on the divertor targets and thus a broadening of the heat and particle flux profiles. Comparison of these results with stochastic boundary results from limiter tokamaks shows that a significant difference is a "focusing" of the magnetic field line loss into the vicinity of the divertor.

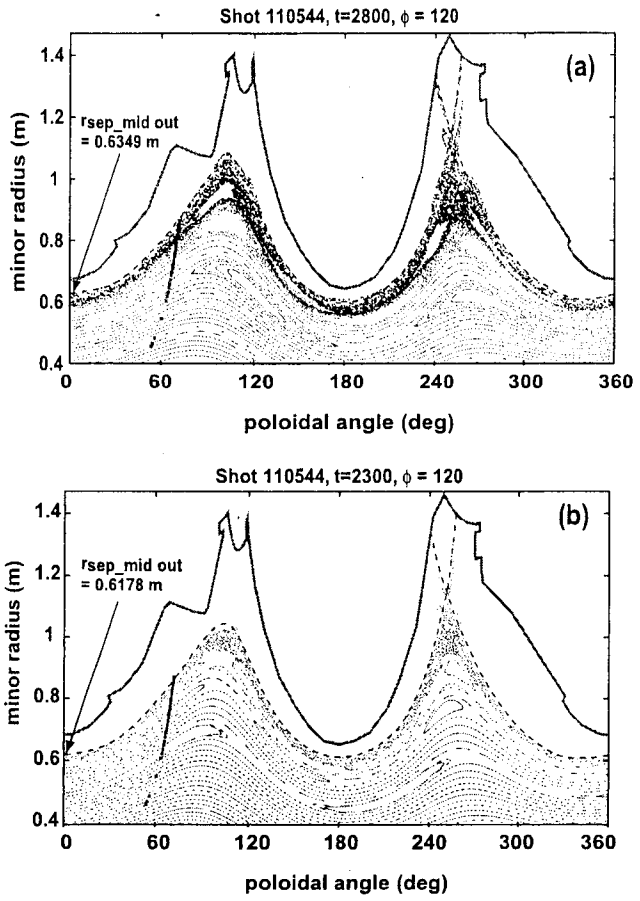

Fig. 3.56: Pedestal field line modeling results from the TRIP3D code for DIII-D shot 110544 at (a) 2800 ms and (b) 2300 ms. Black dots represent field lines that do not cross the unperturbed EFIT separatrix. Red and green dots represent field lines integrated in the forward (red) and reverse (green).B_T direction that intersect a material surface.

3.8.2 Loss of poloidal magnetic flux from the DIII-D pedestal

The TRIP3D modelling of discharge 110544 demonstrates that magnetic field lines in the edge pedestal region of the DIII-D tokamak can become stochastic for C-coil currents within the normal operating range. Simulation results showing the fractional flux loss $\delta\psi_\ell = \delta\psi_{lcfs}/\psi_{Ns}$ as a function of magnetic perturbation strength δb_r, where $\delta\psi_{lcfs}$ is the poloidal flux at the perturbed last closed flux surface and ψ_{Ns} is the normalized flux at the unperturbed separatrix, has a complex dependence on the plasma shape and the edge safety factor profile $q(\psi)$. The DIII–D C–coils are predicted, by vacuum magnetic field line integration, to lead to significant stochastic magnetic flux loss from the pedestal and separatrix region at typical operating plasma conditions and coil currents. Comparisons with the level of stochastic magnetic flux loss for nondiverted, inner wall limited (IWL) DIII–D discharges at the same δb_r strength demonstrate that diverted configurations are more sensitive to breakup of the axisymmetric flux surfaces in the boundary than nondiverted discharges. Although this sensitivity can be considered a limitation of diverted tokamak configurations, it also provides a possible mechanism for controlling the pedestal region (pedestal height and the concomitant core plasma confinement; edge stability and ELM behavior, density control and helium exhaust, and impurity penetration).

3.8.3 Sensitivity of poloidal divertor configurations

We investigate the sensitivity of the axisymmetric equilibria of poloidally diverted discharges with one [lower or upper single null (LSN) or (USN)] or two (DN) poloidal magnetic field nulls

(divertor X–points) relative to an inner wall limited case with no X–points as shown in Fig. 3.57. Much of the previous work on stochastic boundary effects in tokamaks has been performed in circular or low elongation ($\kappa \approx 1.0-1.1$) limiter discharges similar to our IWL case. The X–points in the diverted discharges lead to higher values of safety factor $q(\psi)$ and magnetic shear $s(\psi)$ in the boundary with respect to the IWL case as shown in Fig. 3.58. These variations in $q(\psi)$ and $s(\psi)$ for the diverted discharges provide additional low order resonant surfaces that are more closely spaced than in the IWL. This results in an increased sensitivity of diverted configurations to the breakup of the axisymmetric equilibrium flux surfaces and larger stochastic magnetic flux losses in most cases, a feature first reported by Skinner *et al.* [125].

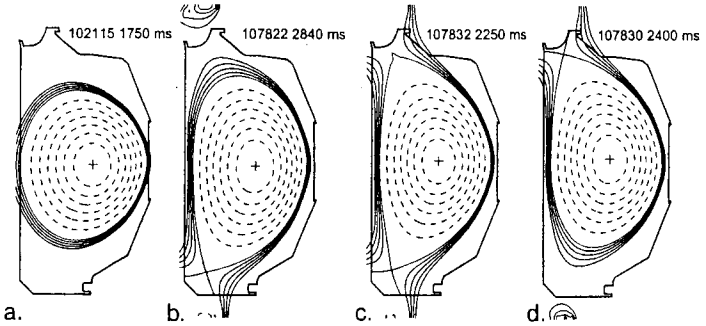

Fig. 3.57. The unperturbed, axisymmetric equilibria calculated by EFIT for this study, including: (a) IWL, (b) LSN, (c) DN, and (d) USN divertor configurations.

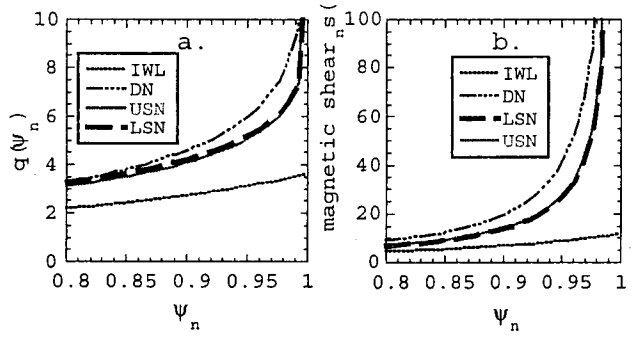

Fig. 3.58. (a) Edge safety factor $q(\psi)$ and (b) magnetic shear $s(\psi)$ profiles for the IWL, lower and upper SN and DN divertor discharges used in this study.

We focus on the region just inside the unperturbed divertor separatrix, the so-called "pedestal" region, described in DIII–D by $0.7 < \psi_N < 1.0$. This is typically equivalent to a minor radius r at poloidal angle $\theta = 0$ (the outboard midplane) between 0.5–0.65 m. The r, θ coordinates of each field line intersection with a poloidal plane after each toroidal transit, are displayed on a rectangular Poincaré plot at the toroidal angle of the Thomson scattering system $\phi = 2\pi/3$ in Fig. 3.59. These Poincaré plots show the DIII–D vacuum vessel wall and divertor structures (solid blue line), the unperturbed last closed flux surface (magenta), a single stochastic field line region (green) and an inner region of closed flux surfaces (red with remnant islands in blue dots). In Fig. 3.59(a), we show an IWL discharge and in Fig. 3.59(b) an USN discharge. The stochastic field line shown in these plots is the deepest penetrating field line at the outer mid-plane, for each configuration and C–coil current, lost to a plasma facing surface. Thus the depth of penetration, in flux space, calculated for this field line represents a measure of the flux loss for each shape and coil current.

The IWL case, shown in Fig. 3.59(a), has relatively good flux surfaces across the outer 10–12 cm of the plasma with rather large $m,n = 3,1$ and 2,1 islands residing in this region. In this case, $\delta\psi_\ell$ is of order 4% but as the current is increased from approximately 8 to 20 kA-turns these two island chains break up and the outer flux surfaces are lost across the entire region. The USN case for 8 kA-turns, Fig. 3.59(b), shows that the flux surfaces traversed by a single

stochastic field line (green) cover a region which is about 6 cm inside the unperturbed separatrix (magenta) and that this field line is lost to the upper divertor target plate region along the unperturbed strike point.

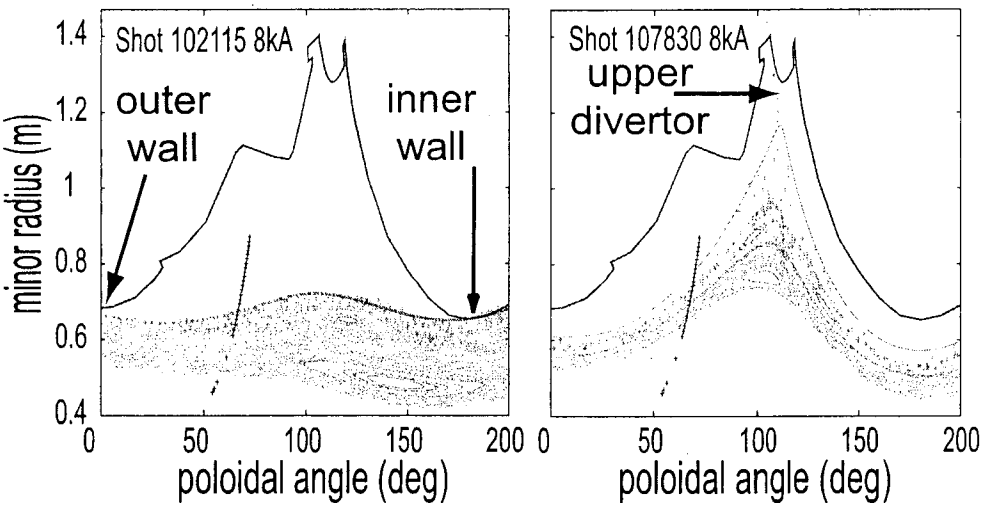

*Fig. 3.59. Rectangular Poincarié plots at a toriodal angle $\phi = 120°$ for (a) the IWL (102115 with 8 kA-turns) and (b) the USN (107830 with 8 kA-turns) discharges. The colors show, respectively: (blue solid line) the vessel wall; (magenta *) the unerturbed separatrix; (green +) a single stochastic field line that leaves the vessel; (red dots) confined field line trajectories; (blue dots) remnant island flux surfaces; and (black crosses) the Thomson scattering measurement points in the poloidal plane at $\phi = 120°$.*

For the USN case shown in Fig. 3.59(b), most of the field lines in the region $0.88<\psi_N<1.0$ terminate on the upper-outer divertor target near the strike point. Nevertheless, there are some field lines in the stochastic region that remain closed inside partially destroyed remnant islands. These remnant islands result in isolated, relatively well-confined, helical filaments that can produce nonuniformities in the measured plasma profiles. Previous measurements [126,127] of the plasma properties in these remnant islands indicate that they have a rapidly spinning vortex structure caused by an $E\times B$ drift motion due to internal electric fields of order 50 V/cm in Ohmic plasmas. The effect of these remnant islands embedded in the stochastic layer may be to modify the effective global transport in the island O–points by confining some of the plasma on a longer time scale while increasing the heat and particle flux through the island X–points.

3.8.4 Scaling of the poloidal magnetic flux loss

To better understand the behavior of $\delta\psi_\ell$ with plasma shape, $s(\psi)$ and I_c the four DIII–D discharges shown in Fig. 3.57 were modeled using TRIP3D. This set spans most of the standard experimental configurations used in DIII–D and provides a representative range of $s(\psi)$ profiles. For these scaling studies, we fix the amplitude of each coil to be either $\pm I_c$ and set the phase such that three adjoining loops (c79, c139 and c199) are all positive while the opposing loops are all negative. We then vary the coil current between 0 and 20 kA-turns in order to study $\delta\psi_\ell$ as a function of I_c and plasma shape. Figure 3.60 shows how $\delta\psi_\ell$ scales with I_c in each case.

The principal uncertainties in this calculation include: (1) some flux is trapped in small remnant island cores which results in an overestimate of the flux loss, and (2) island width effects due to the relative phasing of the island X– and O–points at the outer midplane for a fixed toroidal

angle (e.g., the inferred poloidal flux loss will vary with toroidal angle). The latter effect tends to underestimate $\delta\psi_\ell$ somewhat, compensating for the flux trapped in the remnant islands. Numerical tests indicate that these two effects combine to give a net uncertainty of ±0.005 in each $\delta\psi_\ell$ value shown in Fig. 3.60.

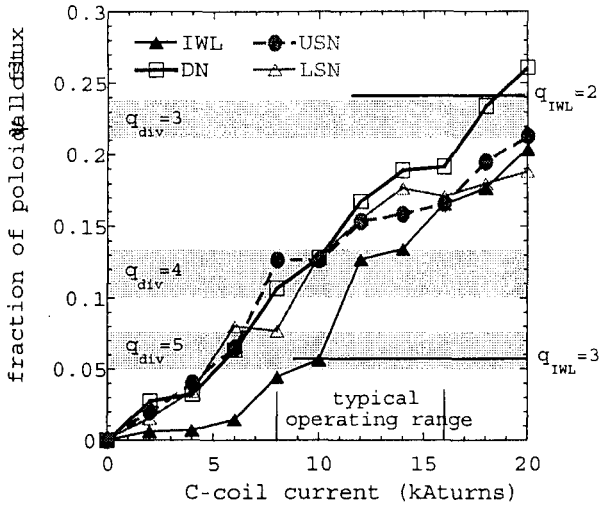

Fig.3.60: Scaling of poloidal magnetic flux loss $\delta\psi_\ell$ as a function of C–coil current in the USN, DN, LSN and IWL cases. The radial locations of the resonant q surfaces (in terms of ψ_N) are indicated for the IWL and diverted discharges.

3.8.5 Plasma response and compatibility with high performance

Previous experimental studies of the effects of stochastic boundary layers on plasmas in ohmically heated, circular limiter tokamaks have shown a dramatic flattening in the T_e profile across the stochastic region (Fig. 3.61) which substantially increases ∇T_e deeper inside the plasma [128]. Similar profile flattening has been seen under *some* conditions in DIII–D. Fig. 3.62 shows the pedestal profiles for a typical "quiescent double barrier" mode (QDB) discharge, an ELM-free H–mode discharge in the DIII–D tokamak [129]. A 3 cm flat region in T_e [Fig. 3.62(b)] and a corresponding 4 cm flat region in the plasma density [Fig. 3.62(a)] are seen during the QDB phase of this discharge, a result that is typical of QDB discharges with a strong edge harmonic oscillation (EHO) [116].

Simulations of this QDB discharge with the C–coil currents and phases in the experiment produce a 4 cm wide stochastic layer at the location of the Thomson scattering system used to measure the T_e profile. The density profile flattening seen in this case could result from the combination of an edge stochastic layer (model prediction) and the quiescent H–mode (QH) radial transport barrier (experimentally measured). Not all DIII–D discharges which are predicted to have a significant edge stochastic layer have distinct flat regions in T_e just inside the unperturbed separatrix. While this flattening is consistent with the width of the stochastic layer modeled with the TRIP3D code, it has not been shown that these flat profiles are caused by some combination of δb_r fields in the pedestal due to either the C–coil, error fields, or internal modes (such as the magnetic field of the EHO itself). A definitive proof of the existence of an edge stochastic layer in such a high performance QDB mode discharge would establish the compatibility of edge stochastic layers with high confinement operation. In contrast, definitive proof of the lack of such a stochastic layer would establish the need to better understand the nonlinear plasma response to stochastic field regions. To date, the limited experimental data available suggest that, at least for *circular limiter ohmically heated discharges*, vacuum magnetic field line integration results are a reasonable quantitative match to the real plasma response as shown in Fig. 3.63. This would indicate that little plasma "self-healing" occurs under those

conditions. In high performance discharges in DIII–D, however, the additional power flow or momentum input from high power neutral beam heating might produce a plasma response which significantly heals the stochasticity via plasma rotation or some other effect. Understanding the self-consistent plasma response is critical for interpreting experimental results for tokamak pedestal and scrapeoff layer physics, and for developing predictive models of the edge plasma in tokamaks. Such understanding might, in turn, lead to new techniques for controlling the pedestal and boundary of high performance tokamaks.

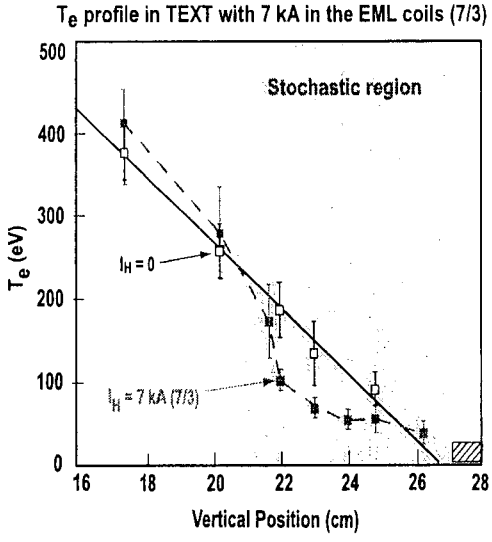

Fig. 3.61. Formation of an H-mode like gradient in the T_e profile across the stochastic region formed in the TEXT tokamak with 7 kA of current in the Ergodic Magnetic Limiter coils [10]. Note that the steep gradient region forms inside the region predicted to be stochastic.

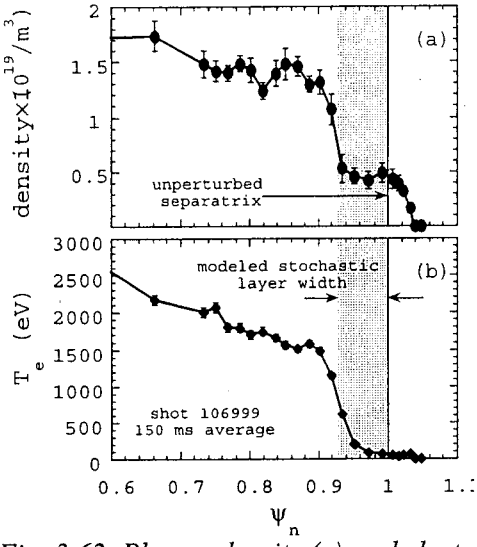

Fig. 3.62. Plasma density (a) and electron temperature (b) profiles measured by Thomson scattering for shot 106999 (USN) showing flat regions at the edge conincident with the stochastic layer width modelled with the vacuum field line integration code TRIP3D.

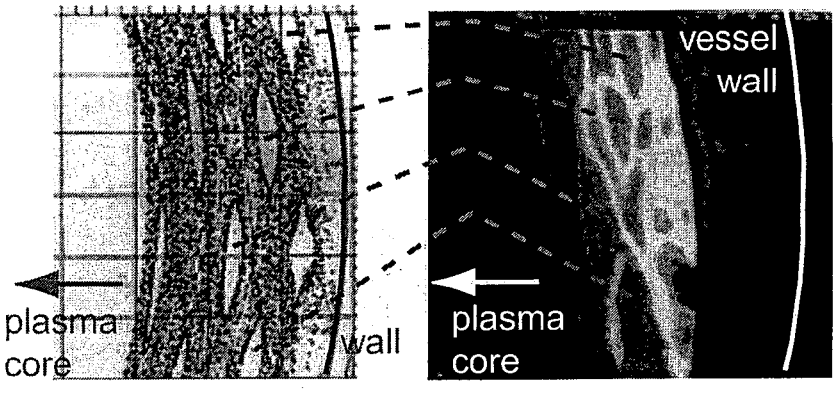

Fig. 3.63. Comparison of a TRIPND vacuum field line integration simulation (left) with an image of the stochastic layer for an ohmic discharge with 15 kA in the ergodic divertor coils at Tore Supra. The image is a tangential view of total visible light taken near the high field side plasma facing surface. The spatial scales of the image and the simulation are approximately the same. Red dashed lines indicated island remnants within the stochastic layer which are reproduced quantitatively in the simulation (both location and size).

3.8.6 The I-coil and dedicated stochastic boundary experiments in DIII-D

A significant drawback to using the C-coil for stochastic boundary experiments in DIII-D is the mode spectrum of the resulting radial magnetic field perturbation, which contains poloidal mode numbers $1 \leq m \leq 6$ for an n=1 perturbation. This results in perturbations to both the core (e.g. $q = m/n = 2$) and boundary (e.g. $q = m/n = 4$ to 6). In CY 2003, the DIII-D I-coil will be fully operational and capable of producing a relatively "clean" (essentially free of perturbation with significant resonance inside $q = 3$) edge stochastic layer. While the I-coil is designed to be operated in an $n = 1$ configuration to control RWMs and neoclassical tearing modes, it can also be operated in an $n = 3$ configuration that provides a relatively good perturbation source for exploring the physics of stochastic pedestal control. The I-coil provides a flexible dual parity $n = 3$ mode spectrum with reasonably good time response and current limit capabilities. Dedicated stochastic boundary control experiments will begin in CY 2003 involving direct participation by international experts from Germany, France, Japan, and Australia. These experiments will explore the potential for using edge stochastic layers to control pedestal profiles, impurity and neutral penetration depths, and edge MHD stability (particularly for ELMs). The results will form the basis for designing a dedicated stochastic boundary control coil which is being considered for installation in DIII-D during the next five year plan. The I-coil has been implemented in TRIP3D, and will be used to model the results of these experiments, and to design the dedicated stochastic layer control coils.

3.8.7 Stochastic magnetic fields and ELMs

ELMs remain a critical concern for ITER and other burning plasma experiments due to: 1) the erosion of the divertor target plates by the impulsive heat flux from large ELMs, and 2) by the tritium inventory in the plasma-facing components when the eroded material is co-deposited with hydrogenic species [130]. Controlling ELMs, however, is complicated by the need to provide a steady-state operating environment with density control and without impurity build-up in the absence of the transport associated with ELMs. While ELMs are not yet fully understood, some researchers have suggested that the high transport rates associated with large ELMs might arise due to partial ergodization of the boundary magnetic field lines. At least two different steady-state regimes with H-mode edge transport barriers and without large ELMs have been demonstrated: QH mode in DIII-D [130] and ASDEX-Upgrade, and EDA H-mode in C-Mod [131]. Each of these regimes rely on particle transport by electromagnetic modes (Edge Harmonic Oscillation in QH mode [Fig. 3.64(a)]; Quasi-Coherent Mode in EDA H-mode [Fig. 3.64(b)]) located in the pedestal [Fig. 3.64(c) and (d)] to maintain density control and to avoid impurity accumulation. These regimes, however, have limited operating windows, and development of an active control scenario that could be used over a wider range of operation would improve the viability of a burning plasma experiment.

Because ELM behavior (amplitude and frequency) are sensitive to MHD stability in the boundary, which in turn depends upon the edge pressure and current profiles, edge resonant radial magnetic field perturbations might provide a means for active control of ELMs and the H-mode pedestal [132]. This report has already demonstrated a number of favorable features of such an approach, including:

- The pedestal region of divertor tokamaks is inherently more sensitive than the edge of a limiter tokamak to break up of the magnetic flux surfaces into an edge stochastic layer; thus, control coils need to provide only a relatively small perturbation (low coil current).

- The resulting stochastic layer is localized radially by the high edge magnetic shear; thus, overall confinement might not be adversely affected.
- The stochastic field lines are lost near the divertor X-point(s) into the divertor chamber rather than from around the entire plasma column; thus, the tokamak is still diverted.
- The stochastic layer broadens the target plate particle and heat fluxes to further reduce erosion rates.
- The edge stochastic layer provides enhanced screening of impurities from the plasma core, a well documented feature of boundary stochastic layer experiments in tokamaks such as TEXT and Tore Supra.

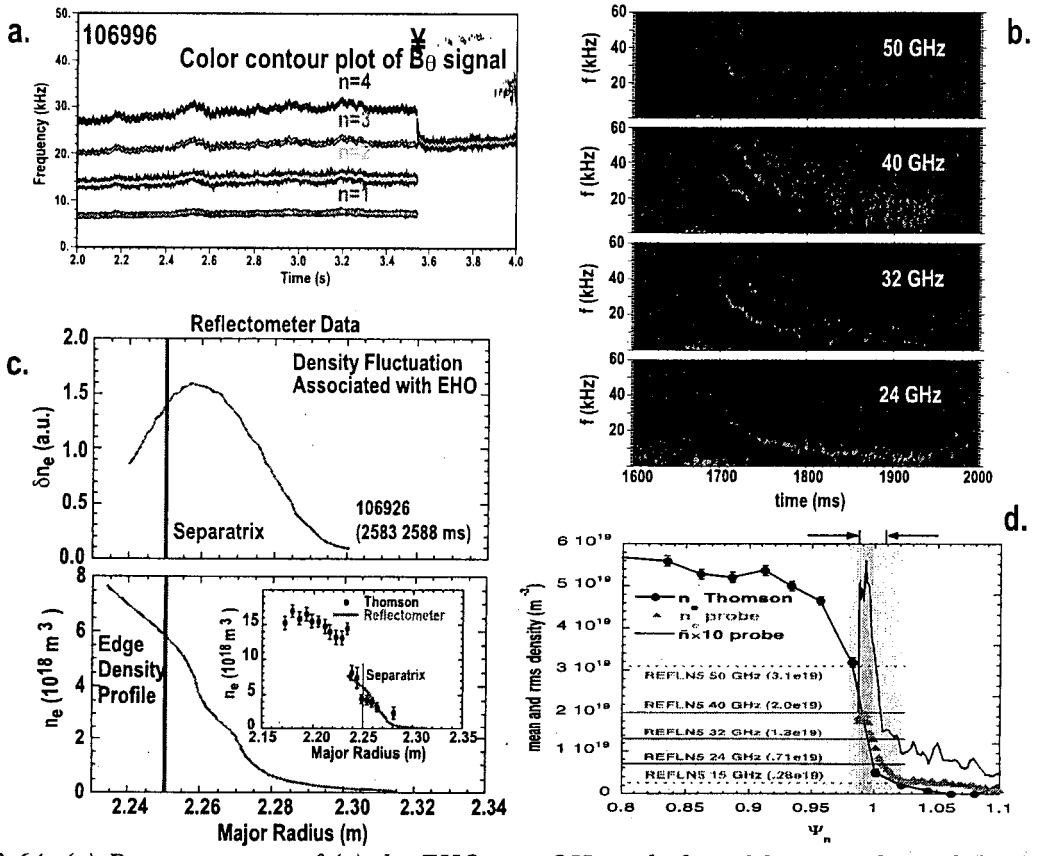

Fig. 3.64. (a) Power spectra of (a) the EHO in a QH mode from Mirnov coils, and (b) the QC mode from reflectometry in a C-Mod dimensionless scaling discharge in DIII-D. Both modes are localized to the bottom of the H-mode pedestal as shown in (c) for QH mode and (d) for EDA H-mode.

DIII-D data already demonstrate that the ELM amplitude and frequency change following a change in the C-coil currents, as shown in Fig. 3.65. However, the C-coil perturbs both the core (q = 2 surface) and the edge, which complicates the interpretation of the results. There is an onset in MHD activity at 2510 ms, followed by a locked mode at 2840 ms. The availability of the I-coil, consisting of 12 segments, 6 mounted above the C-coils and 6 mounted below the C-coils in CY2003 provides the capability of using an edge resonant magnetic perturbation in n=3 mode. Experimental time has been allocated in CY03 at DIII-D to investigate ELM control using this

edge resonant perturbation in collaboration with an extensive group of international scientists. The ability to model the results of these experiments may prove crucial in designing effective ELM/pedestal control scenarios using a boundary stochastic layer.

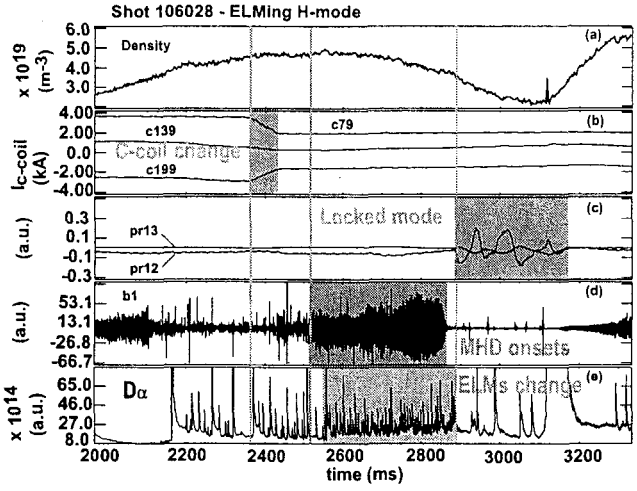

Fig. 3.65. Change in ELM frequency and amplitude following a C-coil magnetic perturbation at 2350-2400 ms. (a) plasma density, (b) Coil currents, (c) saddle loop signals indicating a locked mode at 2900 ms, (d) fast Mirnov signal, and (e) divertor D_α.

The stabilization of MHD modes by moving the resonant surface of the mode sufficiently close to a poloidal divertor separatrix to produce a stochastic layer around the separatrix has already been demonstrated for (1,1) internal kink and (2,1) tearing modes both computationally [133] and experimentally [134]. In the context of ELM control in QH and EDA modes, the radial magnetic field perturbation associated with the EHO and QC modes (Fig. 3.64) in the pedestal might be sufficient to produce an edge stochastic layer without the effects of the C-coil considered in the previous section. In this sense, both QH mode and EDA H-mode might already represent inadvertent realizations of ELM control via edge stochastic layers [132].

3.9 Type I ELM suppression with n=3 edge resonant I-coil perturbations

With the availability of the I-coil in CY 2003, an international team of scientists conducted the first experiments using an edge resonant magnetic perturbation of 1 part in 10^4 from the I-coil to control large Type I ELMs in DIII-D [135,136]. The applied perturbation had a toroidal mode number n = 3 and a range of edge resonant poloidal harmonics $9 < m < 14$ (Fig. 3.46). Vacuum field line integration modeling predicts that this relatively weak perturbation produces a chain of non-overlapping islands spanning the pedestal region [Fig. 3.66(right)].

Nonetheless, this perturbation suppressed ELMs for periods of up to 8.6 τ_E in a range of high performance H-modes with a pedestal collisionality $\nu_e^* \sim 1$ without degrading core confinement (Fig. 3.67). Measurements of the surface temperature rise from an IRTV in fast line scan mode comfirm that during the ELM suppression, the energy impulses to the divertor target plates are reduced by at least a factor of 5 [136] (Fig. 3.68).

The total pressure profile in these discharges was relatively unaffected by the applied perturbation, resulting in a pedestal pressure gradient ∇p^{TOT} near the peeling-ballooning boundary [137] (Fig. 3.69). Instead, the Type I ELMs are suppressed by enhancing small events, possibly Type II ELMs [138], associated with increased intermittent "blob" transport [139] (Fig. 3.70). These rapid, small amplitude events provide a more constant power loss from the boundary, reducing the impulsive loading to the target plates while providing the same steady state power loading overall [136]. If there are enough of these events, the resultant transport holds ∇p^{TOT} just below the stability limit for the large Type I ELMs (Fig. 3.71).

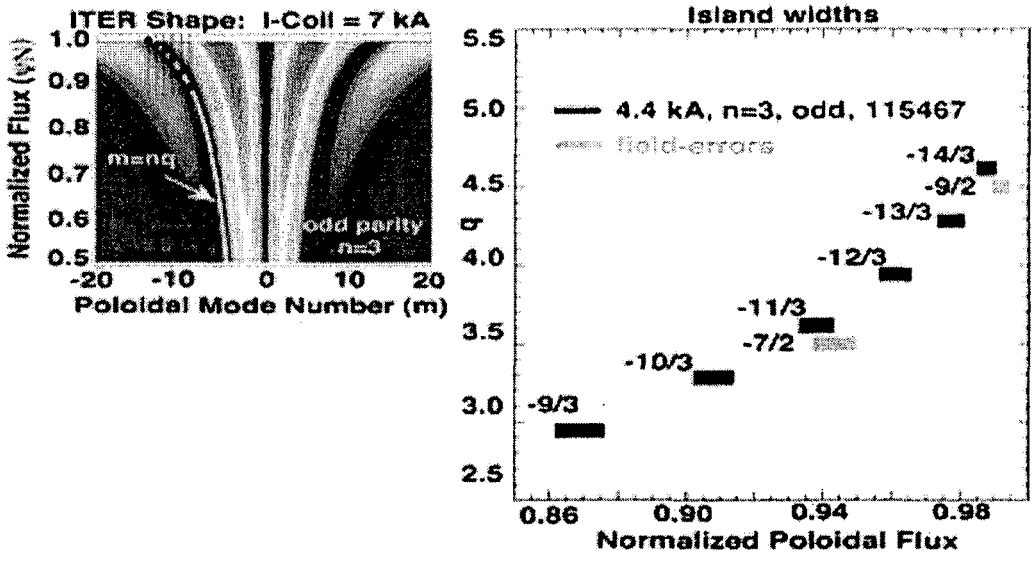

Fig. 3.66. (left) Color contour plot of the applied radial magnetic field $\delta b_r^{m,n}$ from the I-coil as a function of poloidal mode number m and plasma radius (in terms of the normalized poloidal magnetic flux ψ_n). in the ELM control experiments. The white line indicates the pitch-resonant portion of the spectrum, m = nq. The applied harmonics are relatively weak in the configuration used since the pitch resonant line lies in the "valley" in the $\delta b_r^{m,n}$ amplitude. (right) Island widths (black bars) in the pedestal region resulting from the perturbation spectrum shown on left. There is no significant island overlap. The known field errors (green bars) are shown for comparison. The island widths are comparable to the field errors in the device.

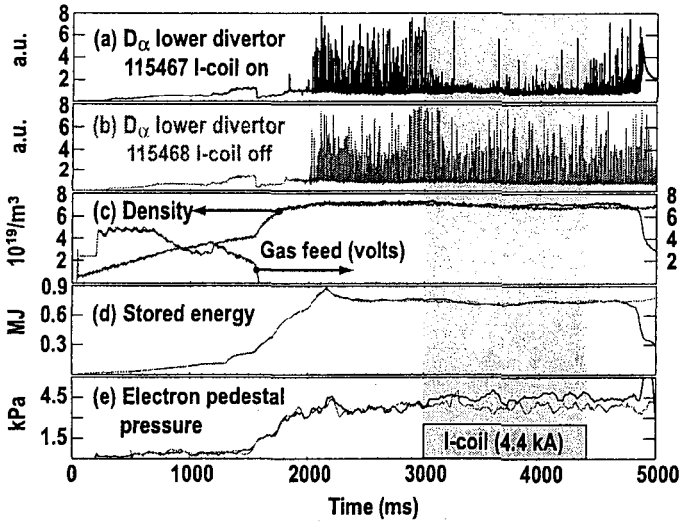

Fig. 3.67. Comparison of ELM suppression and core confinement in identical discharges with (115467, black0 and without (115468, red) an n=3 I-coil pulse of 4.4 kA: D_α recycling in the lower divertor for (a) 4.4 kA from 3000 to 4400 ms (shaded) and (b) reference discharge with I-coil current = 0 kA. The plasma density and gas feed (c) and the plasma stored energy (d) for the ELM suppression discharge (black) and the reference (red). (e) The electron pedestal pressure with (black) and without (red) the I-coil pulse.

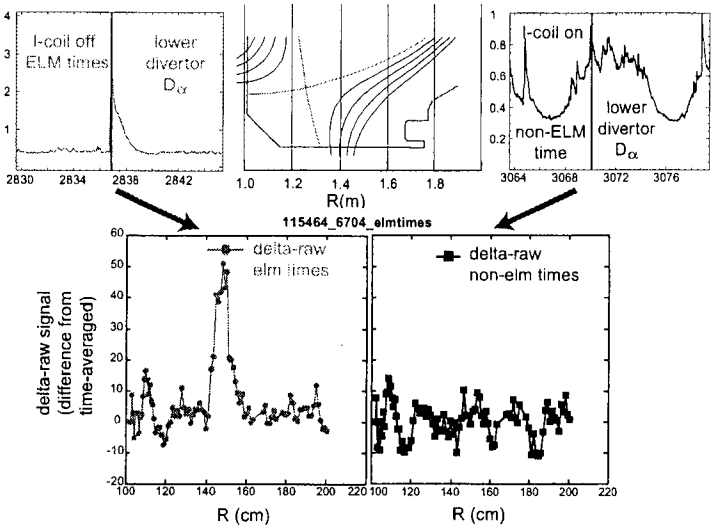

Fig. 3.68. Fast surface temperature measurement using an IRTV in line scan mode, comparing (red) the profile of the surface temperature rise (lower left) across the divertor floor (top center) for a typical ELM with I-coil =0 kA (top left) and (black) the surface temperature rise (lower right) during the small events (top right) for I-coil = 4.4 kA. Surface temperature profiles are measured at the times indicated by the blue lines.

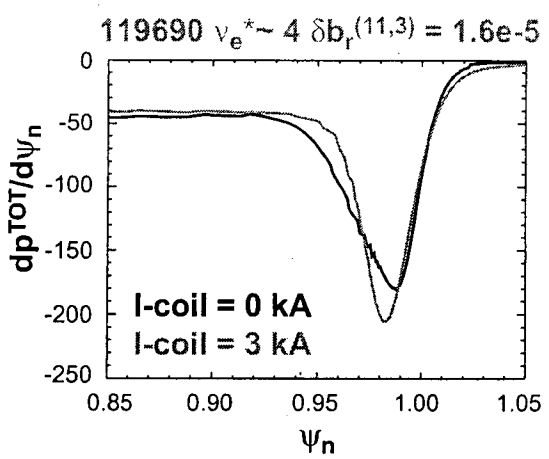

Fig. 3.69. Comparison of the total pressure profile gradient ∇p^{TOT} in the pedestal with (black) I-coil = 0 kA and (green) I-coil = 4.4 kA.

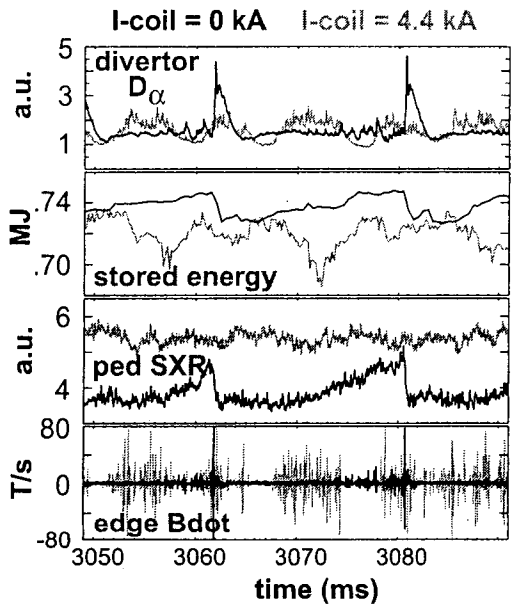

Fig. 3.70. Comparison of Type I ELM behavior for (black) I-coil = 0 kA and (green) I-coil = 4.4 kA, showing, top to bottom: divertor D_α, plasma stored energy, pedestal SXR emissivity, and magnetic fluctuations from the edge.

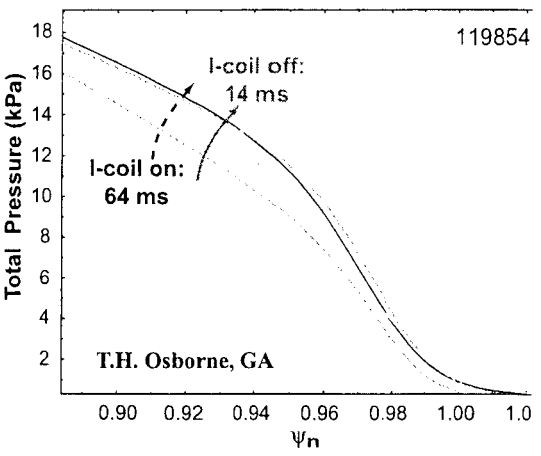

Fig. 3.71. Comparison of the evolution of the total pedestal pressure profile pTOT over an ELM cycle with (solid lines) I-coil = 0 kA and (dashed lines) I-coil = 4.4 kA. In the 4.4 kA case, the large Type I ELMs were not completely surpressed. The time between successive ELMs increased from 14 ms (0 kA) to 64 ms (4.4 kA) due to the delay in recovery of the profile following a large ELM caused by the increased transport associated with the small events..

These results demonstrated conclusively that edge resonant magnetic perturbations could be used effectively to control ELM and pedestal behavior without degrading core confinement. Additional experiments will be needed to extend this ELM control technique to H-modes with ITER-relevant pedestal collisionalities ($\nu_e^* < 0.1$), edge safety factor ($q_{95} \sim 3$), and toroidal rotation before the viability of this ELM control technique in ITER can be assessed.

References for Section 3:

[1] Project Staff, "The DIII-D Five-Year Program Plan 2003–2008," General Atomics Report GA-A23927 (2003) pp. 1-2.

[2] M.E. Fenstermacher et al., Contributions to Plasma Physics **36** (1996) 127.

[3] W.P. West et al., Plasma Phys. Control. Fusion **39** Suppl. 5A (1997) 295.

[4] R.A. Moyer et al., J. Nucl. Mater. **241-243** (1997) 633.

[5] J.A. Boedo,et al., Phys. Plasmas **5** (1998) 4305.

[6] J.A. Boedo et al., J. Nucl. Mater. **266-269** (1999) 783.

[7] G.D. Porter et al., Phys. Plasmas **7** (2000) 3663.

[8] S.L. Allen et al., J. Nucl. Mater. **290-293** (2001) 995.

[9] X.Q. Xu, et al., J. Nucl. Mater. **266-269** (1999) 993.

[10] X.Q. Xu, et al., Nucl. Fusion **40** spec. issue, (2000) 731.

[11] X.Q. Xu, et al. Nucl. Fusion **42** (2002) 21.

[12] B.A. Carreras IEEE Trans Plasma Sci **25** (1997) 1281.

[13] F. Wagner et al., Phys. Rev. Lett. **49** (1982) 1408.

[14] H.Y.W. Tsui et al., Rev. Sci. Instrum. **63** (1992) 4608.

[15] C. Hidalgo, et al., Phys. Rev. Lett. **69** (1992) 1205.

[16] J.A. Boedo et al., Rev. Sci. Instrum. **70** (1999) 2997.

[17] D.L. Rudakov et al., Rev. Sci. Instrum. **72** (2001) 453.

[18] P. Diamond and T.S. Hahm, Phys. Plasmas **2** (1995) 3640.

[19] D. Newman *et al.*, Phys. Plasmas **3** (1996) 1858.

[20] B.A. Carreras, *et al.* Phys. Plasmas **3** (1996) 2903.

[21] F.F. Chen, Phys. Rev. Lett. **15** (1965) 381.

[22] M.A. Pedrosa, *et al.*, Phys. Rev. Lett. _____ (1999) _____.

[23] P. Bak, *et al.* Phys. Rev. Lett. **59** (1987) 381.

[24] T.L. Rhodes, *et al.*, Phys. Lett. A **253** (1999) 181.

[25] K.H. Burrell, Phys. Plasmas, **6**, (1999) 4418.

[26] R.J. Groebner, K.H. Burrell,, and R.P. Seraydarian, Phys. Rev. Lett. **64** (1990) 3015.

[27] P.W. Terry, Rev. Mod. Phys. **72** (2000) 109.

[28] H. Biglari, P.H. Diamond, and P.W. Terry, Phys. Fluids B **4** (1990) 1385.

[29] A. Hasegawa and M. Wakatani, Phys. Rev. Lett. **59** (1987) 431.

[30] W. Horton and A. Hasegawa, Chaos **4** (1994) 227.

[31] Z. Lin et al. Science **281** (1998) 1835.

[32] M. Beer et al. Plasma Phys Contr. Fusion **35** (1993) 973.

[33] A. Dimits et al. Phys. Rev. Lett. **77** (1996) 71.

[34] R.D. Sydora et al. Plasma Phys. Contr. Fusion **38** (1996) A281.

[35] P.H. Diamond et al. Proc. 18th IAEA Fusion Energy Conf. (4-10 October 2000, Sorrento, Italy), IAEA-CN-77/TH2/1 (2000).

[36] P.H. Diamond and Y.-B. Kim, Physics of Fluids **3** (1991) 1626.

[37] P.H. Diamond, et al. Phys. Rev. Lett. **84** (2000) 4842.

[38] G.R. Tynan, et al. Phys. Plasmas **8** (2001) 2691.

[39] R.J. Taylor et al., Phys. Rev. Lett. **63** (1989) 2365.

[40] R.R. Weynants et al., Nucl. Fusion **32**(1992) 837.

[41] R. E. Waltz et al., Phys. Plasmas **2**, (1995) 2408.

[42] X. H. Wang, P. H. Diamond and M. N. Rosenbluth, Phys. Fluids B **4** (1992) 2402.

[43] K. C. Shaing, E. C. Crume and W. A. Houlberg, Phys. Fluids B **2** (1990) 1492.

[44] K. Itoh and S. Itoh, Phys. Plasmas Controlled Fusion **38**, (1996) 1.

[45] K. C. Shaing, E. C. Crume Jr and W. A. Houlberg, Phys. of Fluids B **2** (1990) 1492.

[46] Y. Z. Zhang and S. M. Mahajan, Phys. Fluids B **4** (1992) 1385.

[47] R.A. Moyer et al. Phys. Plasmas **2** (1995) 2397.

[48] A. S. Ware, et al., Phys. Plasmas **5** (1998) 173.

[49] R.J. Colchin et al., Phys. Rev. Lett **88** (2002) 255002.

[50] R.J. Colchin et al., Nucl. Fusion **42** (2002) 113.

[51] J.-N. Leboeuf, L.A. Charlton, and B.A. Carreras, Phys Fluids **B 5** (1993) 2959.

[52] D.L. Rudakov et al., Plasma Phys. Cont. Fusion **43** (2001) 559.

[53] B.A. Carreras et al. Phys. Plasmas **1** (1994) 4014.

[54] B.N. Rogers, J.F. Drake, and A. Zeiler, Phys. Rev. Lett. **81** (1998) 4396.

[55] G. R. McKee et al., Phys. Plasmas **10** (2003), 1712.

[56] J.C. Luxon, L.G. Davis, Fusion Technology **8**, Part 2A (1985) 441.

[57] J.A. Boedo, *et al.* Phys. Plasmas **5** (1998) 4305.

[58] G.D. Porter and the DIII-D Team, Proc. 23rd European Conf. On Controlled Fusion and Plasma Physics, June 24–28, 1996, Kiev, Ukraine, **20C**, Part II, (European Physical Society, Petit-Lancy, Switzerland, 1996) 699.

[59] S.I. Braginskii, Reviews of Plasma Physics, edited by M.A. Leontovich (Consultants Bureau, New York, 1965), Vol. I, 205.

[60] A.W. Leonard, *et al* Phys. Rev. Lett. **78** (1997) 4769.

[61] C.J. Lasnier, *et al.,* Nucl. Fusion **38** (1998) 1225.

[62] J.A. Boedo, *et al.*, Phys. Plasmas **7** (2000) 1075.

[63] T.D. Rognlien, G.D. Porter, and D.D. Ryutov, J. Nucl. Mater. **266-269** (1999) 654.

[64] J.A. Boedo, *et al.*, Conf. Abstracts, 25th European Conference on Controlled Fusion and Plasma Physics 1998, ECA **23J** (1999) 1185.

[65] M.R. Wade, *et al.* J. Nucl. Mater. **266-269** (1999) 44.

[66] J.A. Boedo, *et al.*, Nucl. Fusion **40** (2000) 209.

[67] G.L. Jackson, *et al.*, J. Nucl. Mater. **266-269** (1999) 380.

[68] R.R. Dominuez, Nucl. Fusion **31** (1991) 2063.

[69] M. Fröjdh, M. Liljeström, and H. Nordman, Nucl. Fusion **32** (1992) 419.

[70] P.C. Stangeby, "The plasma boundary of magnetic fusion devices", IoP (200) 46.

[71] P.C. Stangeby, G. McCracken, Nucl. Fusion **30** (1990).

[72] J.A. Boedo, et al. Rev. Sci. Instrum. **69** (1998) 2663.

[73] B. LaBombard et al. Nucl. Fusion **4** (2000) 2041.

[74] M.R. Wade, et al., J. Nucl. Mater. **266-269** (1999) 44.

[75] A.H. Nielsen, et al. Phys. Plasmas **3** (1996) 1530.

[76] R.D. Lehmer. PhD thesis, University of California Los Angeles, UCSD-ENG-032, (1996).

[77] E. Sanchez, et al., Phys. Plasmas, **7** (2000) 1408.

[78] B.K. Joseph, et al., Phys. Plasmas **4** (1997) 4292.

[79] R.A. Moyer, et al., Plasma Phys. Control. Fusion **38** (1996) 1273.

[80] R. Jha and Y. C. Saxena, Phys. Plasmas **3** (1996) 2979.

[81] C. Hidalgo, et al., Fizika Plazmy **23** (1997) 562.

[82] B. Carreras, et al, Phys. Plasmas **7** (2000) 3278.

[83] W. Press, S. Teukolsky, W. Vettering and B. Flannery, "Numerical Recipes in Fortran", Cambridge University Press, (1986), 606.

[84] J.A. Boedo, et al., Phys. Plasmas **8** (2001) 4826.

[85] D.L. Rudakov, et al, Plasma Phys. Control. Fusion **44** (2002) 717.

[86] A.V. Filippas, et al, Phys. Plasmas **2** (1995) 839.

[87] J. Soteckel, et al. Phys. Plasmas **6** (1999) 846.

[88] G. Antar, et al. Phys. Rev. Lett. **87** (2001) 065001.

[89] G. Antar, et al., Phys. Plasmas **8** (2001) 1612.

[90] I. Garcia-Cortes, et al. Plasma. Physics. Control. Fusion **42** (2000) 389.

[91] B. La Bombard, et al., Phys. Plasmas **8** (2001) 2107.

[92] S.J. Zweben and S.S. Medley, Phys. Fluids B **1** (1989) 2058.

[93] R. Maqueda, G. Wurden, S. Zweben et al., Rev. Sci. Instrum. **72**, (2002) 931.

[94] J.A. Boedo et al., J. Nucl. Mater. **313-316** (2003) 813.

[95] J.A. Boedo et al., Phys. Plasmas **10** (2003) 1670.

[96] Y. Sarazin and Ph. Ghendrih Phys. Plasmas **5** (1998) 4214.

[97] A.W. Leonard, et al. J. Nucl. Mater. **266-269** (1999) 109.

[98] A. W. Leonard, et al., J. Nucl. Mater. **290-293** (2001) 1097.

[99] J.W. Connor, Phys. Plasmas **5** (1998) 2687

[100] P.B. Snyder et al., Phys. Plasmas **9** (2002) 2037.

[101] P.B. Snyder et al., IAEA Fusion Energy Conference, Lyon, France (2002), submitted to Nucl. Fusion.

[102] H.R. Wilson et al., Phys. Plasmas **9** (2002) 1277.

[103] J.A. Boedo et al., "ELM dynamics and Transport in the SOL of the DIII-D Tokamak," submitted to: Phys. Plasmas 2003.

[104] M.E. Fenstermacher et al., "ELM Particle and Energy Transport in the SOL and Divertor of DIII-D," submitted to: Plasma Phys. Cont. Fusion.

[105] M. Groth, et al. J. Nucl. Mater. **313-316** (2003) 1071.

[106] M. Groth et al, Rev. Sci. Instrum. **74** (2003) 2064.

[107] X. Xu and R.H. Cohen, Contrib. Plasma Phys. **36** (1996) 202.

[108] J.R. Myra *et al.*, Phys. Plasmas **4** (1997) 1330.

[109] X. Xu, *et al.* Phys. Plasmas **7** (2000) 1951.

[110] R.A. Moyer *et al.*, J. Nucl. Mater. **266-269** (1999) 1145.

[111] X. Xu, *et al.* J. Nucl. Mater. **266-269** (1999) 993.

[112] X. Xu, *et al.*, Nucl. Fusion **40** (2000) 731.

[113] D.A. Mossessian, et al. Phys. Plasmas **10** (2003) 689.

[114] R.J. Groebner, et al., Plasma Phys. Control. Fusion **44**, suppl.5A (2002) A265.

[115] R.A. Moyer, et al., Plasma Phys. Control. Fusion **41** (1999) 243.

[116] K.H. Burrell, et al., Plasma Phys. Control. Fusion **44**, suppl.5A (2002) A253.

[117] Workshop on Future Directions in Theory of 3D Magnetic Confinement Systems Summary Report, ORNL, 2002.

[118] R.J. La Haye, A.W. Hyatt, S.T. Scoville, Nucl. Fusion **32** (1992) 2119.

[119] M. Okabayashi, J. Bialek, M.S. Chance, et al. Phys. Plasmas **8** (2001) 2071.

[120] A.M. Garofalo, T.H. Jensen, L.C. Johnson et al., Phys. Plasmas **9** (2002) 1997.

[121] R.J. La Haye, et al. Phys. Plasmas **9** (2002) 2051.

[122] T.H. Osborne, et al., Plasma Physics and Controlled Fusion, 42, Suppl. 5A (2000) A175.

[123] T.E. Evans and R.A. Moyer, J. Nucl. Mater. **313-316** (2003) 1282.

[124] T.E. Evans, R.A. Moyer, and P. Monat, Phys. Plasmas **9** (202) 4957.

[125] D.A. Skinner, et al. Phys. Fluids B **30** (1987) 1218.

[126] S. Takamura, et al., Phys. Fluids **30**, (1987) 144.

[127] T. Evans, et al., Proceedings of the 14th European Physical Society Conference on Controlled Fusion and Plasma Physics, Madrid 1987 (European Physical Society, Petit-Lancy, 1987) Vol. IID, p. 770.

[128] T.E. Evans, et al., J. Nucl. Mater. **145-146** (1986) 812.

[129] K.H. Burrell, et al., Phys. Plasmas **8** (2001) 2153.

[130] G. Federici et al.,"Plasma-material Interactions in Current Tokamaks and their Implications for Next-step Fusion Reactors," A joint report with Princeton Plasma Physics Laboratory, Princeton, NJ, USA (PPPL-3531) and the Max-Planck-Institut fur Plasmaphysik, Garching, Germany (IPP-9/128), January 2001.

[131] M. Greenwald et al., Plasma Physics & Controlled Fusion, **42**, suppl.5A, (2000) A263; A. Mazurenko, Phys. Rev. Lett. **89** (2002) 225004.

[132] R.A. Moyer et al., "Prospects for ELM and pedestal control with edge resonant magnetic perturbations," U.S.-E.U. Transport Task Force Meeting, Madison WI, 2003.

[133] E. Uchimoto, J.D. Callen, Zuoyang Chang, S.C. Prager, Phys. Plasmas **1** (1994) 648.

[134] R.A. Moyer, "*Magnetic and Material Limiter Discharges in Tokapole II*," Ph.D. thesis, U. Wisconsin-Madison, 1988.

[135] T.E. Evans, et al., Phys. Rev. Lett. **92** (2004) 235003-1.

[136] R.A. Moyer, et al., Phys. Plasmas **12** (2005) 056119-1.

[137] R.A. Moyer, et al., "ELM control with n=3 Magnetic Perturbatons," contributed oral presentation at the 47th Annual Meeting of the Division of Plasma Physics, American Physical Society, Denver CO 10/2005; abstract published in: Bull. Amer. Phys. Soc. **50** (2005) 28.

[138] T.H. Osborne et al., ECA Vol. **29C** (2005) P4.012 (European Physical Society).

[139] J.A. Boedo, et al., ECA Vol. **29C** (2005) P5-047 (European Physical Society).

4. Publications with contributions from this research

[1] Wong CPC. Whyte DG. Bastasz R. Wampler W. Brooks JN. Evans TE. West WP. Whaley J. Doerner R. Watkins J. Allain JP. Hassanein A. Rudakov D., "DiMES contributions to PMI understanding," 20th IEEE/NPSS Symposium on Fusion Engineering (IEEE Cat. No.03CH37469C). IEEE. 2003, pp.236-41.

[2] Whyte DG. Evans TE. Wong CPC. West WP. Bastasz R. Allain JP. Brooks JN., "Experimental observations of lithium as a plasma-facing surface in the DIII-D tokamak divertor." Fusion Engineering & Design, vol.72, no.1-3, Nov. 2004, pp.133-47.

[3] Hollmann EM. and Pigarov AY., "Multi-fluid code simulation of DIII-D filterscope data including reflection of light from plasma-facing surfaces." Contributions to Plasma Physics, vol.44, no.1-3, 2004, pp.301-6.

[4] Buzhinskij OI. Barsuk VA. Otroshchenko VG. West WP. Whyte DG. "Effect of cyclic extremely high loads on behaviour of the ATJ graphite sample exposed to DIII-D divertor plasma." Fusion Engineering & Design, vol.65, no.4, July 2003, pp.537-43.

[5] Allain JP. Whyte DG. Brooks JN. Lithium erosion experiments and modelling under quiescent plasma conditions in DIII-D. Nuclear Fusion, vol.44, no.5, May 2004, pp.655-64.

[6] Humphreys DA. Ferron JR. Garofalo AM. Hyatt AW. Jernigan TC. Johnson RD. La Haye RJ. Leuer JA. Okabayashi M. Penaflor BG. Scoville JT. Strait EJ. Walker ML. Whyte DG. "Advanced tokamak operation using the DIII-D plasma control system." Fusion Engineering & Design, vol.66-68, Sept. 2003, pp.663-7.

[7] Evans TE. Moyer RA. Thomas PR. Watkins JG. Osborne TH. Boedo JA. Doyle EJ. Fenstermacher ME. Finken KH. Groebner RJ. Groth M. Harris JH. La Haye RJ. Lasnier CJ. Masuzaki S. Ohyabu N. Pretty DG. Rhodes TL. Reimerdes H. Rudakov DL. Schaffer MJ. Wang G. Zeng L. "Suppression of large edge-localized modes in high-confinement DIII-D plasmas with a stochastic magnetic boundary." Physical Review Letters, vol.92, no.23, 11 June 2004, pp.235003/1-4.

[8] McKee GR. Fonck RJ. Jakubowski M. Burrell KH. Hallatschek K. Moyer RA. Nevins W. Rudakov DL. Xu X., "Observation and characterization of radially sheared zonal flows in DIII-D." Plasma Physics & Controlled Fusion, vol.45, no.12A, Dec. 2003, pp.A477-85.

[9] Becoulet M. Huysmans G. Sarazin Y. Garbet X. Ghendrih P. Rimini F. Joffrin E. Litaudon X. Monier-Garbet P. Ane J-M. Thomas P. Grosman A. Parail V. Wilson H. Lomas P. de Vries P. Zastrow K-D. Matthews GF. Lonnroth J. Gerasimov S. Sharapov S. Gryaznevich M. Counsell G. Kirk A. Valovic M. Buttery R. Loarte A. Saibene G. Sartori R. Leonard A. Snyder P. Lao LL. Gohil P. Evans TE. Moyer RA. Kamada Y. Chankin A. Oyama N. Hatae T. Asakura N. Tudisco O. Giovannozzi E. Crisanti F. Perez CP. Koslowski HR. Eich T. Sips A. Horton L. Hermann A. Lang P. Stober J. Suttrop W. Beyer P. Saarelma S., "Edge localized mode physics and operational aspects in tokamaks," Plasma Physics & Controlled Fusion, vol.45, no.12A, Dec. 2003, pp.A93-113.

[10] Gray DS. Luckhardt SC. Chousal L. Gunner G. Kellman AG. Whyte DG. "Time resolved radiated power during tokamak disruptions and spectral averaging of AXUV photodiode response in DIII-D." Review of Scientific Instruments, vol.75, no.2, Feb. 2004, pp.376-81.

[11] Fenstermacher ME. Leonard AW. Snyder PB. Boedo JA. Brooks NH. Colchin RJ. Gray DS. Groebner RJ. Groth M. Hollmann EM. Lasnier CJ. Osborne TH. Petrie TW. Rudakov DL. Takahashi H. Watkins JG. Zeng L., "ELM particle and energy transport in the SOL and divertor of DIII-D." Plasma Physics & Controlled Fusion, vol.45, no.9, Sept. 2003, pp.1597-626.

[12] Van Oost G. Adamek J. Antoni V. Balan P. Boedo JA. Devynck P. Duran I. Eliseev L. Gunn JP. Hron M. Ionita C. Jachmich S. Kirnev GS. Martines E. Melnikov A. Schrittwieser R. Silva C. Stockel J. Tendler M. Varandas C. Van Schoor M. Vershkov V. Weynants RR. "Turbulent transport reduction by E * B velocity shear during edge plasma biasing: recent experimental results." Plasma Physics & Controlled Fusion, vol.45, no.5, April 2003, pp.621-43.

[13] Gohil P. Baylor LR. Burrell KH. Casper TA. Doyle EJ. Greenfield CM. Jernigan TC. Kinsey JE. Lasnier CJ. Moyer RA. Murakami M. Rhodes TL. Rudakov DL. Staebler GM. Wang G. Watkins JG. West WP. Zeng L., "Recent experimental studies of edge and internal transport barriers in the DIII-D tokamak." Plasma Physics & Controlled Fusion, vol.45, no.5, April 2003, pp.601-20.

[14] Hollmann EM. Gray DS. Whyte DG. Pigarov AYu. Krasheninnikov SI. Boedo JA. Humphreys DA. "Radiated power measurement during the thermal quench phase of a density limit disruption." Physics of Plasmas, vol.10, no.7, July 2003, pp.2863-70.

[15] Evans TE. Moyer RA. "Modeling of coupled edge stochastic and core resonant magnetic field effects in diverted tokamaks." Journal of Nuclear Materials, vol.313-316, March 2003, pp.1282-6.

[16] Whyte DG. Jernigan TC. Humphreys DA. Hyatt AW. Lasnier CJ. Parks PB. Evans TE. Taylor PL. Kellman AG. Gray DS. Hollmann EM. "Disruption mitigation with high-pressure noble gas injection." Journal of Nuclear Materials, vol.313-316, March 2003, pp.1239-46.

[17] West WP. Lasnier CJ. Whyte DG. Isler RC. Evans TE. Jackson GL. Rudakov D. Wade MR. Strachan J. "Methane penetration in DIII-D ELMing H-mode plasmas." Journal of Nuclear Materials, vol.313-316, March 2003, pp.1211-15.

[18] Pigarov AYu. Krasheninnikov SI. West WP. Rognlien TD. Boedo JA. Whyte DG. Lasnier CJ. Petrie TW. Schaffer MJ. Watkins JG., "DIII-D edge plasma simulations with UEDGE code including non-diffusive anomalous cross-field transport." Journal of Nuclear Materials, vol.313-316, March 2003, pp.1076-80.

[19] Groth M. Fenstermacher ME. Boedo JA. Brooks NH. Gray DS. Lasnier CJ. Leonard AW. Porter GD. Watkins JG., "High time-resolved, 2D imaging of type-I ELMs in DIII-D using a image-intensified CID camera."Journal of Nuclear Materials, vol.313-316, March 2003, pp.1071-5..

[20] Lasnier CJ. Burrell KH. deGrassie JS. Leonard AW. Moyer RA. Porter GD. Watkins JG. "Scrape-off layer features of the QH-mode." Journal of Nuclear Materials, vol.313-316, March 2003, pp.904-8.

[21] Stangeby PC. Elder JD. Boedo JA. Bray B. Brooks NH. Fenstermacher ME. Groth M. Isler RC. Lao LL. Lisgo S. Porter GD. Reiter D. Rudakov DL. Watkins JG. West WP. Whyte DG. "Interpretive modeling of simple-as-possible-plasma discharges on DIII-D using the OEDGE code."Journal of Nuclear Materials, vol.313-316, March 2003, pp.883-7.

[22] Jackson GL. Boedo JA. Lasnier CJ. Leonard AW. McKee GR. Murakami M. Wade MR. Watkins JG. West WP. Whyte DG. "Edge plasma effects in DIII-D impurity seeded discharges." Journal of Nuclear Materials, vol.313-316, March 2003, pp.878-82.

[23] Isler RC. Colchin RJ. Brooks NH. Evans TE. West WP. Whyte DG. "Carbon sources in the DIII-D tokamak." Journal of Nuclear Materials, vol.313-316, March 2003, pp.873-7.

[24] Boedo JA. Rudakov DL. Colchin RJ. Moyer RA. Krasheninnikov S. Whyte DG. McKee GR. Porter G. Schaffer MJ. Stangeby PC. West WP. Allen SL. Leonard AW. "Intermittent convection in the boundary of DIII-D." Journal of Nuclear Materials, vol.313-316, March 2003, pp.813-19.

[25] Leonard AW. Boedo JA. Fenstermacher ME. Groebner RJ. Goth M. Lasnier CJ. Mahdavi MA. Osborne TH. Rudakov DL. Petrie TW. Watkins JG. "Transport of ELM energy and particles into the SOL and divertor of DIII-D." Journal of Nuclear Materials, vol.313-316, March 2003, pp.768-76.

[26] Brooks JN. Kirschner A. Whyte DG. Ruzic DN. Alman DA. "Advances in the modeling of chemical erosion/redeposition of carbon divertors and application to the JET tritium codeposition problem." Journal of Nuclear Materials, vol.313-316, March 2003, pp.424-8.

[27] Wampler WR. Whyte DG. Wong CPC. West WP. "Erosion in the DIII-D divertor by neon-detached plasmas." Journal of Nuclear Materials, vol.313-316, March 2003, pp.333-6.

[28] Buzhinskij OI. Otroshchenko VG. Whyte DG. Baldwin M. Conn RW. Doerner RP. Seraydarian R. Luckhardt S. Kugel H. West WP. "Plasma deposition of boron films with high growth rate and efficiency using carborane." Journal of Nuclear Materials, vol.313-316, March 2003, pp.214-18.

[29] McKee GR. Fonck RJ. Jakubowski M. Burrell KH. Hallatschek K. Moyer RA. Rudakov DL. Nevins W. Porter GD. Schoch P. Xu X. "Experimental characterization of coherent, radially-sheared zonal flows in the DIII-D tokamak." Physics of Plasmas, vol.10, no.5, May 2003, pp.1712-19.

[30] Boedo JA. Rudakov DL. Moyer RA. McKee GR. Colchin RJ. Schaffer MJ. Stangeby PG. West WP. Allen SL. Evans TE. Fonck RJ. Hollmann EM. Krasheninnikov S. Leonard AW. Nevins W. Mahdavi MA. Porter GD. Tynan GR. Whyte DG. Xu X. "Transport by intermittency in the boundary of the DIII-D tokamak." Physics of Plasmas, vol.10, no.5, May 2003, pp.1670-7.

[31] Watkins JG. Lasnier CJ. Whyte DG. Stangeby PC. Ulrickson MA. "Calorimeter probe for the DIII-D divertor." Review of Scientific Instruments, vol.74, no.3, March 2003, pp.1574-7.

[32] Mossessian DA. Groebner RJ. Moyer RA. Osborne TH. Hughes JW. Greenwald M. Hubbard A. Rhodes TL. "Edge dimensionless identity experiment on DIII-D and Alcator C-Mod." Physics of Plasmas, vol.10, no.3, March 2003, pp.689-98.

[33] Buzhinskij OI. Barsuk VA. Otroshchenko VG. Markin AV. West WP. Whyte DG. "The investigation of structure, chemical composition, hydrogen isotope trapping and release processes in deposition layers on graphite sample surfaces exposed to DIII-D divertor plasma in extreme conditions." Fusion Engineering & Design, vol.61-62, Nov. 2002, pp.191-5.

[34] Evans TE. Moyer RA. Monat P. "Modeling of stochastic magnetic flux loss from the edge of a poloidally diverted tokamak." Physics of Plasmas, vol.9, no.12, Dec. 2002, pp.4957-67.

[35] Colchin RJ. Carreras BA. Maingi R. Baylor LR. Jernigan TC. Schaffer MJ. Carlstrom TN. Brooks NH. Greenfield CM. Gohil P. McKee GR. Rudakov DL. Rhodes TL. Doyle EJ. Austin ME. Watkins JG. "Physics of slow L-H transitions in the DIII-D tokamak." Nuclear Fusion, vol.42, no.9, Sept. 2002, pp.1134-43.

[36] Whyte DG. Jernigan TC. Humphreys DA. Hyatt AW. Lasnier CJ. Parks PB. Evans TE. Rosenbluth MN. Taylor PL. Kellman AG. Gray DS. Hollmann EM. Combs SK. "Mitigation of tokamak disruptions using high-pressure gas injection." Physical Review Letters, vol.89, no.5, 29 July 2002, pp.055001/1-4.

[37] Colchin RJ. Schaffer MJ. Carreras BA. McKee GR. Maingi R. Carlstrom TN. Rudakov DL. Greenfield CM. Rhodes TL. Doyle EJ. Brooks NH. Austin ME. "Slow L-H transitions in DIII-D plasmas." Physical Review Letters, vol.88, no.25, pt.1, 24 June 2002, pp.255002/1-4.

[38] Rudakov DL. Boedo JA. Moyer RA. Krasheninnikov S. Leonard AW. Mahdavi MA. McKee GR. Porter GD. Stangeby PC. Watkins JG. West WP. Whyte DG. Antar G. "Fluctuation-driven transport in the DIII-D boundary." Plasma Physics & Controlled Fusion, vol.44, no.6, June 2002, pp.717-31.

[39] Holland C. Tynan GR. Diamond PH. Moyer RA. Burin MJ. "Evidence for Reynolds-stress driven shear flows using bispectral analysis: theory and experiment." Plasma Physics & Controlled Fusion, vol.44, suppl.5A, May 2002, pp.A453-7.

[40] Carlstrom TN. Groebner RJ. Fenzi C. McKee GR. Moyer RA. Rhodes TL. "Evidence for the role of velocity shear on the L-H transition in DIII-D. Plasma Physics & Controlled Fusion, vol.44, suppl.5A, May 2002, pp.A333-9.

[41] Burrell KH. Austin ME. Brennan DP. DeBoo JC. Doyle EJ. Gohil P. Greenfield CM. Groebner RJ. Lao LL. Luce TC. Makowski MA. McKee GR. Moyer RA. Osborne TH. Porkolab M. Rhodes TL. Rost JC. Schaffer MJ. Stallard BW. Strait EJ. Wade MR. Wang G. Watkins JG. West WP. Zeng L. "Quiescent H-mode plasmas in the DIII-D tokamak." Plasma Physics & Controlled Fusion, vol.44, suppl.5A, May 2002, pp.A253-63.

[42] Greenfield CM. Burrell KH. Doyle EJ. Groebner RJ. West WP. Casper TA. DeBoo JC. Fenzi C. Gohill P. Kinsey JE. Lao LL. Leboeuf JN. Makowski MA. McKee GR. Moyer RA. Murakami M. Pinsker RI. Porter GD. Rettig CL. Rhodes TL. Staebler GM. Stallard BW. Synakowski EJ. Zeng L. DIII-D Team. "The quiescent double barrier regime in DIII-D." Plasma Physics & Controlled Fusion, vol.44, suppl.5A, May 2002, pp.A123-35.

[43] Boedo JA. Gray DS. Terry PW. Jachmich S. Tynan GR. Conn RW. "Scaling of plasma turbulence suppression with velocity shear." Nuclear Fusion, vol.42, no.2, Feb. 2002, pp.117-21.

[44] Mahdavi MA. Osborne TH. Leonard AW. Chu MS. Doyle EJ. Fenstermacher ME. McKee GR. Staebler GM. Petrie TW. Wade MR. Allen SL. Boedo JA. Brooks NH. Colchin RJ. Evans TE. Greenfield CM. Porter GD. Isler RC. La Haye RJ. Lasnier CJ. Maingi R. Moyer RA. Schaffer MJ. Stangeby PG. Watkins JG. West WP. Whyte DG. Wolf NS. "High performance H mode plasmas at densities above the Greenwald limit." Nuclear Fusion, vol.42, no.1, Jan. 2002, pp.52-8.

[45] Jackson GL. Murakami M. McKee GR. Baker DR. Boedo JA. La Haye RJ. Lasnier CJ. Leonard AW. Messiaen AM. Ongena J. Staebler GM. Unterberg B. Wade MR. Watkins JG. West WP. "Effects of impurity seeding in DIII-D radiating mantle discharges." Nuclear Fusion, vol.42, no.1, Jan. 2002, pp.28-41.

[46] Xu XQ. Cohen RH. Nevins WM. Porter GD. Rensink ME. Rognlien TD. Myra JR. D'Ippolito DA. Moyer RA. Snyder PB. Carlstrom TN. "Turbulence simulations of X point physics in the L-H transition." Nuclear Fusion, vol.42, no.1, Jan. 2002, pp.21-7.

[47] Federici G. Skinner CH. Brooks JN. Coad JP. Grisolia C. Haasz AA. Hassanein A. Philipps V. Pitcher CS. Roth J. Wampler WR. Whyte DG. "Plasma-material interactions in current tokamaks and their implications for next step fusion reactors." Nuclear Fusion, vol.41, spec. issue., Dec. 2001, pp.1967-2137.

[48] Groebner RJ. Baker DR. Burrell KH. Carlstrom TN. Ferron JR. Gohil P. Lao LL. Osborne TH. Thomas DM. West WP. Boedo JA. Moyer RA. McKee GR. Deranian RD. Doyle EJ. Rettig CL. Rhodes TL. Rost JC. "Progress in quantifying the edge physics of the H mode regime in DIII-D." Nuclear Fusion, vol.41, no.12, Dec. 2001, pp.1789-800.

[49] Doyle EJ. Baylor LR. Burrell KH. Casper TA. DeBoo JC. Ernst DR. Garofalo AM. Gohil P. Greenfield CM. Groebner RJ. Hyatt AW. Jackson GL. Jernigan TC. Kinsey JE. Lao LL. Lasnier CJ. Leboeuf J-N. Makowski M. McKee GR. Moyer RA. Murakami M. Osborne TH. Peebles WA. Porkolab M. Porter GD. Rhodes TL. Rost JC. Rudakov D. Staebler GM. Stallard BW. Strait EJ. Sydora RD. Synakowski EJ. Wade MR. Wang G. Watkins JG. West MP. Zeng L. "The quiescent double barrier regime in the DIII-D tokamak." Plasma Physics & Controlled Fusion, vol.43, no.12A, Dec. 2001, pp.A95-A112.

[50] Antar GY. Krasheninnikov SI. Devynck P. Doerner RP. Hollmann EM. Boedo JA. Luckhardt SC. Conn RW. "Experimental evidence of intermittent convection in the edge of magnetic confinement devices." Physical Review Letters, vol.87, no.6, 6 Aug. 2001, pp.065001/1-4.

[51] Allen SL. Anderson PM. Austin ME. Baggest DS. Baity W. Baker DR. Baldwin DE. Barber G. Bastasz R. Baxi CB. Baylor L. Bernabei S. Bialek J. Boedo JA. Bogatu IN. Bondeson A. Bozek AS. Bravenec R. Bray BD. Brennan D. Broesch JD. Brooks NH. Burrell KH. Burrus J. Callen J. Callis RW. Candy J. Carlstrom TN. Carolipio E. Carreras B. Cary WP. Casper TA. Chan VS. Chance M. Chen I. Chin E. Chiu HK. Chin SC. Chu M. Colchin RJ. Combs S. Comer K. Davis W. DeBoo JC. deGrassie JS. Delaware S. Dernian R. Doane JL. Doyle EJ. Edgell D. Ellis R. Ellis III R. Ernst D. Evans TE. Feder R. Ferstermacher ME. Fenzi C. Ferron JR. Finkenthal D. Fonck R. Fredrickson E. Freeman J. Friend M. Fuchs C. Galkin S. Garofalo A. Garstka G. Giruzzi G. Gohil G. Gootgeld AA. Gorelov I. Grantham N. Gray D. Gryazevich M. Greene JM. Grenne KL. Greenfield CM. Greenough N. Groebner RJ. Guenter S. Hahm TS. Hansink MJ. Harris TE. Harvey ! RW. Hatae T. Hegna C. Heidbrink WW. Hinton FL. Hogan J. Hollman E. Holtrop KL. Hong R-M. Hosea J. Houlberg W. Hsieh CL. Humphreys DA. Hyatt AW.

Ikezi H. Isayama A. Isler RC. Jackson GL. Jaluka N. Jayakumar J. Jensen TH. Jerigan T. Johnson L. Johsno RD. Kaplan DH. Keith KM. Kellman AG. Kellman DH. Khayrutdinov R. Kim JS. Kinsey JE. La Haye RJ. Labik G. Lao LL. Lasnier CJ. Latchem J. Lazarus EA. Lee RL. Legg RA. Leonard AW. Leuer JA. Lin-Liu YR. Lodestro L. Lohr JM. Luce TC. Luckhardt S. Lukash V. Luxon JL. Mahdavi MA. Maingi R. Makariou CC. Makowski MA. Mandrekas J. Manickam J. McHarg BB. McKee GE. Messiaen AM. Meyer WH. Middaugh KR. Miller RL. Mioduszewski PK. Moller J. Moyer RA. Murakami M. Nagy A. Navratil GA. Nerem A. Nevins W. Nikolski Y. Nilson DE. Okabayashi M. Omelchenko Y. O'Neill RC. Ongena J. Osborne TH. Owens L. Parks PB. Peebles AW. Penaflor BG. Perkins FW. Petersen PI. Petrie TW. ! Petty CC. Phillips JC. Piglowski DA. Pinsker RI. Politzer ! PA. Pon ce D. Porkolab M. Porter GD. Prater R. Pronko SG. Punjabi A. Raftopooulos S. Ramsey A. Reis Jr EE. Remsen DE. Rensink ME. Rettig CL. Rhodes TH. Rice BW. Robinson JI. Rolens G. Rosenbluth M. Ross D. Rost C. Rudakov D. Sauthoff N. Savercool RI. Schachter JM. Schaffer MJ. Schissel DP. Schmidt G. Scoville JT. Simone TC. Skinner SM. Snider RT. Snyder PB. St John HE. Stacey W. Staebler GM. Stellard BW. Stambaugh RD. Stangeby PG. Strait EJ. Synakowski E. Takahasi H. Takenaga H. Taylor PL. Taylor TS. Terpstra T. Thomas DM. Turgarinov S. Turnbull AD. Uterberg B. Vernon R. VonGoeler S. Wade MR. Waellbrock F. Walker ML. Waltz RE. Wampler WR. Watkins JG. Watson G. Wesley JC. West WP. Whaley Jr J. Whyte DG. Wilson H. Wolf N. Wong CPC. Wong K. Wong SK. Yin F. Zaniol B. Zeng L. Zerbini M. Zhang C. "Overview of recent experimental results from the DIII-D advanced tokamak programme." Nuclear Fusion, vol.41, no.10, Oct. 2001, pp.1341-53.

[52] Boedo JA. Rudakov D. Moyer R. Krasheninnikov S. Whyte D. McKee G. Tynan G. Schaffer M. Stangeby P. West P. Allen S. Evans T. Fonck R. Hollmann E. Leonard A. Mahdavi A. Porter G. Tillack M. Antar G. "Transport by intermittent convection in the boundary of the DIII-D tokamak." Physics of Plasmas, vol.8, no.11, Nov. 2001, pp.4826-33.

[53] Isler RC. Colchin RJ. Brooks NH. Evans TE. West WP. Whyte DG. "Spectroscopic determinations of carbon fluxes, sources, and shielding in the DIII-D divertors." Physics of Plasmas, vol.8, no.10, Oct. 2001, pp.4470-82.

[54] Moyer RA. Tynan GR. Holland C. Burin MJ. "Increased nonlinear coupling between turbulence and low-frequency fluctuations at the L-H transition." Physical Review Letters, vol.87, no.13, 24 Sept. 2001, pp.135001/1-4.

[55] Whyte DG. West WP. Wong CPC. Bastasz R. Brooks JN. Wampler WR. Brooks NH. Davis JW. Doerner RP. Haasz AA. Isler RC. Jackson GL. Macaulay-Newcombe RG. Wade MR. "The effect of detachment on carbon divertor erosion/redeposition in the DIII-D tokamak." Nuclear Fusion, vol.41, no.9, Sept. 2001, pp.1243-52.:

[56] McKee GR. Petty CC. Waltz RE. Fenzi C. Fonck RJ. Kinsey JE. Luce TC. Burrell KH. Baker DR. Doyle EJ. Garbet X. Moyer RA. Rettig CL. Rhodes TL. Ross DW. Staebler GM. Sydora R. Wade MR. "Nondimensional scaling of turbulence characteristics and turbulent diffusivity." Nuclear Fusion, vol.41, no.9, Sept. 2001, pp.1235-42.

[57] Greenfield CM. Burrell KH. DeBoo JC. Doyle EJ. Stallard BW. Synakowski EJ. Fenzi C. Gohil P. Groebner RJ. Lao LL. Makowski MA. McKee GR. Moyer RA. Rettig CL. Rhodes TL. Pinsker RI. Staebler GM. West WP. "Quiescent double barrier regime in the DIII-D tokamak." Physical Review Letters, vol.86, no.20, 14 May 2001, pp.4544-83.

[58] Tynan GR. Moyer RA. Burin MJ. Holland C. "On the nonlinear turbulent dynamics of shear-flow decorrelation and zonal flow generation." Physics of Plasmas, vol.8, no.6, June 2001, pp.2691-9.

[59] Rettig CL. Rhodes TL. Leboeuf JN. Peebles WA. Doyle EJ. Staebler GM. Burrell KH. Moyer RA. "Search for the ion temperature gradient mode in a tokamak plasma and comparison with theoretical predictions." Physics of Plasmas, vol.8, no.5, May 2001, pp.2232-7.

[60] Whyte DG. West WP. Doerner R. Brooks NH. Isler RC. Jackson GL. Porter G. Wade MR. Wong CPC. "Reduction of divertor carbon sources in DIII-D.".Journal of Nuclear Materials, vol.290-293, March 2001, pp.356-61.

[61] Wampler WR. Whyte DG. Wong CPC. West WP. "Suppression of net erosion in the DIII-D divertor with detached plasmas." Journal of Nuclear Materials, vol.290-293, March 2001, pp.346-51.

[62] Allen SL. Boedo JA. Bozek AS. Brooks NH. Carlstrom TN. Casper TA. Colchin RJ. Evans TE. Fenstermacher ME. Friend ME. Isler RC. Jayakumar R. Lasnier CJ. Leonard AW. Mahdavi MA. Maingi R. McKee GR. Moyer RA. Murakami M. Osborne TH. O'Neill RC. Petrie TW. Porter GD. Ramsey AT. Schaffer MJ. Stangeby PC. Stambaugh RD. Wade MR. Watking JG. West WP. Whyte DG. Wolf NS. "Experiments and computational modeling focused on divertor and SOL optimization for advanced tokamak operation on DIII-D. Journal of Nuclear Materials, vol.290-293, March 2001, pp.995-1001.

[63] Pitts RA. Duval BP. Loarte A. Moret J-M. Boedo JA. Coster D. Furno I. Horacek J. Kukushkin AS. Reiter D. Rommers J. "Divertor geometry effects on detachment in TCV.".Journal of Nuclear Materials, vol.290-293, March 2001, pp.940-6.

[64] Mahdavi MA. Wade MR. Watkins JG. Lasnier CJ. Luce T. Allen SL. Hyatt AW. Baxi C. Boedo JA. Bozek AS. Brooks NH. Colchin RJ. Evans TE. Fenstermacher ME. Friend ME. O'Neill RC. Isler RC. Kellman AG. Leonard AW. Maingi R. Moyer RA. Petrie TW. Porter GD. Schaffer MJ. Skinner S. Stambaugh RD. Stangeby PC. West WP. Whyte DG. Wolf NS. "Initial performance results of the DIII-D Divertor 2000." Journal of Nuclear Materials, vol.290-293, March 2001, pp.905-9.

[65] West WP. Porter GD. Evans TE. Stangeby P. Brooks NH. Fenstermacher ME. Isler RC. Rognlien TD. Wade MR. Whyte DG. Wolf NS. "Modeling of carbon transport in the divertor and SOL of DIII-D during high performance plasma operation." Journal of Nuclear Materials, vol.290-293, March 2001, pp.783-7.

[66] Watkins JG. Stangeby P. Boedo JA. Carlstrom TN. Lasnier CJ. Moyer RA. Rudakov DL. Whyte DG. "Comparison of Langmuir probe and Thomson scattering measurements in DIII-D." Journal of Nuclear Materials, vol.290-293, March 2001, pp.778-82.

[68] Stangeby PC. Watkins JG. Porter GD. Elder JD. Lisgo S. Reiter D. West WP. Whyte DG. "Onion-skin method (OSM) analysis of DIII-D edge measurements." Journal of Nuclear Materials, vol.290-293, March 2001, pp.733-7.

[68] Schaffer MJ. Boedo JA. Moyer RA. Carlstrom TN. Watkins JG. "Large E*B convection near the divertor X-point. Source Elsevier. Journal of Nuclear Materials, vol.290-293, March 2001, pp.530-6.

[69] Counsell GF. Coad P. Federici G. Krieger K. Philipps V. Skinner CH. Whyte DG. "Towards an improved understanding of the relationship between plasma edge and materials issues in a next-step fusion device." Journal of Nuclear Materials, vol.290-293, March 2001, pp.255-9.

[70] Burrell KH. Austin ME. Brennan DP. DeBoo JC. Doyle EJ. Fenzi C. Fuchs C. Gohil P. Greenfield CM. Groebner RJ. Lao LL. Luce TC. Makowski MA. McKee GR. Moyer RA. Petty CC. Porkolab M. Rettig CL. Rhodes TL. Rost JC. Stallard BW. Strait EJ. Synakowski EJ. Wade MR. Watkins JG. West WP. "Quiescent double barrier high-confinement mode plasmas in the DIII-D tokamak." Physics of Plasmas, vol.8, no.5, May 2001, pp.2153-62.

[71] Schaffer MJ. Bray BD. Boedo JA. Carlstrom TN. Colchin RJ. Hsieh C-L. Moyer RA. Porter GD. Rognlien TD. Watkins JG. "E*B circulation at the tokamak divertor X point." Physics of Plasmas, vol.8, no.5, May 2001, pp.2118-24.

[72] Rudakov DL. Boedo JA. Moyer RA. Lehmer RD. Gunner G. Watkins JG. "Fast electron temperature diagnostic based on Langmuir probe current harmonic detection on DIII-D." Review of Scientific Instruments, vol.72, no.1, pt.1-2, Jan. 2001, pp.453-6.

[73] Murakami M. McKee GR. Jackson GL. Staebler GM. Alexander DA. Baker DR. Bateman G. Baylor LR. Boedo JA. Brooks NH. Burrell KH. Cary JR. Cohen RH. Colchin RJ. DeBoo JC. Doyle EJ. Ernst DR. Evans TE. Fenzi C. Greenfield CM. Greewood DE. Groebner RJ. Hogan JT. Houlberg WA. Hyatt AM. Jayakumar R. Jernigan TC. Jong RA. Kinsey JE. Kritz AH. La Haye RJ. Lao LL. Lasnier CJ. Makowski MA. Mandrekas J. Messiaen AM. Moyer RA. Ongena J. Pankin A. Petrie TW. Petty CC. Rettig CL. Rhodes TL. Rice BW. Ross DW. Rost JC. Shasharina SG. St John HE. Stacey WM. Strand PI. Sydora RD. Taylor TS. Thomas DM. Wade MR. Waltz RE. West WP. Wong KL. Zeng L. "Physics of confinement improvement of plasmas with impurity injection in DIII-D." Nuclear Fusion, vol.41, no.3, March 2001, pp.317-23.

[74] Boedo J. Gunner G. Gray D. Conn R. "Robust Langmuir probe circuitry for fusion research." Review of Scientific Instruments, vol.72, no.2, Feb. 2001, pp.1379-82.

[75] Whyte DG. Tynan GR. Doerner RP. Brooks JN. "Investigation of carbon chemical erosion with increasing plasma flux and density."Nuclear Fusion, vol.41, no.1, Jan. 2001, pp.47-62.

[76] Harvey RW. Chan VS. Chiu SC. Evans TE. Rosenbluth MN. Whyte DG. "Runaway electron production in DIII-D killer pellet experiments, calculated with the CQL3D/KPRAD model." Physics of Plasmas, vol.7, no.11, Nov. 2000, pp.4590-9.

[77] Humphreys DA. Whyte DG. "Classical resistivity in a post-thermal quench disrupting plasma." Physics of Plasmas, vol.7, no.10, Oct. 2000, pp.4057-61.

[78] Whyte DG. Humphreys DA. Taylor PL. "Measurement of plasma electron temperature and effective charge during tokamak disruptions." Physics of Plasmas, vol.7, no.10, Oct. 2000, pp.4052-6.

[79] Boedo JA. Terry PW. Gray D. Ivanov RS. Conn RW. Jachmich S. van Oost G. "Suppression of temperature fluctuations and energy barrier generation by velocity shear." Physical Review Letters, vol.84, no.12, 20 March 2000, pp.2630-3.

[80] Porter GD. Isler R. Boedo J. Rognlien TD. "Detailed comparison of simulated and measured plasma profiles in the scrape-off layer and edge plasma of DIII-D." Physics of Plasmas, vol.7, no.9, Sept. 2000, pp.3663-80.

[81] Boedo J. Gray D. Jachmich S. Conn R. Terry GP. Tynan G. Van Oost G. Weynants RR. "Enhanced particle confinement and turbulence reduction due to E*B shear in the TEXTOR tokamak." Nuclear Fusion, vol.40, no.7, July 2000, pp.1397-410.

[82] Xu XQ. Cohen RH. Porter GD. Rognlien TD. Ryutov DD. Myra JR. D'Ippolito DA. Moyer RA. Groebner RJ. "Turbulence studies in tokamak boundary plasmas with realistic divertor geometry." Nuclear Fusion, vol.40, spec. issue., 2000, pp.731-6.

[83] McKee GR. Murakami M. Boedo JA. Brooks NH. Burrell KH. Ernst DR. Fonck RJ. Jackson GL. Jakubowski M. La Haye RJ. Messiaen AM. Ongena J. Rettig CL. Rice BW. Rost C. Staebler GM. Sydora RD. Thomas DM. Unterberg B. Wade MR. West WP. "Impurity-induced turbulence suppression and reduced transport in the DIII-D tokamak." Physics of Plasmas, vol.7, no.5, May 2000, pp.1870-7.

[84] Boedo JA. Schaffer MJ. Maingi R. Lasnier CJ. "Electric field-induced plasma convection in tokamak divertors." Physics of Plasmas, vol.7, no.4, April 2000, pp.1075-8.

[85] Boedo JA. Ongena J. Sydora R. Gray DS. Jachmich S. Conn RW. Messiaen A. "Turbulent transport and turbulence in radiative I mode plasmas in TEXTOR-94.." Nuclear Fusion, vol.40, no.2, Feb. 2000, pp.209-21.

[86] Allen SL. Brooks NH. Bastasz R. Boedo J. Brooks JN. Cuthbertson JW. Evans TE. Fenstermacher ME. Hill DN. Hillis DL. Hogan J. Hyatt AW. Isler RC. Jackson GL. Jernigan T. Lasnier CJ. Lehmer R. Leonard AW. Mahdavi MA. Maingi R. Meyer WH. Mioduszewski PK. Moyer RA. Nilson DG. Owen LW. Petrie TW. Porter GD. Rensink ME. Schaffer MJ. Smith J. Staebler GM. Stambaugh RD. Thomas DM. Wade MR. Wampler WR. Watkins JG. West WP. Whyte DG. Wolf N. Wong CPC. Wood RD. "Radiative divertor and scrape-off layer experiments in open and baffled diverters on DIII-D."IAEA. Nuclear Fusion, vol.39, spec. issue., 1999, pp.2015-23.

[87] Whyte DG. Coad JP. Franzen P. Maier H. "Similarities in divertor erosion/redeposition and deuterium retention patterns between the tokamaks ASDEX Upgrade, DIII-D and JET." Nuclear Fusion, vol.39, no.8, Aug. 1999, pp.1025-9.

[88] Boedo JA. Gray D. Schaffer M. Conn RW. Luong P. Ivanov RS. Chernilevsky VA. van Oost G. "On the harmonic technique to measure electron temperature with high time resolution." Review of Scientific Instruments, vol.70, no.7, July 1999, pp.2997-3006.

[89] Gray DS. Baelmans M. Boedo JA. Reiter D. Conn RW. "Self-consistent plasma-neutral modeling in tokamak plasmas with a large-area toroidal belt limiter." Physics of Plasmas, vol.6, no.7, July 1999, pp.2816-25.

[90] Brooks JN. Whyte DG. "Modelling and analysis of DIII-D/DiMES sputtered impurity transport experiments." Nuclear Fusion, vol.39, no.4, April 1999, pp.525-38.

[91] Moyer RA. Lehmer R. Boedo JA. Watkins JG. Xu X. Myra JR. Cohen R. D'Ippolito DA. Petrie TW. Schaffer MJ. "Potentials, E*B drifts, and fluctuations in the DIII-D boundary." Journal of Nuclear Materials, vol.266-269, March 1999, pp.1145-50.

[92] Xu XQ. Cohen RH. Porter GD. Myra JR. D'Ippolito DA. Moyer R. "Turbulence in boundary plasmas." Journal of Nuclear Materials, vol.266-269, March 1999, pp.993-6.

[93] Watkins JG. Batishchev O. Boedo J. Hill DN. Lasnier CJ. Lehmer R. Leonard AW. Moyer RA. "An evaluation of kinetic effects in the DIII-D divertor." Journal of Nuclear Materials, vol.266-269, March 1999, pp.980-5.

[94] Buzhinskij OI. Opimach IV. Barsuk VA. Arkhipov II. West WP. Whyte D. Wong CPC. Wampler WR. "The investigation of structure, chemical composition, hydrogen isotope trapping and release processes in deposition layers on surfaces exposed to DIII-D divertor plasma." Journal of Nuclear Materials, vol.266-269, March 1999, pp.793-7.

[95] Boedo JA. Lehmer R. Moyer RA. Watkins JG. Porter GD. Evans TE. Leonard AW. Schaffer MJ. "Measurements of flows in the DIII-D divertor by Mach probes." Journal of Nuclear Materials, vol.266-269, March 1999, pp.783-7.

[96] West WP. Brooks NH. Fenstermacher ME. Isler RC. Jackson GL. Lasnier CJ. Ramsey A. Wade MR. Whyte DG. Wood RD. "Carbon influx in He and D plasmas in DIII-D." Journal of Nuclear Materials, vol.266-269, March 1999, pp.732-8.

[97] Petrie TW. Maingi R. Porter GD. Allen SL. Fenstermacher ME. Groebner RJ. Hill DN. Leonard AW. Lasnier CJ. Mahdavi MA. Moyer RA. Rensink ME. Thomas DM. West WP. "The role of neutrals in the H-L back transition of high density single-null and double-null gas-fueled discharges in DIII-D." Journal of Nuclear Materials, vol.266-269, March 1999, pp.642-7.

[98] Maingi R. Mahdavi MA. Petrie TW. Baylor LR. Jernigan TC. La Haye RJ. Hyatt AW. Wade MR. Watkins JG. Whyte DG. "Density limit studies on DIII-D." Journal of Nuclear Materials, vol.266-269, March 1999, pp.598-603.

[99] Jackson GL. Murakami M. Staebler GM. Wade MR. Messiaen AM. Ongena J. Unterberg B. Boedo JA. Evans TE. Hyatt AW. LaHaye RJ. Lasnier CJ. Leonard AW. McKee GW. Maingi R. Moyer RA. Petrie TW. West WP. "Enhanced confinement discharges in DIII-D with neon and argon induced radiation."Journal of Nuclear Materials, vol.266-269, March 1999, pp.380-5.

[100] Fenstermacher ME. Allen SL. Hill DN. Isler RC. Lasnier CJ. Leonard AW. Petrie TW. Porter GD. West WP. Whyte DG. Wood RD. "Evolution of 2D deuterium and impurity radiation profiles during transitions from attached to detached divertor operation in DIII-D." Journal of Nuclear Materials, vol.266-269, March 1999, pp.348-53.

[101] Schaffer MJ. Boedo JA. Brooks NH. Isler RC. Moyer RA. "Plasma pressure and flows during divertor detachment." Journal of Nuclear Materials, vol.266-269, March 1999, pp.264-71.

[102] Allen SL. Fenstermacher ME. Greenfield CM. Hyatt AW. Maingi R. Porter GD. Wade MR. Bozek AS. Ellis R. Hill DN. Hollerbach MA. Lasnier CJ. Leonard AW. Mahdavi MA. Nilson DG. Petrie TW. Schaffer MJ. Smith JP. Stambaugh RD. Thomas DM. Watkins JG. West WP. Whyte DG. Wood RD. "Studies of high- delta (baffled) low- delta (open) pumped divertor operation on DIII-D." Journal of Nuclear Materials, vol.266-269, March 1999, pp.168-74.

[103] Whyte DG. Bastasz R. Brooks JN. Wampler WR. West WP. Wong CPC. Buzhinskij OI. Opimach IV. "Divertor erosion in DIII-D." Journal of Nuclear Materials, vol.266-269, March 1999, pp.67-74.

[104] Brooks JN. Alman D. Federici G. Ruzic DN. Whyte DG. "Erosion/redeposition analysis: status of modeling and code validation for semi-detached tokamak edge plasmas." Journal of Nuclear Materials, vol.266-269, March 1999, pp.58-66.

[105] Wade MR. West WP. Wood RD. Allen SL. Boedo JA. Brooks NH. Fenstermacher ME. Hill DN. Hogan JT. Isler RC. Jackson GL. Lasnier CJ. Lehmer R. Leonard AW. Mahdavi MA. Maingi R. Moyer RA. Osborne TH. Petrie TW. Schaffer MJ. Stambaugh RD. Watkins JG. Whyte DG. "Impurity enrichment and radiative enhancement using induced SOL flow in DIII-D." Journal of Nuclear Materials, vol.266-269, March 1999, pp.44-50..

[106] Rhodes TL. Moyer RA. Groebner R. Doyle EJ. Lehmer R. Peebles WA. Rettig CL. "Experimental evidence for self-organized criticality in tokamak plasma turbulence." Physics Letters A, vol.253, no.3-4, 22 March 1999, pp.181-6.

[107] Taylor PL. Kellman AG. Evans TE. Gray DS. Humphreys DA. Hyatt AW. Jernigan TC. Lee RL. Leuer JA. Luckhardt SC. Parks PB. Schaffer MJ. Whyte DG. Zhang J. "Disruption mitigation studies in DIII-D." Physics of Plasmas, vol.6, no.5, May 1999, pp.1872-9.

[108] Ongena J. Messiaen AM. Unterberg B. Budny RV. Bush CE. Hill K. Hoang GT. Jackson G. Kallenbach A. Monier-Garbet P. Mueller D. Murakami M. Staebler G. Ryter F. Wade M. Bell M. Boedo J. Bonheure G. Dumortier P. Durodie F. Finken KH. Fuchs G. Giesen B. Hutteman P. Jaspers R. Koch R. Kramer-Flecken A. Mertens Ph. Moyer R. Pospieszczyk A. Ramsey A. Samm U. Sauer M. Schweer B. Uhlemann R. Vandenplas PE. Van Oost G. Vervier M. Van Wassenhove G. Waidmann G. Weynants RR. Wolf GH. "Overview of experiments with radiation cooling at high confinement and high density in limited and diverted discharges." Plasma Physics & Controlled Fusion, vol.41, suppl.3A, March 1999, pp.A379-99.

[109] Fenstermacher ME. Boedo J. Isler RC. Leonard AW. Porter GD. Whyte DG. Wood RD. Allen SL. Brooks NH. Colchin R. Evans TE. Hill DN. Lasnier CJ. Lehmer RD. Mahdavi MA. Maingi R. Moyer RA. Petrie TW. Rognlien TD. Schaffer MJ. Stambaugh RD. Wade MR. Watkins JG. West WP. Wolf N. "Physics of the detached radiative divertor regime in DIII-D."Plasma Physics & Controlled Fusion, vol.41, suppl.3A, March 1999, pp.A345-55.

[110] Boedo J. Gray D. Conn R. Jackmich S. van Oost G. Weynants RR. "Stabilization of turbulence and enhanced particle confinement by velocity shear." Acad. Sci. Czech. Republic, Inst. Phys. Czechoslovak Journal of Physics, vol.48, suppl., pt.S3, 1998, pp.99-119.

[111] Jachmich S. van Oost G. Weynants RR. Boedo J. "Induced radial electric fields and their influence on particle transport, confinement and exhaust in TEXTOR." Acad. Sci. Czech. Republic, Inst. Phys. Czechoslovak Journal of Physics, vol.48, suppl., pt.S3, 1998, pp.32-46.

[112] Moyer RA. Rhodes TL. Rettig CL. Doyle EJ. Burrell KH. Cuthbertson J. Groebner RJ. Kim KW. Leonard AW. Maingi R. Porter GD. Watkins JG. "Study of the phase transition dynamics of the L to H transition." Plasma Physics & Controlled Fusion, vol.41, no.2, Feb. 1999, pp.243-9.

[113] Staebler GM. Jackson GL. West WP. Allen SL. Groebner LRJ. Schaffer MJ. Whyte DG. "Improved high-confinement mode with neon injection in the DIII-D tokamak." Physical Review Letters, vol.82, no.8, 22 Feb. 1999, pp.1692-5.

[114] Wade MR. Hogan JT. Allen SL. Brooks NH. Hill DN. Maingi R. Schaffer MJ. Watkins JG. Whyte DG. Wood RD. West WP. "Impurity enrichment studies with induced scrape-off layer flow on DIII-D." Nuclear Fusion, vol.38, no.12, Dec. 1998, pp.1839-59.

[115] Bolt H. Scholz T. Boedo J. Finken KH. Hassanein A. "High heat flux erosion of carbon fibre composite materials in the TEXTOR tokamak." Journal of Nuclear Materials, vol.258-263, pt.A, Oct. 1998, pp.757-63.

[116] Wong CPC. Whyte DG. Bastasz RJ. Brooks J. West WP. Wampler WR. "Divertor materials evaluation system (DiMES)." Journal of Nuclear Materials, vol.258-263, pt.A, Oct. 1998, pp.433-9.

[117] Gray DS. Boedo JA. Baelmans M. Conn RW. Moyer RA. Dippel KH. Finken KH. Pospieszczyk A. Reiter D. Doerner RP. Hillis DL. Mank G. Wolf GH. Team T. "Plasma exhaust and density control in Tokamak fusion experiments with neutral beam or ICRF auxiliary heating." Nuclear Fusion, vol.38, no.11, Nov. 1998, pp.1585-606.

[118] Whyte DG. Evans TE. Hyatt AW. Jernigan TC. Lee RL. Kellman AG. Parks PB. Stockdale R. Taylor PL. "Rapid inward impurity transport during impurity pellet injection on the DIII-D tokamak." Physical Review Letters, vol.81, no.20, 16 Nov. 1998, pp.4392-5.

[119] Bolt H. Scholz T. Boedo J. Finken KH. Hassanein A. Linke J. "Response of plasma-facing materials to high transient heat loads in a tokamak." Fusion Engineering & Design, vol.39-40, Sept. 1998, pp.287-94.

[120] Boedo JA. Porter GD. Schaffer MJ. Lehmer R. Moyer RA. Watkins JG. Evans TE. Lasnier CJ. Leonard AW. Allen SL. "Flow reversal, convection, and modeling in the DIII-D divertor." Physics of Plasmas, vol.5, no.12, Dec. 1998, pp.4305-10.

[121] Ongena J. Boedo J. Bonheure G. Budny RV. Bush CE. Dumortier P. Evans T. Hill K. Hyatt A. Jackson G. Messiaen AM. Mueller D. Ramsey A. Staebler G. Unterberg B. Vandenplas PE. Wade M. van Wassenhove G. Weynants RR. "Overview of improved confinement in impurity seeded discharges in TEXTOR-94, DIII-D and TFTR." Fusion Theory. Proceedings of the Seventh European Fusion Theory, Conference. Forschungszetrum Julich GmbH. 1998, pp.91-4. Julich, Germany.

[122] Whyte DG. Isler RC. Wade MR. Schultz DR. Krstic PS. Hung CC. West WP. "Argon density measurements from charge-exchange spectroscopy." Physics of Plasmas, vol.5, no.10, Oct. 1998, pp.3694-9.

[123] Opimach IV. Buzhinskij OI. Arkhipov IN. West WP. Wampler W. Whyte D. "Hydrogen isotope retention in B/sub 4/C coating on RGT graphite under high heat fluxes of DIII-D divertor plasma." 17th IEEE/NPSS Symposium Fusion Engineering (Cat. No.97CH36131). IEEE. Part vol.2, 1998, pp.881-3 vol.2.

[124] Kugel HW. Boedo J. Chance M. Goldston R. Jardin S. Kesner J. Luckhardt S. Manickam J. McGuire AK. Okabayashi M. Schmidt J. Schmitz L. Zakharov L. "Feedback stabilization experiment for MHD control with edge current." 17th IEEE/NPSS Symposium Fusion Engineering (Cat. No.97CH36131). IEEE. Part vol.1, 1998, pp.517-22 vol.1. New York, NY, USA.

[125] Boedo J. Grey D. Chousal L. Conn R. Hiller B. Finken KH. "Fast scanning probe for tokamak plasmas." Review of Scientific Instruments, vol.69, no.7, July 1998, pp.2663-70.

[126] Jachmich.S. Van Oosts G. Weynants RR. Boedo JA. "Experimental investigations on the role of E*B flow shear in improved confinement." Plasma Physics & Controlled Fusion, vol.40, no.6, June 1998, pp.1105-13.

[127] Whyte DG. Wade MR. Finkenthal DF. Burrell KH. Monier-Garbet P. Rice BW. Schissel DP. West WP. Wood RD. "Measurement and verification of Z/subeff/ radial profiles using charge exchange recombination spectroscopy on DIII-D." Nuclear Fusion, vol.38, no.3, March 1998, pp.387-98.

[128] Rhodes TL. Peebles WA. Doyle EJ. Pribyl P. Gilmore M. Moyer RA. Lehmer RD. "Signal amplitude effects on reflectometer studies of density turbulence in tokamaks." Plasma Physics & Controlled Fusion, vol.40, no.4, April 1998, pp.493-510.

[129] Leonard AW. Porter GD. Wood RD. Allen SL. Boedo J. Brooks NH. Evans TE. Fenstermacher ME. Hill DN. Isler RC. Lasnier CJ. Lehmer RD. Mahdavi MA. Maingi R. Moyer RA. Petrie TW. Schaffer MJ. Wade MR. Watkins JG. West WP. Whyte DG. "Radiative divertor plasmas with convection in DIII-D." Physics of Plasmas, vol.5, no.5, May 1998, pp.1736-43.